Pontifícia Universidade Católica
do Rio de Janeiro

Clarice de Amorim

Pore-Scale Mechanisms of Oil Displacement by Emulsion Injection

Tese de Doutorado

Thesis presented to the Programa de Pós–graduação em Engenharia Mecânica, do Departamento de Engenharia Mecânica da PUC-Rio in partial fulfillment of the requirements for the degree of Doutor em Engenharia Mecânica.

Advisor : Prof. Marcio da Silveira Carvalho
Co-advisor: Dr. Ranena Verónica Ponce Flores

Rio de Janeiro
July 2024

Pontifícia Universidade Católica
do Rio de Janeiro

Clarice de Amorim

Pore-Scale Mechanisms of Oil Displacement by Emulsion Injection

Thesis presented to the Programa de Pós–graduação em Engenharia Mecânica da PUC-Rio in partial fulfillment of the requirements for the degree of Doutor em Engenharia Mecânica. Approved by the Examination Committee:

Prof. Marcio da Silveira Carvalho
Departamento de Engenharia Mecânica - PUC-Rio

Dr. Ranena Verónica Ponce Flores
Departamento de Engenharia Mecânica - PUC-Rio

Prof. Ian Gates
Department of Chemical and Petroleum Engineering - University of Calgary

Prof. Mônica Feijó Naccache
Departamento de Engenharia Mecânica - PUC-Rio

Prof. Paulo Roberto de Souza Mendes
Departamento de Engenharia Mecânica - PUC-Rio

Prof. Vladimir Alvarado Basante
Department of Energy and Petroleum Engineering - University of Wyoming

Prof. Yves Méheust
Géosciences Rennes - Université de Rennes 1

Rio de Janeiro, July the 29th, 2024

Clarice de Amorim

Majored in Petroleum Engineering, Clarice holds a Master's degree in Mechanical Engineering from Universidade Estadual de Campinas (UNICAMP). Currently, she is a PhD candidate in the Laboratory of Microhydrodynamics and Flow in Porous Media (LMMP) at Pontifícia Universidade Católica do Rio de Janeiro (PUC-Rio).

Bibliographic data

Amorim, Clarice de

Pore-Scale Mechanisms of Oil Displacement by Emulsion Injection / Clarice de Amorim; advisor: Marcio da Silveira Carvalho; co-advisor: Ranena Verónica Ponce Flores. – 2024.

118 f: il. color. ; 30 cm

Tese (doutorado) - Pontifícia Universidade Católica do Rio de Janeiro, Departamento de Engenharia Mecânica, 2024.

Inclui bibliografia

1. Engenharia Mecânica – Teses. 2. Microfluídica. 3. Escoamento em meios porosos. 4. Escoamento de emulsão. 5. EOR. 6. Emulsão óleo-em-água. I. Carvalho, Marcio da Silveira. II. Ponce Flores, Ranena Verónica. III. Pontifícia Universidade Católica do Rio de Janeiro. Departamento de Engenharia Mecânica. IV. Título.

CDD: 621

Dedicated to my parents, Paulo and Isabel, and my brother, Ricardo,
for their eternal love and support.

Acknowledgments

To God, for guiding me throughout the journey of life.

To my advisor, Professor Marcio Carvalho, thank you for your invaluable guidance, support, and trust throughout my academic journey. Your example and encouragement have profoundly inspired me to become not only a researcher but also a dedicated scientist.

To my co-advisor, Dr. Ranena Ponce, I am deeply grateful for your generous support, exceptional technical expertise, and indispensable suggestions.

To Dr. Amanda Pessoa and Jesús Daniel, thank you for your inspirational and insightful discussions, which have significantly contributed to this thesis. I also extend my sincere thanks to Leonardo Moreira for his generous assistance and invaluable support with the experiments throughout the years in the lab.

To my parents, Paulo and Isabel, and my brother Ricardo, I offer my deepest and most heartfelt gratitude for your endless love and selfless support. Your encouragement has been my guiding force through life, and your genuine belief in me has been my greatest strength.

To my dear Caio Mello, thank you for inspiring me to persevere and for being by my side through this often challenging journey. Your constant love and support have enriched my life in countless meaningful ways.

To Margarida Alves and Alice Casanova, thank you for embracing me into your lives with so much warmth and support.

To Vivian Mendes, whom I consider a sister, thank you for sharing countless moments and growing alongside me. Your presence has been a treasured and irreplaceable part of my life.

To my friends Andrea Mora and Jesús Daniel, whom I met at PUC-Rio and will cherish for life, thank you for your affection and for brightening my journey. Your friendship has been truly invaluable.

To my dear colleagues from the "gray room", I extend my sincere gratitude. Whether you are still here or have embarked on new paths, your support and inspiration have made my academic journey deeply fulfilling and exciting.

To my research group members, thank you for your valuable contributions and companionship in the lab. Your collaborative spirit has made this journey stimulating and rewarding.

To all the professors and staff at PUC-Rio, thank you for your exceptional lessons and dedicated service. Your contributions have been essential to my education and the successful completion of this significant milestone.

To PUC-Rio and Repsol-Sinopec Brasil, thank you for the funding that made this research possible.

This study was financed in part by the Coordenação de Aperfeiçoamento de Pessoal de Nível Superior - Brasil (CAPES) - Finance Code 001.

Abstract

Amorim, Clarice de; Carvalho, Marcio da Silveira (Advisor); Ponce Flores, Ranena Verónica (Co-Advisor). **Pore-Scale Mechanisms of Oil Displacement by Emulsion Injection**. Rio de Janeiro, 2024. 118p. Tese de Doutorado – Departamento de Engenharia Mecânica, Pontifícia Universidade Católica do Rio de Janeiro.

Water injection is the most commonly used method for extending the productive life of oil reservoirs; however, its efficiency is limited by an unfavorable mobility ratio between the injected aqueous phase and the displaced oil phase. Reservoir heterogeneity exacerbates this issue, driving water through preferential flow paths with lower capillary resistance, leaving trapped oil behind. Recent studies propose oil-in-water emulsions as a pore-blocking agent to reduce aqueous phase mobility, leading to a more uniform displacement front and enhancing oil recovery. Despite recent developments in emulsion injection for enhanced oil recovery (EOR), fundamental aspects of the pore-scale dynamics of oil-in-water emulsion flow and its correlation with observed macroscopic mobility reduction remain not completely understood. This study explores key factors influencing the design of an effective emulsion injection process, including emulsion drop size, pore throat distribution, and injection flow rate, and their impact on the mobility reduction of the aqueous phase. Two-dimensional porous media micromodels were employed to visualize drop dynamics, examining how pore-scale phenomena affect aqueous phase mobility reduction. Two distinct geometries were designed for this purpose. The linear micromodel ensures a constant pressure gradient and flow velocity along its length, while the radial configuration assesses emulsion flooding performance under varying capillary numbers. In the latter configuration, the flow area increases with the radius, reducing the flow velocity as the fluid moves away from the injection point. Results show that mobility reduction can be finely controlled by the capillary number and the drop size distribution. At sufficiently high capillary numbers, the pressure difference in most pores is strong enough to overcome the capillary pressure needed to push a drop through the constriction; the number of trapped drops is relatively small, and mobility reduction is weak. Conversely, at low capillary numbers, the number of trapped drops is large; the mobility reduction is strong and dependent on the drop size distribution. Additionally, in radial flow, stronger pore-blocking occurs below a critical capillary number, where capillary resistance surpasses viscous pressure. Flow visualization demonstrates that emulsion flooding improves pore-level displacement efficiency, reducing residual oil saturation. These findings offer valuable insights into tailoring oil-in-water emulsions for injection into

reservoirs with known pore throat distributions, aiming to achieve the necessary aqueous phase mobility reduction and consequently increase oil recovery factors.

Keywords

Microfluidics; Flow in porous media; Flow of emulsion; EOR; Oil-in-water emulsion.

Resumo

Amorim, Clarice de; Carvalho, Marcio da Silveira; Ponce Flores, Ranena Verónica. **Mecanismos em Escala de Poros de Deslocamento de Óleo por Injeção de Emulsão**. Rio de Janeiro, 2024. 118p. Tese de Doutorado – Departamento de Engenharia Mecânica, Pontifícia Universidade Católica do Rio de Janeiro.

A injeção de água é o método mais utilizado para estender a vida produtiva de reservatórios de petróleo. No entanto, sua eficiência é limitada pela relação de mobilidade desfavorável entre a fase aquosa injetada e a fase oleosa deslocada. A heterogeneidade das formações agrava essa questão, direcionando a água através de caminhos preferenciais, resultando na retenção de óleo residual. Estudos recentes propõem emulsões de óleo-em-água como agentes de bloqueio para reduzir a mobilidade da fase aquosa. A redução da mobilidade associada à captura de gotas da fase dispersa leva a uma frente de deslocamento mais uniforme, aumentando a recuperação de óleo. Apesar dos avanços recentes na injeção de emulsões como método de recuperação avançada de petróleo (EOR), aspectos fundamentais do escoamento de emulsões óleo-em-água a nível microscópico e sua relação com a redução macroscópica na mobilidade da fase aquosa ainda necessitam de maior compreensão. Este estudo explora fatores que influenciam a eficácia de um processo de injeção de emulsão, incluindo o tamanho das gotas, a distribuição das gargantas de poros e a vazão de injeção, que influenciam diretamente na redução da mobilidade. Micromodelos bidimensionais foram empregados para visualizar a dinâmica de retenção e liberação de gotas, relacionando fenômenos em escala de poros à mobilidade da fase aquosa. Duas geometrias foram projetadas para este propósito. O micromodelo linear assegura um gradiente de pressão e uma velocidade constante ao longo de seu comprimento, enquanto a configuração radial avalia o desempenho da injeção de emulsão sob diferentes números de capilaridade. Nesta última configuração, a área de fluxo aumenta com o raio, reduzindo a velocidade do escoamento à medida que o fluido se afasta do ponto de injeção. Os resultados mostram que a redução da mobilidade pode ser controlada pelo número de capilaridade e pela distribuição do tamanho de gotas. Em números de capilaridade suficientemente altos, a diferença de pressão na maioria das gargantas de poro supera a pressão capilar, empurrando as gotas através das constrições. Nestes casos, a retenção de gotas é baixa e a redução da mobilidade é fraca. Por outro lado, em números de capilaridade baixos, a retenção de gotas é alta, causando uma redução significativa na mobilidade da fase aquosa, que é fortemente dependente da distribuição do tamanho de gotas. Além disso, no fluxo radial, o bloqueio de poros ocorre

abaixo de um número de capilaridade crítico, onde a força capilar supera a pressão viscosa. O trabalho demonstra que a injeção de emulsão melhora a eficiência de deslocamento a nível microscópico, reduzindo a saturação residual de óleo. Os resultados podem orientar a seleção de características específicas de emulsões a serem injetadas em reservatórios com distribuições conhecidas de gargantas de poros, visando alcançar a necessária redução na mobilidade da fase aquosa e, consequentemente, incrementar a recuperação de óleo.

Palavras-chave

Microfluídica; Escoamento em meios porosos; Escoamento de emulsão; EOR; Emulsão óleo-em-água.

Table of contents

List of figures

List of tables

1
Introduction

1.1
Overview

Water flooding remains the prevailing method for extending the productive life of oil reservoirs. However, its effectiveness is often limited by the high mobility ratio between water and oil phases. This unfavorable mobility ratio causes water to flow preferentially through paths with lower capillary resistance, leaving significant amounts of oil trapped in pore throats where capillary forces are higher.

To overcome water flooding inefficiency, various enhanced oil recovery (EOR) methods have been studied to mobilize trapped oil and guide it toward production wells, thereby improving oil recovery. These methods often involve the use of pore-blocking agents designed to reduce water mobility in high-permeability areas. By blocking preferential paths, these agents redirect the flow toward previously unswept regions of the reservoir, enhancing microscopic displacement and ultimately increasing oil recovery. Among these agents, O/W emulsions have proven particularly effective in reducing the mobility of water and favorably changing the displacement front [8].

Emulsion injection involves trapping droplets within the porous medium, reducing the effective permeability of the displacing aqueous phase. As illustrated in Figure 1.1, during water flooding, water flows through high-permeability paths where capillary resistance is lower, leaving behind trapped oil. When emulsion is injected, the dispersed phase navigates these preferential paths, restricting the flow as the droplets become trapped. During subsequent water injection, the water is redirected to previously unswept regions of the reservoir, mobilizing trapped oil.

The transport of droplets through porous media significantly alters the flow by changing the dynamics at the pore level, as drops can either move through pore throats or become trapped in pore bodies [15]. Traditional mean-field descriptions of flow in porous media overlook these intricate pore-level interactions, averaging microscopic effects over larger scales and failing to capture small-scale variations [16].

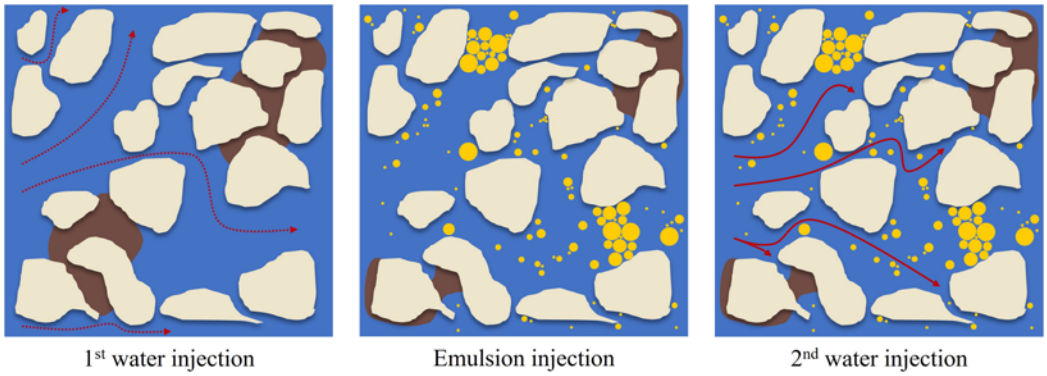

Figure 1.1: Schematic illustration of emulsion injection as an enhanced oil recovery method. The process involves pore blockage during emulsion flooding, which modifies the water's preferential flow paths.

Describing the transport of droplets through individual constrictions involves complex interactions between drop deformation and local hydrodynamic stresses [10, 17]. In emulsion flooding, these complexities are further amplified by droplet-droplet interactions, which introduce long-range forces and result in collective phenomena [18, 19]. Such behaviors challenge straightforward generalizations akin to those found in thermodynamics and statistical mechanics.

To fully understand the flow physics in porous media, it is crucial to observe both macroscopic properties and pore-scale dynamics. While core flooding experiments provide valuable insights into flow behavior, high-resolution imaging techniques like micro-computed tomography are often expensive and time-consuming. Alternatively, microfluidic approaches using porous media analogs offer a practical means to visualize small-scale fluid flow dynamics. Microfluidic experiments allow for precise control over pore structure parameters, such as pore shape, size and distribution [20]. When combined with pressure drop and flow measurements, micromodels offer a detailed correlation between macroscopic transport properties and micro-scale displacement mechanisms.

1.2 Objectives

The objective of this work is to study pore-scale mechanisms governing emulsion flow in porous media. Specifically, the study aims to relate the water phase mobility to the capillary number and emulsion drop size. By employing pore-scale visualization and pressure measurements during the flow of O/W emulsions, we seek to correlate the macroscopic flow behavior with the pore-scale phenomena.

This study adopts a predominantly experimental approach using mi-

crofluidic porous media devices. We fabricate model systems with precisely controlled geometric parameters and prepare polydisperse emulsions with drop-size distributions that match the range of the pore channels. This allows us to assess the effectiveness of emulsion droplets in blocking preferential flow paths. Our goal is to evaluate how the geometric parameters of the porous media and the properties of the injected emulsion impact transport dynamics at different capillary numbers.

1.3 Thesis Outline

The structure of this thesis is organized into six chapters. Chapter 1 introduces emulsion flooding as an EOR method and outlines the objectives of this research.

Chapter 2 covers the fundamentals of microfluidics in multiphase flow, emphasizing surface and interfacial phenomena crucial for small-scale flows. It then explores essential concepts concerning immiscible displacement, elucidating the micro-scale physical phenomena of emulsion flow in porous media. The chapter concludes with a comprehensive literature review on emulsion transport in pore network systems.

Chapter 3 outlines the experimental methodology used to investigate emulsion flow in model porous media. It begins with a comprehensive description of the microfabrication process and the design of the pore network. The chapter then presents the fluid properties, including the procedures for emulsion preparation. A thorough explanation follows on the experimental setups used for each flow configuration. Finally, the chapter discusses the methods used for image acquisition and processing.

Chapter 4 presents the findings from the linear flow tests. It begins with a complete characterization of the linear device, describing its structural properties and surface characteristics. The chapter then discusses the results of the water-mobility tests, providing insights into the dynamics of droplet trapping and subsequent mobilization within the pore space. These results are part of the project "Emulsion Injection as a Flow Diversion Method to Increase Oil Recovery and Reduce Water Production", conducted in collaboration between LMMP and Repsol-Sinopec Brasil.

Chapter 5 examines the results from flow behavior of emulsions in radial micromodels. Similar to Chapter 4, it begins with the characterization of the device including geometric dimensions, pore-size distribution, absolute permeability, and surface wettability. The chapter then presents the findings from the water-mobility flow tests conducted at two distinct capillary numbers,

followed by an analysis of the oil displacement test.

Chapter 6 presents the concluding remarks and suggestions for future work.

2
Literature Review

This chapter presents the fundamentals of microfluidics in multiphase flow, with a focus on surface and interfacial phenomena critical for small-scale flows. Key concepts related to the flow of immiscible fluids elucidate the micro-scale physics underlying emulsion flow in porous media. The chapter concludes with a detailed literature review on the transport of emulsion in pore network systems.

2.1
Microfluidics

Microfluidics is the science and technology of systems that manipulate small amounts of fluids. It involves the design, fabrication, and testing of devices that can precisely control and handle fluids at the micro-scale. Often referred to as lab-on-a-chip systems, these devices integrate multiple laboratory functions, such as mixing, pumping, separating, and analyzing fluids, onto a single chip. Compared to conventional laboratory techniques, microfluidic devices reduce the consumption of samples and reagents, leading to cost savings and minimized waste.

Model porous media devices, commonly known as micromodels, are experimental tools used to simulate the structure and flow characteristics of natural porous media like rock and soils at a controlled and observable scale. These devices are usually made from transparent materials and are molded to create a network of pores and channels that mimic the geometry and connectivity of real porous media. Additionally, experimental conditions can easily be modified, making micromodels versatile tools for studying a wide range of phenomena, from single-phase flow to complex multiphase transport and interactions.

Micromodels are made from transparent materials including glass, silicon, and polymers, such as polydimethylsiloxane (PDMS) and polymethylmethacrylate (PMMA), which allow for direct optical observation of fluid flow and displacement processes within the pore network. The pore structures can be precisely fabricated using techniques like photolithography, etching, or molding, enabling the design of specific pore geometries, sizes, and distribu-

tions. This control facilitates systematic studies of the influence of pore structure on fluid behavior. Micromodels can also be fabricated by packing glass beads between parallel plates (2D) or within a transparent capillary (3D). The ease of surface treatments further aids in investigating wettability effects on porous media flow, which is crucial in petroleum and environmental engineering processes [20].

Fluid flow in microfluidic devices differs significantly from that in macroscopic systems. The dimensions of the channels, typically ranging from tens to hundreds of micrometers, result in a high surface area relative to the fluid volume. This leads to surface forces, such as capillary pressure and surface tension, dominating fluid dynamics; in contrast to larger systems where bulk or body forces prevail. At such a small scale, viscous forces outweigh inertial forces, influencing the behavior of fluids when they come into contact with each other or with the walls of the microchannels. These surface effects cause the flow to deviate from predictions based on larger length scales [16].

Micromodels are instrumental in quantifying pore-scale physics and relating macroscopic transport properties to microscopic displacement mechanisms. The capability to directly visualize fluid behavior at the pore level provides quantitative data on flow patterns, saturation distributions, and other relevant parameters. This data is essential for validating and improving theoretical models and simulations of fluid flow in porous media.

2.1.1 Surface Effects

When immiscible phases coexist in porous media, the surface energy at the fluid interfaces significantly impacts the distribution, saturation, and displacement of the phases. Additionally, the contact angles at which the interfaces meet the solid surface affect how the fluids spread. Together, these factors govern the dynamics of immiscible fluids in porous media, and will be examined in detail in the following sections.

2.1.1.1 Interfacial tension

Attractive van der Waals forces between molecules are felt equally by those in the bulk owing to cohesive interactions. However, molecules at the interface are in a higher energy state due to an imbalance in these forces. This imbalance pulls these molecules toward the bulk, causing the interface to contract and adopt a configuration that minimizes the interfacial free energy. This contracting force is known as interfacial tension.

The resulting curvature of the interface generates a pressure difference, known as capillary pressure, described by the Young-Laplace equation:

$$P_c = \sigma \left(\frac{1}{R_1} + \frac{1}{R_2} \right) \tag{2-1}$$

Where σ is the interfacial tension, and R_1 and R_2 are the principal radii of curvature.

2.1.1.2 Wettability

A liquid with a strong affinity for the solid will maximize its interfacial area and spread to form a film. Conversely, a liquid with weaker affinity will bead up. This property is termed wettability. Wettability refers to the tendency of a liquid to spread on or adhere to a solid surface in the presence of another fluid. It significantly influences capillary forces and fluid flow behavior.

Wettability can be quantified by examining the interfacial forces present when two immiscible phases come into contact with a solid. For oil and water systems on mineral surfaces, the contact angle may range from strongly water-wet ($\theta \sim 0°$) to strongly oil-wet ($\theta \sim 180°$). Intermediate wettability occurs when both fluids tend to wet the solid ($\theta \sim 90°$).

Rock wettability affects fluid saturations and the overall relative permeability characteristics of a fluid-rock system. An example of this effect on saturation is shown in Figure 2.1, illustrating residual oil saturation in both a strongly water-wet and a strongly oil-wet rock [1].

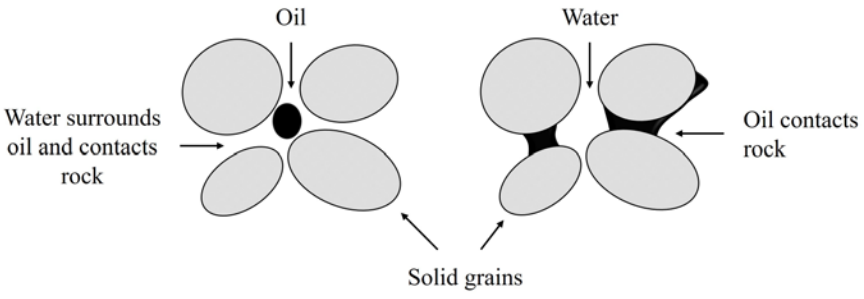

Figure 2.1: Effect of wettability on saturation. Adapted from Green & Wilhite [1].

Reservoir rocks can exhibit intermediate or mixed wettability, depending on the physicochemical properties of the rock and the composition of the oil phase. This variability arises from heterogeneity in the chemical composition of exposed rock surfaces, causing wettability conditions to differ from point to point [1].

2.1.1.3 Capillary pressure

Capillary pressure is a key factor in governing the flow and distribution of fluids within porous media. It arises from the tension at the fluid interfaces, creating a pressure difference across the boundaries. This pressure difference, known as capillary pressure, is defined as:

$$P_c \equiv P_2 - P_1 = \frac{2\sigma cos\theta}{R} \tag{2-2}$$

The capillary pressure is influenced by the interfacial tension between fluid phases (σ), the relative wettability of the fluids (characterized by the contact angle θ), and the size of the capillary (R).

According to Equation 2-2, the pressure on the concave side of the interface (P_2) is greater than that on the convex side (P_1). It indicates that interfacial tension causes an interface with a mean radius of curvature (R) to maintain mechanical equilibrium between two immiscible fluids at different pressures. This principle is crucial for understanding the balance of forces at fluid interfaces in porous media.

2.2 Immiscible Displacement in Porous Media

For slow displacement of immiscible fluids in porous media, the flow is primarily controlled by capillary forces. At the pore scale, capillary pressure dictates how the fluids are displaced and their arrangement within the medium. On a larger scale, it determines the ease with which each phase flows and the extent of fluid displacement.

In drainage, where a non-wetting fluid displaces the wetting phase, capillary forces prevent the non-wetting fluid from spontaneously entering a pore [21, 22]. In the capillary regime, the displacement front advances in sudden and irreversible bursts, known as Haines jumps [23]. In contrast, imbibition, involves the displacement of a non-wetting phase by a wetting fluid. The displacement is strongly dependant on the pore geometry and the surface roughness [24].

The dynamics of immiscible displacement, influenced by both capillary and viscous effects, can be characterized by the capillary number:

$$Ca = \frac{\mu v}{\sigma} \tag{2-3}$$

Which is the ratio of viscous to capillary forces, and the viscosity ratio:

$$M = \frac{\mu_d}{\mu_D} \tag{2-4}$$

Which is the ratio of the viscosity of the defending fluid to that of the invading fluid. Here, μ, v, and σ represent the viscosity, average velocity, and interfacial tension, respectively, while μ_d and μ_D denote the viscosities of the defending and invading fluids, respectively.

When a pressure gradient is applied through porous media, it induces a viscous flow that disrupts the capillary equilibrium. Depending on the relative magnitude of the viscosity ratio, viscous forces can either stabilize or destabilize the fluid interfaces.

In drainage displacements, Lenormand et al. identified three distinct regimes: stable displacement, capillary fingering, and viscous fingering. These regimes are illustrated in Figure 2.2 and depend on the capillary number and the viscosity ratio [25].

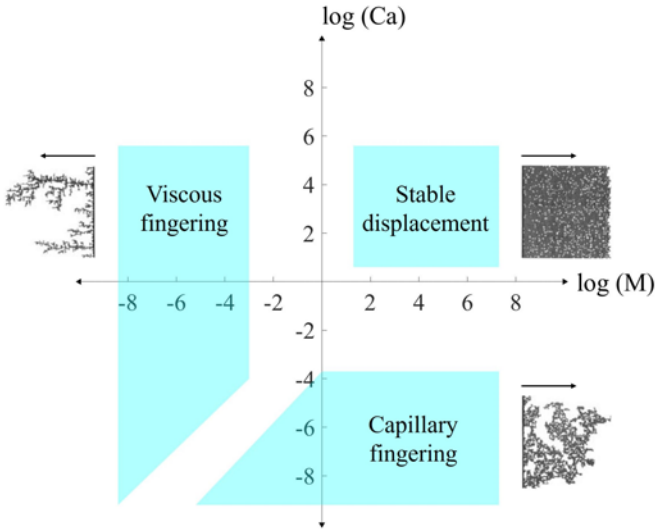

Figure 2.2: Phase diagram for drainage in porous media proposed by Lenormand and Zarcone 2. Adapted from Joekar-Niasar and Hassanizadeh [3].

When a more viscous fluid displaces a less viscous one ($M > 1$), the pressure drop at the displacement front is associated with the invading phase, resulting in either stable displacement or the development of capillary fingering, depending on the capillary number. At low capillary numbers, displacement occurs as capillary fingering. As the capillary number increases, the displacement gradually stabilizes.

For unfavorable viscosity ratios ($M < 1$), at low capillary numbers, the flow is controlled by capillary forces, leading to capillary fingering. However, due to the lower viscosity of the non-wetting invading fluid, viscous fingering dominates the flow at higher capillary numbers.

The displacement pattern in porous media is influenced not only by the viscosity ratio and the capillary number, but also by wettability [26, 27, 28] and the heterogeneity of the pore geometry [4]. This heterogeneity affects the advancing front of the invading phase due to variations in the capillary pressure threshold across the medium [4]. Figure 2.3 illustrates the differences in fingering structures observed in heterogeneous and homogeneous media.

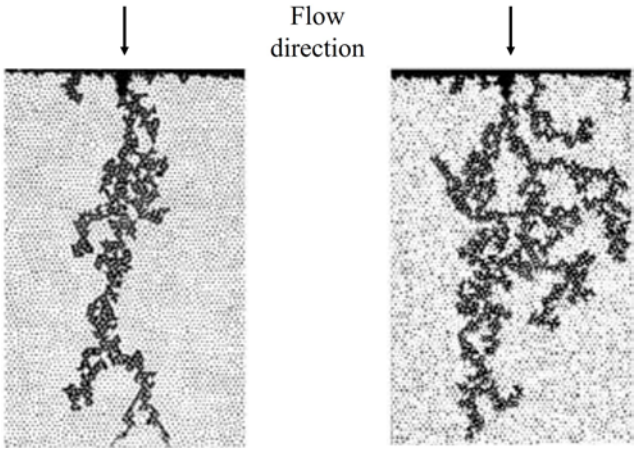

Figure 2.3: Fingering patterns emerged in hydrophilic porous media with homogeneous and heterogeneous porous structure during drainage experiments [4].

Capillary trapping occurs when the non-wetting phase becomes trapped in the pore space as discrete ganglia due to capillary forces. Early explanations for this phenomenon were provided by Jamin [29], who attributed the trapping to capillary forces. Subsequent studies using micromodels identified two main mechanisms of capillary trapping: bypass trapping, which arises from pore-scale heterogeneity, and snap-off trapping, which results from the interplay between capillary and viscous forces [30, 31].

When capillary pressure exceeds a critical threshold, it can cause the formation and trapping of discrete ganglia of the non-wetting fluid [32]. The mobilization of these ganglia depends on reaching a critical capillary number [33, 34]. During drainage, the wetting phase is predominantly trapped through bypass mechanisms. In imbibition, however, the non-wetting phase may be trapped by either bypass, snap-off, or a combination of both mechanisms. The specific trapping mechanism depends on factors such as the local pore structure topology, surface roughness, and capillary number [35].

Additional mechanisms revealed through pore-scale visualization include the study of two-phase flow in vugular porous media [14], mobilization of trapped non-wetting phase in 3D micromodels [36, 37], foam injection as an EOR method [38, 39, 40], polymer flooding [41, 42], and particle transport within porous media [43, 44].

2.3 Emulsions

Colloidal dispersions are two-phase systems consisting of a dispersed phase and a dispersing medium. Emulsions are a specific type of colloidal dispersion involving immiscible liquids, where one liquid (the dispersed phase) is dispersed as small droplets within another liquid (the continuous phase).

Emulsion formation is achieved by effectively homogenizing the oleic and aqueous phases in the presence of a surfactant [45]. This process typically involves intense mechanical agitation of the liquid mixture using devices such as high-shear mixers, high-pressure valve homogenizers, colloidal mills, microfluidizers, or ultrasonic homogenizers [46]. Increased shear force generally results in smaller droplet sizes of the dispersed phase, leading to a more stable and tighter emulsion [47]. In the oil industry, various mixing sources generate significant shear forces during crude oil production.

Emulsions are classified into three main types based on the nature of the dispersed phase: oil-in-water (O/W), water-in-oil (W/O), and double emulsions (Figure 2.4). In oil-in-water (O/W) emulsions, oil droplets are dispersed within a continuous aqueous phase, whereas water-in-oil (W/O) emulsions consist of water droplets dispersed within a continuous oil phase. Double emulsions are more complex systems where small droplets of one phase are dispersed within larger drops of another phase, which are in turn suspended in a continuous phase. Examples include (water-in-oil)-in-water (W/O/W) and (oil-in-water)-in-oil (O/W/O) emulsions [48, 49, 50].

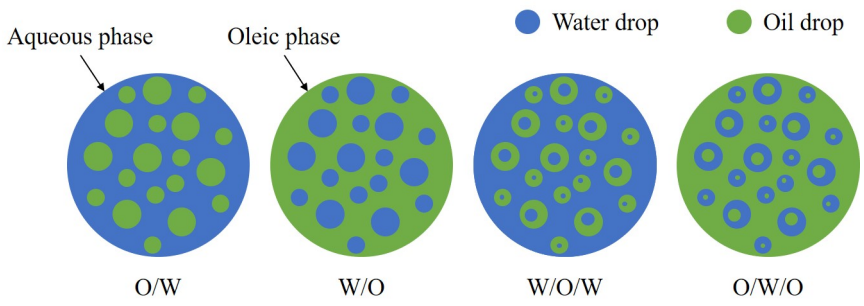

Figure 2.4: Different types of emulsion. Adapted from Martínez-Palou et al. [5].

The type of emulsion formed depends on several factors. Generally, the ratio of oil to water is a key determinant of which phase becomes the dispersed one. The phase with the smaller fraction becomes the dispersed phase, while the larger volume fraction forms the continuous phase. When the phase-volume ratio is close to 1, the presence of emulsifiers and solids can significantly influence the type of emulsion [51].

Emulsions vary based on the size of droplets within the continuous phase. Macroemulsion drops are significantly larger than those in microemulsions, often by several orders of magnitude. Macroemulsions are thermodynamically unstable and do not form spontaneously; they require energy input to form and maintain their dispersed state. Over time, macroemulsions tend to separate back into their stable phases due to their higher interfacial energies. In contrast, microemulsions form spontaneously without requiring high-shear conditions. Their extremely low interfacial tensions allow for the formation of very small droplets, typically 10 nm or smaller. This difference in droplet size and interfacial tension is fundamental to understanding the thermodynamic stability of macroemulsions compared to microemulsions [51, 52].

Emulsions are thermodynamically unstable systems due to the additional energy associated with oil-water interfaces, causing them to separate over time. Achieving kinetic stability over a sufficiently long period requires the use of stabilizing agents. Stabilizers can be classified according to their mode of operation as either emulsifiers or texture modifiers [46]. This work focuses on emulsifiers, which are surface-active agents that adsorb to the surface of emulsion droplets, forming a protective interfacial film that prevents aggregation. Emulsifiers also reduce interfacial tension, facilitating emulsification. Examples of emulsifiers include certain proteins, surfactants, and solid particles.

Surfactants are amphiphilic molecules consisting of a hydrophilic head (polar group) and a hydrophobic tail (non-polar group). When they diffuse to the oil-water interface, the hydrophilic head embeds into the aqueous phase, while the hydrophobic tail extends into the aqueous phase. This orientation reduces the thermodynamic free energy of the system, resulting in more stable emulsions. Figure 2.5 illustrates surfactant molecules accumulating at the interface, stabilizing a water droplet.

Naturally occurring emulsifiers in crude oil, such as asphaltenes and resins, are believed to be the main constituents of interfacial films around water droplets in oilfield emulsions [48, 49, 50]. These molecules contain heteroatoms or polar groups that enhance their surface activity, causing them to accumulate at the oil-water interface [53, 54]. Additionally, mineral solids like fine sands and clay particles act as mechanical stabilizers. Being significantly smaller than

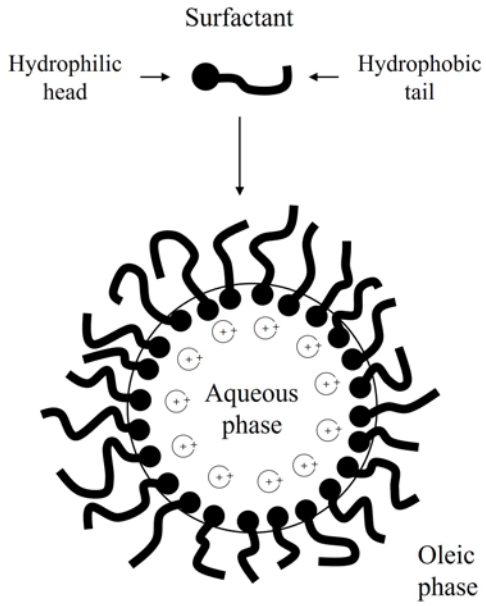

Figure 2.5: W/O emulsion stabilized by surfactants. Adapted from Lee [6].

emulsion droplets, these particles are wetted by both phases and concentrate at the oil-water interface. Their effectiveness in stabilizing emulsions depends on factors such as the solid particle size, interparticle interaction, and the wettability of the solid [55, 56]. The stability of emulsions is also influenced by temperature, drop size, drop-size distribution, pH of water, and brine composition [7].

Another mechanism for stabilizing emulsions involves the external addition of surfactants, which readily adsorb at the oil-water interface to reduce the interfacial tension. In emulsion systems, both natural and synthetic surfactants are employed as emulsifiers.

The kinetic stability of emulsions primarily stems from the formation of protective films at the oil-water interfaces, which mitigate gravitational separation (creaming and sedimentation), aggregation, and coalescence. Creaming and sedimentation occur due to density differences between the two liquid phases. Coalescence results from drops merging with significant changes in their surface area, while aggregation involves drops coming together without such changes. Drops can encounter each other through Brownian motion, sedimentation, or stirring.

Interfacial films act as a protective barrier against drop coalescence. When two drops attempt to merge, this film needs to first drain and rupture. Surfactants slow down the drainage of interfacial films by extending into the bulk phase, as illustrated in Figure 2.6. The steric repulsion generated by the hydrophobic groups of the surfactant molecules forms a physical barrier that prevents droplets from approaching each other and merging [55].

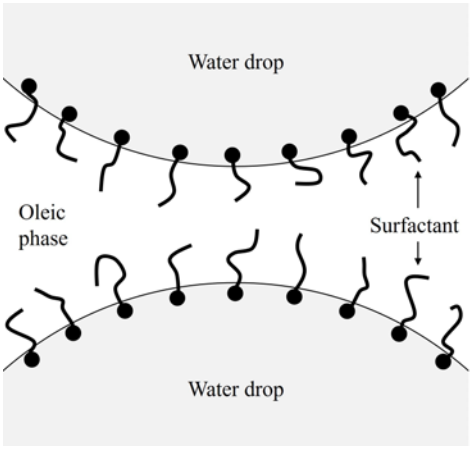

Figure 2.6: Steric repulsion between two water droplets retards film drainage, preventing drop coalescence. Adapted from Kokal [7].

These surfactant molecules also increase the interfacial viscosity and the apparent viscosity of the oil film at the interface, effectively resisting film drainage and inhibiting drop coalescence [7].

2.4 Emulsion Flow in Porous Media

Emulsion plugging occurs when droplets of the dispersed phase become trapped in pore throats as they flow through porous media. Figure 2.7 illustrates the primary capture mechanism for an emulsion droplet when it encounters a pore constriction smaller than its diameter.

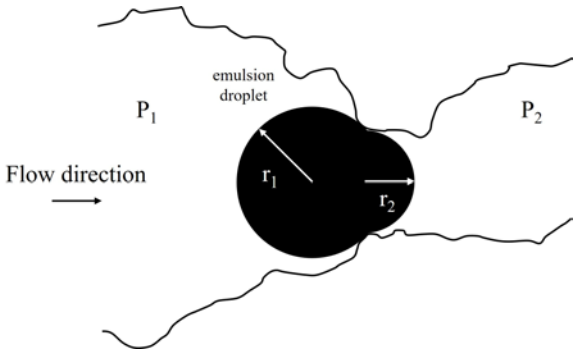

Figure 2.7: Schematic representation of an emulsion droplet entering a pore constriction. Adapted from Mcauliffe [8].

As the droplet passes through the constriction, an additional pressure drop is required to overcome the capillary resistance. This resistance arises from the reduction in the radius of curvature of the droplet tip as it enters the throat region, a phenomenon known as the Jamin effect [57], which is described by the Young-Laplace equation.

In 1973, Mcauliffe investigated the use of crude O/W emulsions as a plugging agent to improve oil recovery during a water flooding field test [58]. This two-year test demonstrated that O/W emulsions effectively increased oil production and favorably altered the flooding pattern. Mcauliffe found that droplets slightly larger than the pore throats reduced water channeling by blocking high-permeability channels, thereby diverting flow into less permeable zones and improving fluid distribution [58, 8].

Mcauliffe also conducted sandstone core flooding tests to examine emulsion permeability behavior [8]. In this work, dilute and stable O/W emulsions were prepared by mixing different asphaltic crude oils with varying concentrations of sodium hydroxide (NaOH) solution and a synthetic surfactant. He observed that emulsions significantly reduced water permeability, with larger drops causing the greatest flow restriction. The rate and degree of permeability reduction were more pronounced at low pressure gradients, indicating non-linear behavior as emulsions flow through porous media.

Numerous studies have investigated the effect of the drop-to-pore size ratio on permeability reduction [8, 13, 59, 10, 11, 60, 61]. These studies consistently show that drops larger than pore throat are more likely to plug pore constrictions and have a more significant impact on reducing permeability compared to smaller drops.

The experimental study by Soo and Radke soo1984flow demonstrates that emulsion flow closely resembles a filtration process [13]. In this process, large drops become trapped in smaller constrictions, while smaller droplets are retained on surfaces or collected in crevices by various physical forces, depending on the surface chemistry of the system [13, 62].

When large drops encounter constrictions smaller than their diameter, they are retained through a mechanism known as straining [13]. Conversely, if droplets are smaller than the pore throats, multiple drops are needed to fully block the constriction. Droplets adsorb onto the pore walls through surface forces, effectively reducing the diameter of the pore throat. As a result, subsequent drops accumulate at the restricted pore throat in a process known as bridging [63]. In cases where droplets are smaller than the pore throats, retention occurs through interception capture [13]. The various pore-trapping mechanisms are illustrated in Figure 2.8.

Furthermore, the flow behavior of droplets is significantly affected by the surface wettability [64]. Wettability affects how droplets interact with the pore walls, and, consequently, the overall efficiency of the plugging or flow behavior.

The ability of large drops to overcome capillary forces and pass through a constriction depends on the capillary number. The effect of the drop-to-pore

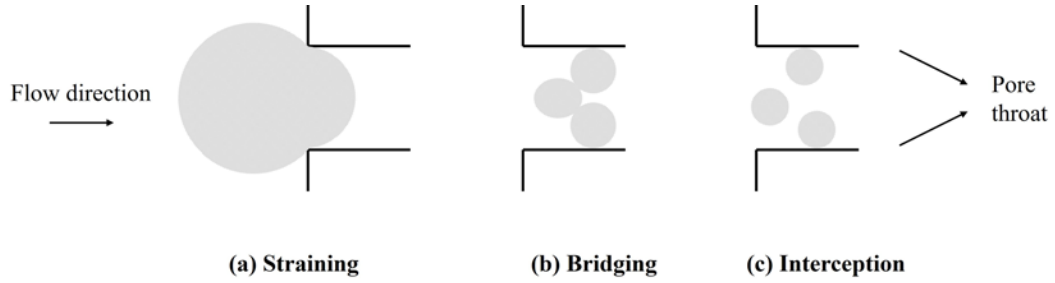

Figure 2.8: Pore trapping mechanisms by drops of varying sizes. (a) Straining occurs when large drops are captured in constrictions smaller than their diameter, (b) bridging involves reducing the effective pore diameter which leads to further accumulation of additional drops, and (c) interception is when smaller droplets are retained on the surface of the pore throats due to surface forces. Adapted from Yu et al.[9].

size ratio on the mobility of O/W emulsions was investigated by Cobos et al. and Romero et al. in micro-channel flow and core flooding experiments. These studies characterized the flow by analyzing the pressure drop-flow rate response at different capillary numbers [10, 11].

Cobos et al. characterized the effect of drop-to-pore throat size on emulsion flow by introducing the mobility reduction factor, which is the reciprocal of the resistance factor. It is defined as the ratio of the steady-state pressure drop of the continuous phase flow (ΔP_c) to that of the emulsion flow (ΔP_e) measured at the same flow rate [10]. The mobility reduction factor serves as a scale for describing the water mobility reduction associated with the trapping of droplets.

Experimental tests conducted by Cobos et al. and Guillen et al. demonstrated that for droplets larger than the pore throats (represented by the red curve in Figure 2.9), the mobility reduction factor exhibits a strong dependency on the capillary number [10, 65]. They reported a critical capillary number below which the mobility reduction factor (f) decreases sharply, indicating partial blocking (Figure 2.9). Above this critical value, the viscous pressure is sufficient to overcome the capillary resistance needed to deform the drops ($f \to 1$). Below this threshold, the mobility reduction factor reflects the additional pressure drop required to deform the droplets as they flow through pore constrictions. In contrast, for droplets smaller than the pore throats (represented by the blue curve in Figure 2.9), the mobility reduction factor shows little dependence on the capillary number ($f \sim 1$).

The effect of the capillary number on the mobility of O/W emulsions was further investigated by Guillen et al [65]. Displacement tests involved alternating the injection of water and emulsion through sandstone cores at two different capillary numbers. At a low capillary number, part of the oil was

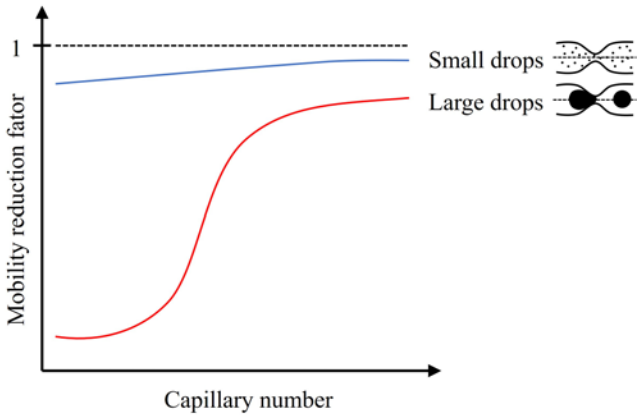

Figure 2.9: Schematic representation of the mobility reduction factor, f as a function of the capillary number [10, 11]. Adapted from Cobos et al. [10].

mobilized following the injection of the emulsion slug, suggesting that emulsion plugging diverted the water to new flow paths. Conversely, at a high capillary number, successive cycles of water and emulsion injection had minimal impact on oil recovery, indicating that emulsion droplets had little effect on fluid mobility. Figure 2.10 illustrated the oil recovery at both capillary numbers.

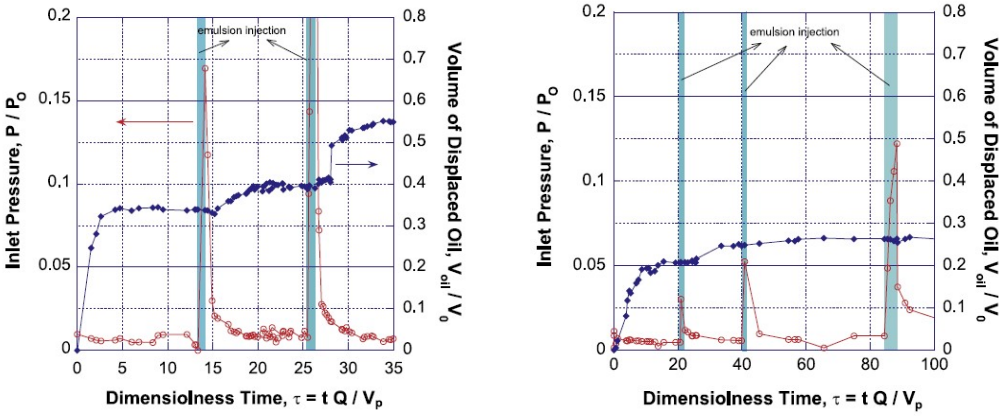

(a) Low capillary number test, $Ca = 2 \times 10^{-5}$.

(b) High capillary number test, $Ca = 2 \times 10^{-4}$.

Figure 2.10: Injection pressure and oil recovery factor at low and high capillary numbers [12].

Guillen et al. conducted additional investigation into oil displacement by visualizing the flow through model porous media devices. They analyzed the mobilization of residual oil during alternating water and emulsion injection (WAE) [12]. Microscopic observations revealed that emulsion droplets partially blocked the initial flow paths, redirecting the flow to previously unswept areas of the micromodel. This pore blockage also affected the average mobility of the water phase, resulting in a more uniform sweep, as depicted in Figure 2.11.

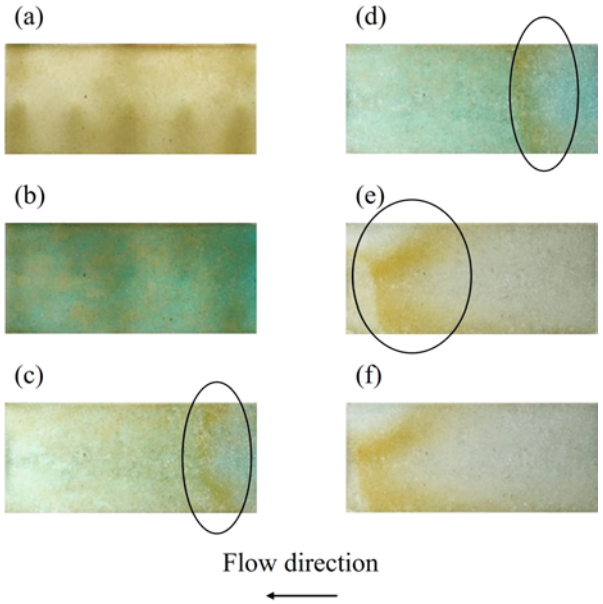

Figure 2.11: Images of transparent porous media at different stages of water and emulsion injection: (a) porous media originally saturated with oil; (b) porous media during water flooding; (c) oil bank after emulsion injection; (d-f) stable oil bank is produced from the injection of emulsion. Adapted from Guillen et al. [12].

The mobility reduction factor has been effectively used in modeling permeability decline to describe flow rate-pressure drop relationship of emulsion flow [11, 66]. Generally, the literature agrees that higher flow rates lead to increased droplet mobility [63, 60]. Experimental data indicate that at higher flow rates, the local pressure gradient becomes more pronounced, allowing larger droplets to be squeezed through pore constrictions more effectively [10].

Experiments conducted by Ding et al. revealed two primary flow regimes, distinguished by a critical threshold pressure, defined as the capillary force required to initiate emulsion flow. Below this critical pressure drop ($Ca < 10^{-4}$), viscous forces are generally insufficient to overcome capillary resistance for most drops, allowing only smaller droplets, which encounter less resistance, to flow through the pore throats. Above this critical pressure drop ($10^{-4} < Ca < 10^{-2}$), trapped drops begin to deform and re-enter the flow stream. These droplets may either become trapped again or continue moving, potentially leading to the re-blocking of pore throats due to the Jamin effect. When the capillary number exceeds this limit ($Ca \geqslant 10^{-2}$), viscous forces start to significantly influence emulsion flow. As the pressure difference increases at higher capillary numbers, droplets begin to squeeze through progressively smaller constrictions. At very high velocities, droplets undulate through the porous medium, opening multiple flow paths and significantly improving emulsion flow efficiency [61]. Soo and Radke observed that while this process

appears continuous, it actually consists of a series of capture events followed by the re-entrainment of captured droplets [67]. The findings of Ding et al. [61] align well with the discussed mobility reduction factor.

Capillary resistance is further influenced by oil-water interfacial tension. It has been established that interfacial tension affects both the depth of emulsion penetration into a porous medium [68, 69] and the effectiveness of droplets in plugging pores [69]. Yu et al. reported that emulsion droplets with higher interfacial tension are more effective at plugging pore throats because they are less deformable [60]. Furthermore, Ding et al. demonstrated that emulsions with higher interfacial tension lead to a sharper initial increase in pressure and higher stable pressure difference during emulsion injection [61].

Most studies have predominantly attributed the plugging mechanism to the Jamin effect. However, additional frictional forces at the contact between the droplet and the wall significantly impact the local pressure across the pore throats. Chen et al. reported that frictional forces arise from the viscosities of both the dispersed and continuous phases. The frictional resistance within a pore throat depends on the oil viscosity, flow velocity, drop size, and pore throat geometry [70].

The increase in pressure drop is influenced by both capillary and frictional forces within the pore throat. Capillary forces arise from the pressure difference across the droplet, while frictional resistance is due to interactions between the droplets and the pore walls, as well as the bulk viscosity of emulsions. However, studies indicate that the increase in bulk viscosity alone has only a minimal effect on the overall pressure drop and plugging effect [9].

In addition to the frictional forces, the total flow resistance is significantly influenced by the number of droplets flowing through porous media [13, 71, 61]. Emulsion concentration, often referred to as emulsion quality, and the volume of injected emulsion, known as slug size, both play significant roles. Ding et al. experimentally demonstrated that permeability reduction increases with larger slug sizes [68, 61]. Moreover, concentrated emulsions increase flow resistance due to the greater number of droplets available to become trapped in the pore throats [61].

2.4.1 Modeling of Emulsion Flow in Porous Media

Numerous researchers have investigated the flow dynamics of emulsions in porous media to develop analytical models that accurately characterize their behavior. Homogeneous models treat emulsions as a continuous single-phase liquid and do not account for interactions between droplets and pore walls.

Alvarado and Marsden proposed a model based on effective viscosity, treating emulsion as a continuous fluid [72]. This rheological model describes the flow of non-Newtonian emulsions through porous media by correlating rheograms obtained from both capillary tubes (shear stress vs. shear rate) and porous media (pressure drop vs. flow rate). A fitting procedure was developed to align these rheograms. For shear rates ranging from 10^3 to 10^4 s^{-1}, O/W emulsions were observed to behave as Newtonian fluids at dispersed phase concentrations below 50%, while higher concentrations resulted in pseudo-plastic behavior. Mcauliffe similarly attributed this non-Newtonian behavior to droplet-droplet interactions [8]. To model the flow of Newtonian emulsions, Alvarado and Marsden proposed a modified Darcy equation that accounts for permeability reduction due to partial plugging in porous media. However, this viscosity model does not consider interactions between emulsion droplets and pore walls, nor does it account for capillary resistance in the flow [72].

The drop retardation model, initially described by Devereux for constant pressure flow and later by Soo and Radke for constant velocity flow, effectively captures permeability changes during emulsion flow [73, 62]. According to this model, permeability is expected to return to its original value once the emulsion flow ceases and the porous medium is flushed with the continuous phase. However, experimental findings revealed that droplets were often permanently trapped within the porous media, and flushing with the continuous phase did not fully restore the original permeability [62].

Radke and colleagues made significant contributions to the study of emulsion flow in porous media, grounding their research in deep bed filtration theory [13, 67, 62, 74]. Their work identified two primary mechanisms of droplet capture: straining and interception. Straining occurs when drops with sizes comparable to the pore diameter become lodged in constriction sites. In contrast, interception involves smaller droplets retained in crevices or on surface sites due to surface forces. These mechanisms can interact; for instance, interception can reduce the effective pore diameter, leading to increased straining of additional droplets in emulsion flow [62, 9]. Figure 2.12 illustrates these capture mechanisms.

Dong and colleagues extended the filtration model to capillaries of varying diameters, developing the filtration capillary model [68, 61, 9, 71]. The model incorporates the pore geometry, drop size, emulsion concentration, droplet-pore wall interaction, oil-water fraction, interfacial tension, oil viscosity, and the permeability and length of the sand pack. Additionally, it accounts for the injection rates and volumes of the injected emulsion. While Radke's model is effective for very dilute emulsions (1% oil concentration),

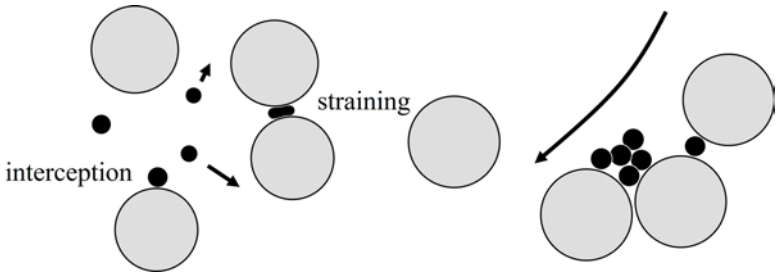

Figure 2.12: Capture mechanisms of emulsion flow in porous media. Adapted from Soo and Radke [13].

Dong's model provides a better fit with experimental data for higher emulsion concentrations, up to 20% [75].

Several network models have been proposed to describe permeability reduction in porous media. Among these, Romero et al. developed a network model for the flow of monodisperse O/W emulsion [11]. This model is based on experimental data from constricted capillary flow studies conducted by Cobos et al. and uses the flow rate-pressure drop relationship to characterize emulsion flow. The mobility reduction factor (f) is derived from this relationship, accounting for changes in local capillary mobility caused by droplet deformation. The model provides qualitative predictions that align with experimental data and effectively captures the flow dependence on local capillary numbers.

Nogueira et al. extended the model developed by Romero et al. by incorporating the volume fraction of the dispersed phase within each node of the network [66]. Nogueira et al. demonstrated that injecting the continuous phase can restore the permeability of the network, either fully or partially, depending on the flow rate.

3
Materials and Methods

This chapter outlines the experimental methodology developed to investigate the transport of polydisperse O/W emulsions in model porous media. The study examines the transport behavior of emulsions in both linear and radial flow configurations, utilizing micromodels with different geometries.

First, the fabrication process of the microfluidic devices is detailed, along with a general description of the pore network design. Next, the properties of the fluids are presented, and the procedures for emulsion preparation and injection are described. Finally, the methods employed for image processing and data analysis are discussed.

3.1
Fabrication of Microfluidic Devices

The microfluidic devices were fabricated from polydimethylsiloxane (PDMS, Sylgard 184 Elastomer Kit, Dow Corning, Germany) using soft lithography technique [76, 77]. The complete process, illustrated in Figure 3.1, comprised two main steps: creating the master mold of the desired geometry and replicating the mold into PDMS micromodels.

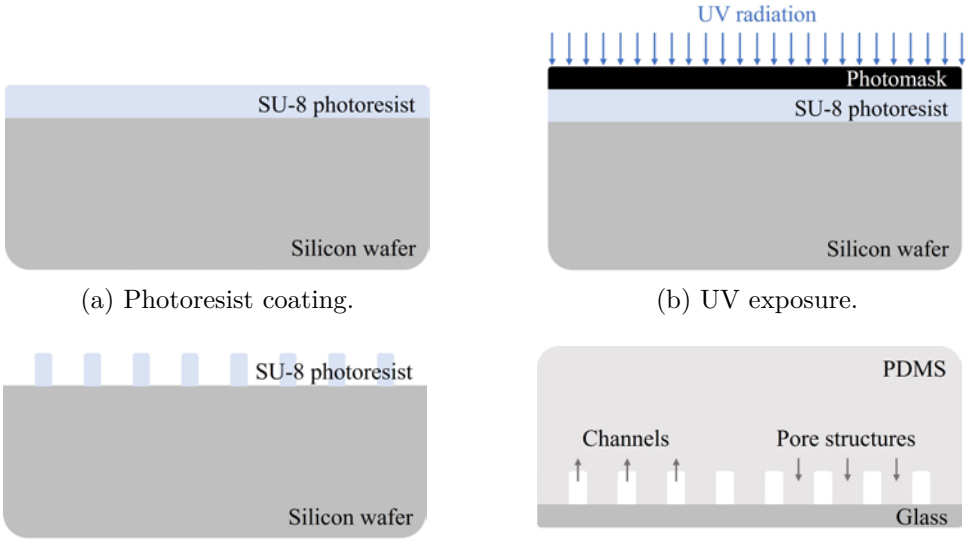

(a) Photoresist coating.

(b) UV exposure.

(c) Chemical development.

(d) Micromodel replication.

Figure 3.1: Schematic illustration of the soft lithography technique.

3.1.1 Master Mold Preparation

A two-dimensional pattern was designed and printed onto a photomask to create the master mold. A high-contrast, epoxy-based, negative photoresist (SU-8 2000, Kayaku Advanced Materials, USA) was spin-coated onto a silicon wafer using a WS-650-23B Spin Coater (Laurell Technologies, USA). The coated substrate underwent baking steps to generate a solid layer of uniform thickness, as illustrated in Figure 3.1a. Parameters such as rotation speed, acceleration, and SU-8 viscosity were adjusted to achieve the desired thickness of the photoresist layer.

The porous medium design was imparted to the wafer by exposing the SU-8 to UV light (UV-KUB 2, Kloé, France) through the photomask (Figure 3.1b). Upon exposure to a 365 nm wavelength, the photoactive components within SU-8 initiated cross-linkage. The exposure time was adjusted based on the layer thickness and the lamp power. Areas of the mold exposed to UV light underwent hardening, while unexposed regions were washed away during chemical development. Next, the mold was submitted to the initial baking steps and developed using propylene glycol monomethyl ether acetate (PGMEA) (Figure 3.1c). Finally, the mold was dried with compressed air and heated to 120 °C for 10 minutes. Specific conditions for each geometry are summarized in Table 3.1.

Table 3.1: Parameters utilized in the mold fabrication of both linear and radial micromodels.

Geometry	**Linear**	**Radial**
Photoresist	SU-8 2075	SU-8 2025
Spin-coating conditions	2,100 rpm @ 30 s	1,000 rpm @ 30 s
Baking temperatures	1^{st} step - 65° C @ 5 min 2^{nd} step - 95° C @ 18 min	1^{st} step - 65° C @ 3 min 2^{nd} step - 95° C @ 9 min
Mold thickness	100 μm	80 μm
UV exposure conditions	84% @ 8 s	50% @ 12 s

SU-8 photoresist underwent three baking steps throughout the process, each serving a distinct purpose. The soft bake, following spin coating, aimed to evaporate the solvent, preparing the photoresist for UV radiation exposure. The second bake, post-UV exposure, activated the photoactive components in SU-8 through radiation, with subsequent heat sustaining the reaction. The final step, the hard bake, involved exposing the photoresist to high temperatures to suppress internal stresses, thereby preventing surface cracks.

Photoresists are sensitive to temperature changes, as rapid changes can induce cracks on the surface. To mitigate mechanical stress, a temperature ramp was adopted, with a first plateau at 65 °C followed by a second at 95 °C. The duration of each plateau was determined by the desired thickness of the photoresist layer.

The preparation of the master mold is the most critical step in the microfabrication process. This step requires meticulous execution within a clean room to avoid any contamination of the porous medium etched onto the silicon wafer. Additionally, specialized printing is needed to generate a high-resolution photomask to achieve accurate replication of the micro-scale geometries within the porous medium. In this work, the fabrication of the master mold was conducted in-house, while the printing of the photomasks was outsourced.

3.1.2 Micromodel Replication

The subsequent step involved fabricating PDMS micromodels using the mold from the previous step. Liquid PDMS was mixed with a reticulating agent (Sylgard 184 Elastomer Kit, Dow Corning, Germany) at a 10:1 polymer-to-cross-linker ratio and then degassed under vacuum to eliminate any trapped air bubbles. After degassing, the PDMS mixture was gently poured onto the SU-8 mold and transferred into an oven set at 80 °C for 2 hours to cure. Once cured, the hardened PDMS replica was carefully peeled off the mold, shaped into the desired configuration, and punched to create inlet and outlet holes. The PDMS surface was cleaned using Scotch Magic™ tape (3M, USA).

Before sealing, a thorough cleaning of the glass slides was conducted using acetone followed by drying with compressed air. The prepared surfaces were then exposed to low-pressure air plasma (500 mTorr, 30W, 2 min) using a plasma cleaner (PDC-001, Harrick Plasma, USA) to induce surface activation. Plasma treatment generates Si-OH polar groups on the PDMS surface, facilitating robust and permanent Si-O-Si bonding with the glass slide surface.

Figure 3.1d illustrates the micromodel after bonding. The resulting PDMS device has channels of 100 μm width and uniform height, equal to the height of the SU-8 photoresist layer. Single-use devices were fabricated for each experiment to ensure consistency and accuracy.

3.2 Model Porous Media

Two-dimensional micromodels were employed for visualizing and investigating pore-blocking mechanisms caused by emulsion drops flowing through porous media. The devices were designed in two distinct geometries, allowing both linear and radial flows to be studied. Images of the photomasks are shown in Figure 3.2. The designs were created using AUTOCAD® and the photomasks were printed at a resolution of 3000 dpi.

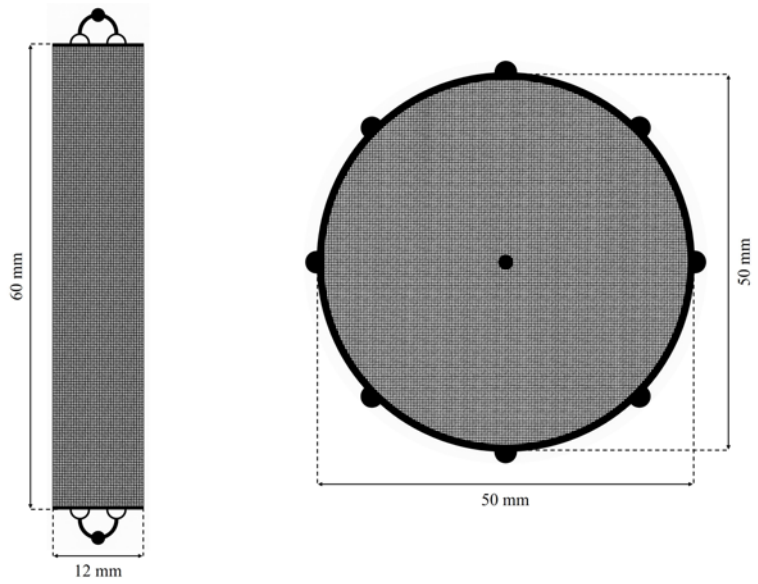

Figure 3.2: Two-dimensional micromodels designed with linear and radial flow configurations to study emulsion flow in porous media.

3.2.1 Porous Media Design

The porous medium consists of a structured network with both straight and constricted channels. Wide regions, known as pore bodies, are connected by narrower constrictions or straight channels, referred to as pore throats. The constrictions are randomly placed within a regular grid of evenly spaced square posts, forming a square-shaped unit cell. The channels have a square cross-sectional profile, measuring 100 μm in both depth and width, except for the constrictions, which measure 45 and 75 μm in width. Figure 3.3 illustrates the unit cell and a localized section of the pore network, highlighting the distribution of constriction sizes.

The posts have a square profile and rounded corners, measuring approximately 200 $\times$ 200 μm^2 in area, apart from the protrusions. An image of the micropatterned PDMS surface is shown in Figure 3.4.

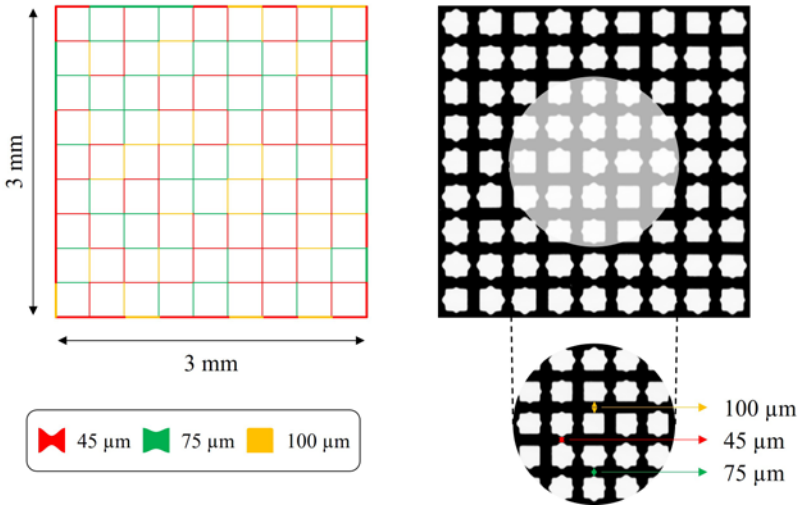

Figure 3.3: Details of the pore network design: on the left, a schematic illustration of the unit cell shows the distribution of both straight and constricted channels, with each color corresponding to a distinct size. On the right, an image of the pore space illustrates the grid cell arrangement, with posts depicted in white and channels in black.

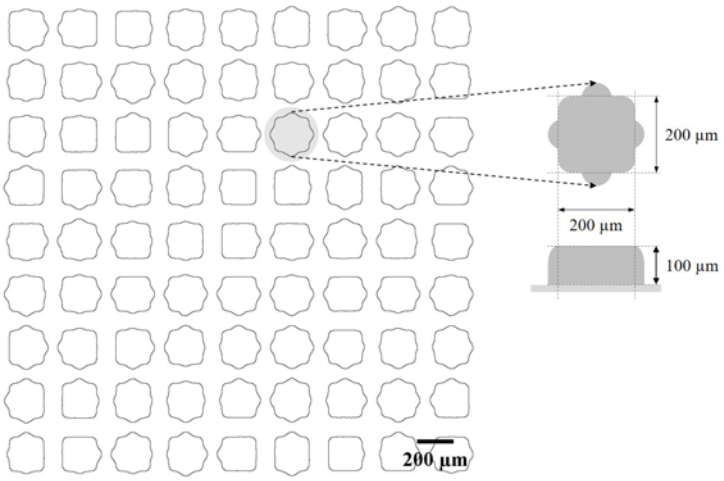

Figure 3.4: Micropatterned PDMS surface with a square lattice of posts. Square posts measuring 200 × 200 in area μm^2 and 100 μm in height.

3.2.2 Characterization of the Pore Network

Confocal laser scanning microscopy (CLSM) was utilized to analyze the geometric characteristics of the device after fabrication. It included determining the average height of the channels, distribution of channel sizes, porosity, and pore volume.

3.2.2.1 Average height of the channels

The height of the channels was obtained by identifying the z-position of each surface enclosing the pore space. Figure 3.5 shows a tile with the PDMS surface on top and the glass surface at the bottom. The local height represents the average height of the channels comprising each tile.

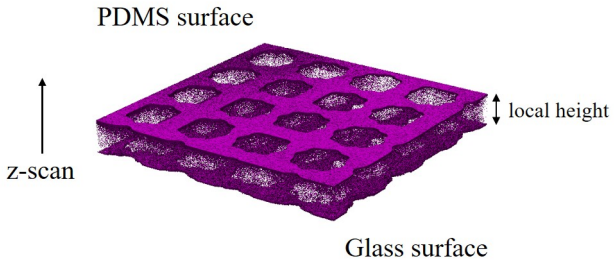

Figure 3.5: A tile illustrating the PDMS (top) and glass surfaces (bottom) surrounding the pore space.

The imaging process involved using a 488 nm laser to image a device saturated with air. Both PDMS and glass reflect light near the incident wavelength of the laser due to the interaction of light with their surfaces. The reflected light was detected by a photomultiplier tube (PMT) sensitive to light close to the 488 nm laser line. The detection window ranged from 478 to 498 nm.

The grayscale value was measured across each z-stack, quantifying the intensity of light captured by each pixel. Within these measurements, highly reflective areas corresponding to the surface of both materials were identified, leading to high-intensity peaks of light (refer to Figure 3.6).

Image acquisition involved segmenting the pore space into lateral images (tiles), with each tile comprising several stacks. By plotting the light intensity relative to the vertical distances from each tile, the local height was determined by subtracting the position of both surfaces, as illustrated in Figure 3.6. The average height of the channels was then computed by combining data from all tiles.

This method, as proposed by Escalante, was validated using two commercial glass micromodels: Dolomite® and Micronit®, with channel heights of 100 and 20 μm, respectively [14].

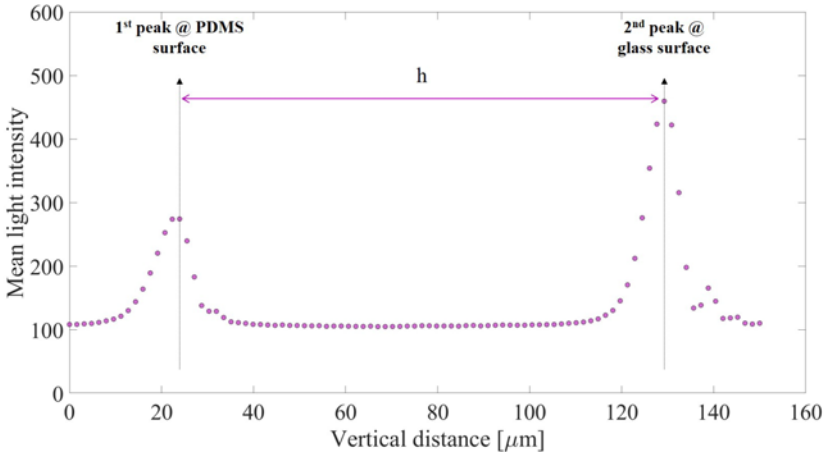

Figure 3.6: Grayscale values across a stack illustrating high-intensity peaks corresponding to the PDMS and glass surfaces, respectively. The average height within each tile was determined by subtracting the vertical position of the surfaces.

3.2.2.2 Channel size distribution

A complete image of the pore network was utilized to measure the width of the channels through image processing techniques. The distribution of channels was then determined by applying the Gaussian mixture model routine, a clustering algorithm available in MATLAB®. This model provided probabilistic assignments for each size category, comprising small constriction (45 μm), large constriction (75 μm), and straight channel (100 μm).

3.2.2.3 Porosity and pore volume

High-resolution images of the porous medium were obtained using CLSM, enabling a detailed visualization of the pore network. To ensure accurate porosity calculation, pre- and post-processing steps were performed to effectively separate the pore channels from the background. Different threshold methods were assessed, and the most suitable one was selected. Further details regarding this methodology are available in Section 3.5.2.1. Subsequently, the image underwent binarization, and the pixels representing the pore structures were computed separately from those corresponding to the pore channels. The total area of the pore network was then determined by summing the segmented regions. The porosity (ϕ) was calculated using Equation 3-1:

$$\phi = \frac{A_{total} - A_{matrix}}{A_{total}} \tag{3-1}$$

where A_{total} represents the total area of the pore network and A_{matrix} is the area occupied by the solid posts. Finally, the pore volume was determined by multiplying the porous area by the average height of the channels.

3.2.2.4 Absolute permeability

The absolute permeability of the micromodels was determined experimentally by injecting an aqueous solution at different flow rates and measuring the corresponding steady-state pressure drop across the pore network. The absolute permeability was then obtained using Darcy's law, which mathematically relates the flow rate of a fluid through a porous medium to the permeability of the medium, the viscosity of the fluid, and the pressure gradient driving the flow:

$$Q = \frac{KA}{\mu L}\Delta P \tag{3-2}$$

where Q is the flow rate, K is the absolute permeability, A is the cross-sectional area of the porous medium, μ is the fluid viscosity, L is the length of the porous medium, and ΔP is the pressure drop. Permeability is typically presented in the Darcy unit system, where 1 Darcy is approximately 0.987×10^{-12} m^2.

3.2.2.5 Surface wettability

Untreated polymers typically have low surface energy, which hinders wetting and interaction with polar groups. Plasma treatment introduces polar functional groups to these surfaces, significantly enhancing their bonding capabilities and hydrophilic properties. These modifications primarily affect the top molecular layers (approximately 100 $\mathring{A}$) of the material, while preserving its bulk properties [78].

In PDMS, plasma treatment breaks the Si-CH_3 bonds, replacing them with Si-OH (silanol) groups, rendering the surface hydrophilic. However, this hydrophilic effect is temporary, lasting around 8 hours [79], as the Si-OH groups gradually revert to their original state, restoring the hydrophobic nature of PDMS. Conversely, plasma treatment on glass removes organic contaminants and other residues, significantly increasing its overall surface energy. This treatment generates hydroxyl (OH) groups on the glass surface, enhancing its interaction with water molecules. Unlike PDMS, the hydrophilic effect on glass is more stable and long-lasting.

The inherent hydrophobic nature of untreated PDMS results in a water contact angle greater than 90°, while glass, due to its higher surface polarity, exhibits a contact angle less than 90°. To evaluate the wetting properties of PDMS and glass with other fluids other than water, contact angle measurements were conducted using the sessile drop method. Figure 3.7 illustrates the experimental setup mounted on the Tracker® Standard Drop Tensiometer (Teclis Scientific) employed for measuring the contact angles.

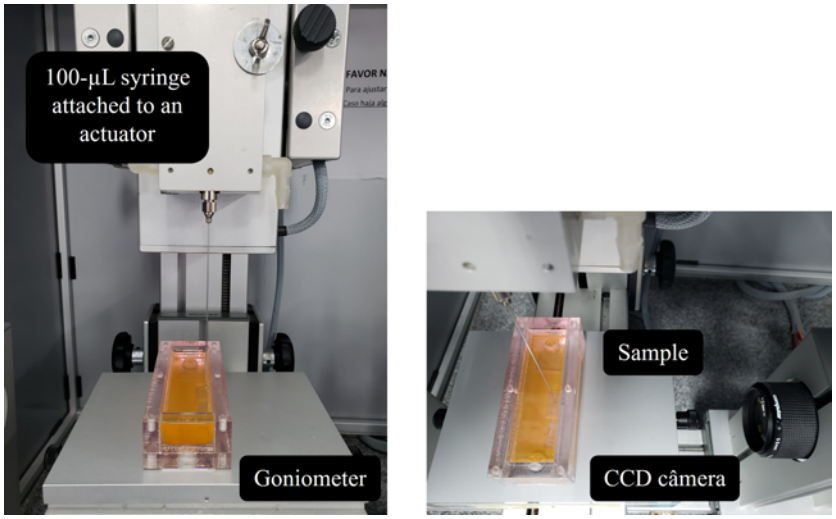

Figure 3.7: Schematic representation of the experimental setup for contact angle measurements using the sessile drop method. The setup includes a 100-μL syringe attached to an actuator for precise droplet placement and a CCD camera positioned in front of the goniometer for capturing images of the droplet on the material surface.

A 5-μL drop of fluid was carefully deposited onto the substrate using a 100-μL syringe attached to an actuator to ensure precise and symmetrical placement. A CCD camera positioned in front of the goniometer captured images of the drop on the surface of the material. The software then automatically analyzed these images, determining the contact angle based on the shape of the drop at its boundary. To ensure reproducibility, the procedure was repeated twice with different drops at varied locations on the surface.

To maintain consistent surface conditions across both materials, PDMS and the glass slide were prepared using identical procedures employed during microfabrication. Contact angles were measured in both a dry environment and inside a transparent cell filled with the oleic phase (DKL7 + OG22). The dry environment simulated the conditions of the water-mobility tests, while the submerged setup replicated the conditions of the oil displacement test (refer to Figure 3.7).

3.3 Fluids

This study focused on the injection of stable O/W emulsions - oil drops dispersed in a carrier phase of surfactant solution - in porous media. The aqueous phase was prepared by adding methylene blue (MB^+, Sigma Aldrich) and sodium dodecyl sulfate (SDS, Sigma-Aldrich) to Mili-Q water at concentrations of 12.5 μM and 14.2 mM, respectively. SDS served as a surfactant to stabilize the emulsions. The oleic phase consisted of 0.1 vol.% Oil-Glo (Spectroline) in Drakeol 7, a light mineral oil. As both fluids are transparent, MB^+ and Oil-Glo were incorporated in each phase to enhance visualization. Two different Oil-Glo dyes were employed to distinguish between the oleic phase of the oil displacement tests and the one utilized as the dispersed phase of the emulsion system. Refer to Table 3.2 for a summary of their properties.

Table 3.2: Properties of the aqueous and oleic phases measured at 21° C.

Fluid phase	**Aqueous**	**Oleic**	**Dispersed oleic**
Components	Mili-Q + SDS + MB	DKL7 + OG 33	DKL7 + OG 22
Density [g/cm^3]	9.99×10^{-1}	8.45×10^{-1}	8.45×10^{-1}
Viscosity [mPa.s]	$9.55 \times 10^{-1} \pm 0.0078$	18.29	18.29

After preparation, the fluids underwent filtration using Milipore® membranes to eliminate dust and other micrometer-sized particles. The aqueous phase was filtered through a 0.45 μm membrane, while the oleic phase was filtered through a 5 μm membrane. The phases remained fully immiscible throughout the experimental timescale.

The critical micelle concentration (CMC) of the aqueous phase solution and the interfacial tension (IFT) between the aqueous and both oleic phases were measured using the Wilhelmy plate method (DCAT 25 Tensiometer, DataPhysics Instruments, Germany). The IFT of both systems measured at the concentrations listed above is presented in Table 3.3.

Table 3.3: Interfacial tension of the aqueous and oleic phases measured at 21° C.

Fluid phase	**Aqueous and oleic**	**Aqueous and dispersed oleic**
IFT [mN/m]	3.25 ± 0.010	8.78 ± 0.024

The CMC was determined by conducting surface tension measurements at varying SDS concentrations while maintaining a fixed concentration of MB^+

(refer to Figure 3.8). It is known that the addition of MB^+ to the aqueous phase significantly reduces the CMC of SDS in water [80]. This phenomenon is ascribed to the strong interaction between MB^+ and SDS, leading to the formation of complexes with an enhanced propensity to reside at the interface and reduce the water solubility. At the MB^+ concentration of 12.51 μM, the CMC was 0.26 mM, as highlighted in Figure 3.8. A concentration of 14.22 mM of SDS was used to ensure the complete emulsification of the system. This concentration facilitates the formation of micelles and enhances emulsion stability. Micelle formation is energetically favorable as it removes hydrophobic tails from direct contact with water, thereby lowering the overall energy state of the system.

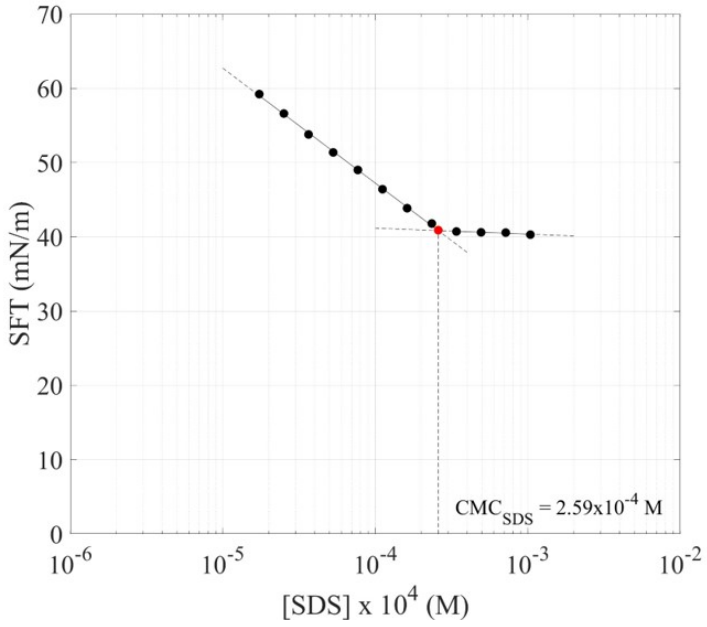

Figure 3.8: Surface tension of the aqueous phase (Mili-Q water + 12.51 μM MB^+) as a function of SDS concentration.

3.3.1 Emulsion Preparation

Each O/W emulsion batch was prepared by mixing 50 mL of oleic phase with 50 mL of aqueous phase in a high-shear mixer using an 18-mm rotor-stator dispersing tool (Dispersing Element S25N-18G, IKA) for 60 seconds. After mixing, a concentrated emulsion was obtained by setting the formed emulsions to rest in a funnel to drain the continuous aqueous phase. The concentrated emulsion obtained after this process had a dispersed phase concentration of 85%.

Because of the lower density of the oleic phase, the dispersed drops do not remain uniformly distributed in the aqueous phase. The gravitational segregation compromises the emulsion injection at a fixed dispersed phase concentration. To avoid this problem, the O/W emulsion was kept in the injection syringe at a very high dispersed phase concentration, which prevents movement of the dispersed phase. The injected concentrated emulsion was diluted inline by mixing it with a stream of the continuous phase.

To study the effect of drop-size on pore blocking and mobility reduction, emulsions with two different drop-size distributions were prepared using different rotor speeds, as shown in Table 3.4.

Table 3.4: Formulation and emulsification conditions of the O/W emulsion systems.

Oleic phase	**Aqueous phase**	**O/W fraction**	**Emulsification conditions**	**d(n,90)**
Drakeol 7 + OG 33	Mili-Q water + SDS + MB	50/50	3,000 rpm @ 60 s 4,000 rpm @ 60 s	~ 80 μm ~ 60 μm

The drop-size distribution was determined by analyzing images from 10 drop samples of 2 μL from each emulsion batch. A custom MATLAB® routine was developed in-house to calculate the number-based drop-size distribution of the emulsions from microscopic images. The Circular Hough Transform (CHT) technique, implemented using the *imfindcircles* function, was employed due to its effectiveness in scenarios where circles exhibit variability in size or lack clear edge definition [81]. Visualization of the identified circles on the original image was then facilitated by the *viscircles* function.

The drop-size distribution of both systems is presented in Figure 3.9. Statistical analysis shows the relative distribution of the number of drops in the range of size classes through the use of histograms. The emulsion prepared at 4,000 rpm is termed small-drop emulsion. Half of the drops have diameters smaller than 24.6 μm and only 10% of the drops have diameters larger than 60 μm ($d_{90} \approx 60$ μm). The system prepared at 3,000 rpm is designated as the large-drop emulsion, presenting a wider drop-size distribution, as expected, with $d_{90} \approx 80$ μm.

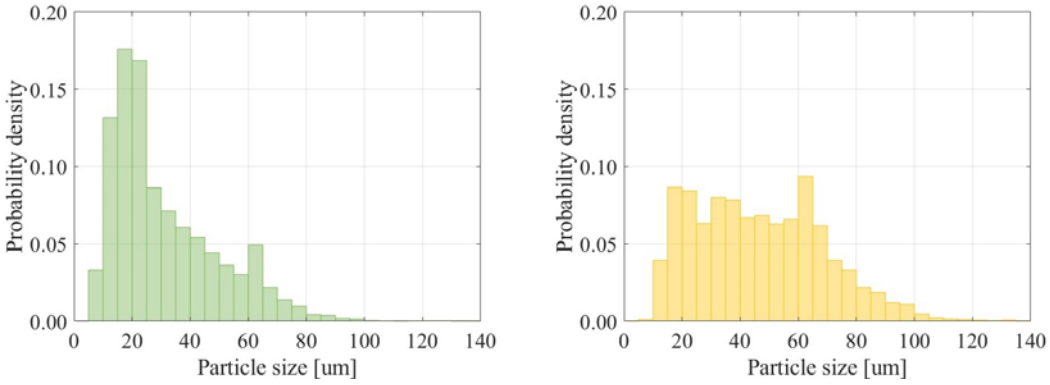

(a) Small drop emulsion. (b) Large drop emulsion.

Figure 3.9: Histogram depicting the drop-size distribution for both small and large drop emulsion systems.

The stability of both emulsions was assessed by measuring the drop-size distribution over time. Figure 3.10 illustrates the time evolution of the measured drop-size distribution, employing standard percentile readings - d(n,10), d(n,50), and d(n,90). The n in the expression indicates that the percentiles refer to a number-based distribution. The results show that both systems remained stable for 15 days.

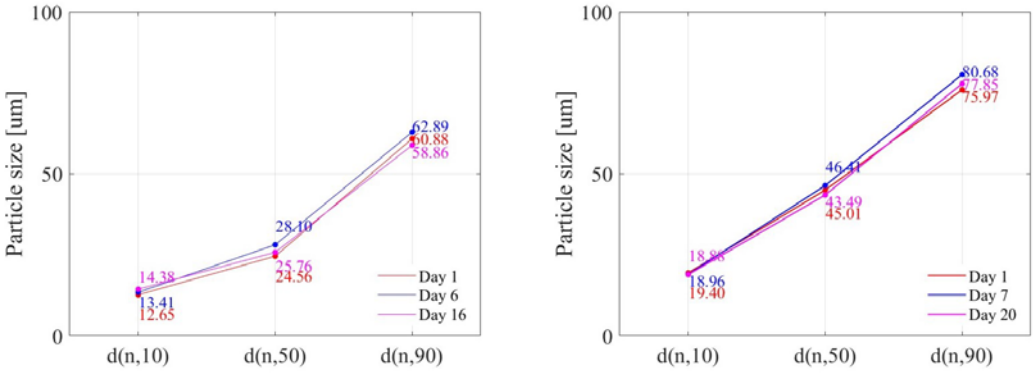

(a) Small drop emulsion. (b) Large drop emulsion.

Figure 3.10: Time evolution of the drop-size distribution in both emulsion systems.

3.4 Experimental Procedure

The efficiency of O/W emulsions as pore-blocking agents was evaluated through water-phase mobility tests and oil displacement tests using two-dimensional porous media micromodels. The water-phase mobility tests investigated the pressure difference behavior of the flow before and after

emulsion injection. The oil displacement experiments evaluated the additional volume of oil recovered after emulsion injection. Images of the flow and pressure data were recorded throughout the tests. The experiments were conducted at various flow rates to cover a wide range of capillary numbers. A schematic representation of the experimental setup utilized for the tests is illustrated in Figure 3.11. Following is an overview of the individual components comprising the experimental setup.

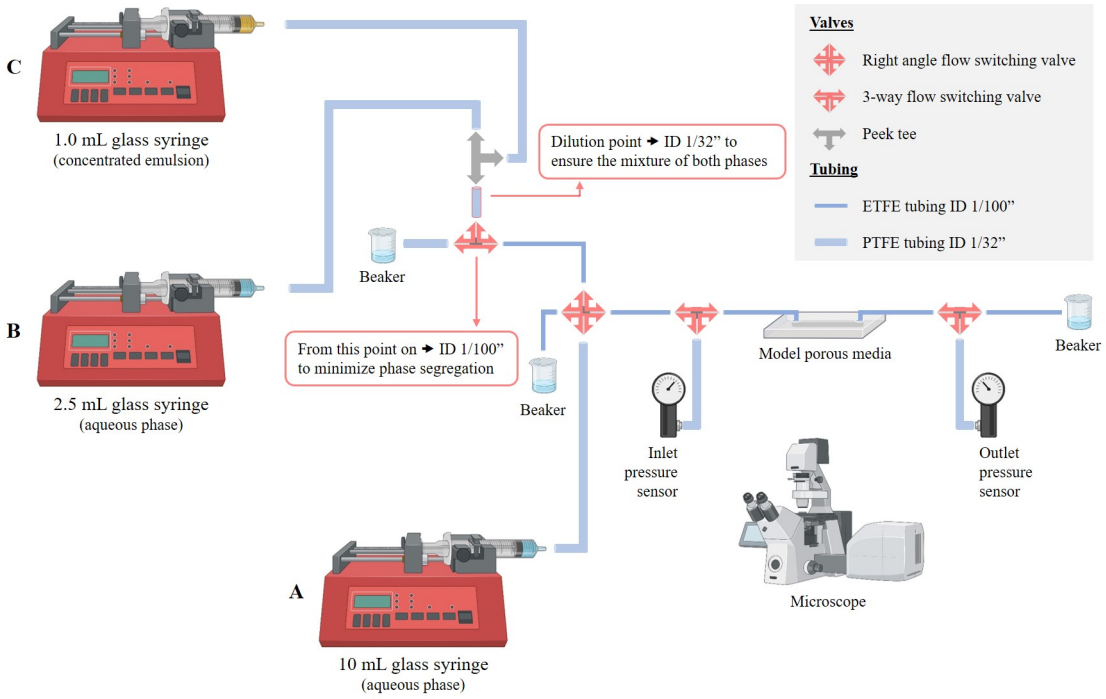

Figure 3.11: Schematic representation of the experimental setup employed for the flow tests. The experimental apparatus is not shown to scale.

1. Injection system

The injection system comprised a sub-system termed the Emulsion Injection Module, illustrated in Figure 3.12. This module consisted of two syringe pumps (Syringe Pump 11 Elite, Harvard Apparatus) coupled to glass syringes (1000 Series GASTIGHT, Hamilton Syringe), each one containing the concentrated emulsion (1.0 mL) and the aqueous phase (2.5 mL), separately. The fluid lines were connected to a PEEK-tee, where the phases converged to dilute the concentrated system in the aqueous phase. By a simple mass balance, the flow rate of each syringe pump was set such that the dispersed phase concentration of the injected emulsion was 5%. The outlet of the PEEK-tee was coupled to a right-angle valve by a 1/32" ID tubing to ensure both phases were properly mixed. Downstream the right-angle valve, a PEEK tubing

(1/100" ID) was used to minimize the gravitational segregation of the phases in the injection line.

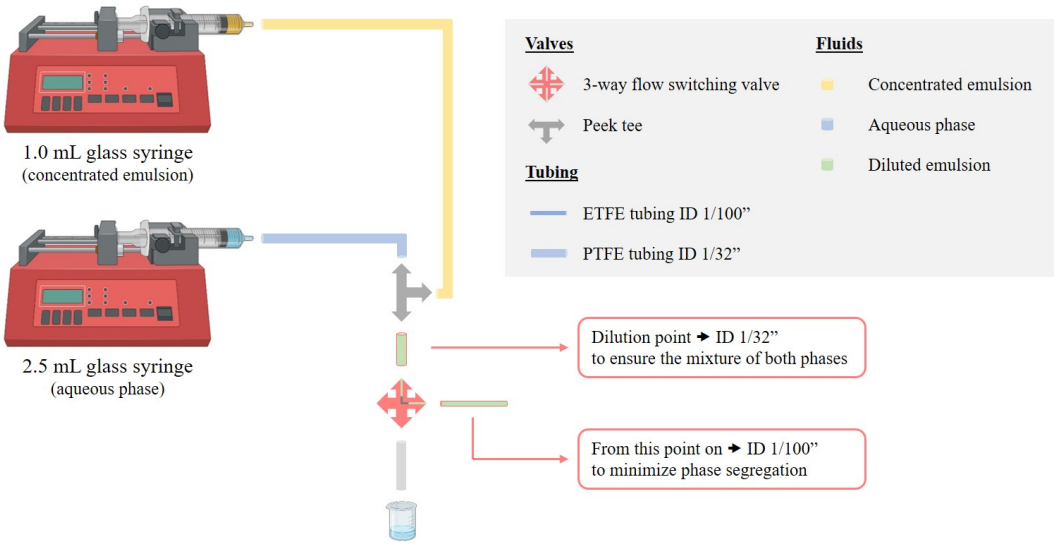

Figure 3.12: Emulsion Injection Module.

The Emulsion Injection Module was integrated with both the micromodel and an additional syringe pump, enabled by a right-angle valve. Pressure sensors were connected to the boundaries of the porous medium, while the flow lines were attached to the inlet and outlet ports of the micromodel. The complete system is illustrated in Figure 3.11.

2. Pressure measurement

Low-pressure sensors were connected to the inlet and outlet ports of the micromodel and the data acquisition (DAQ) module (C Series Current Input Module NI 9203, National Instrument). The module was paired with Labview® for data collection. The sampling rate was set to 1000 Hz, corresponding to a sample interval of 1 millisecond.

A calibration procedure was established to fine-tune the accuracy of the pressure sensors within their operational range. This process involved integrating the sensor with a calibrated pressure gauge (DPG 4000, Omega), a syringe pump, and the current input module for data acquisition. Figure 3.13 illustrates the experimental setup. Calibration points spanning the sensor's measurement range were selected. The process started by ensuring the sensor registered zero pressure at its lower limit of 4 milliamperes (mA) when no external pressure was applied. Pressure was then systematically increased to successive calibration points within the designated range. At each point, a

known pressure was applied using the syringe pump, cross-checked with the pressure gauge, and recorded by the current input module. The module captured and recorded pressure readings in milliamperes corresponding to each applied pressure point. This process was repeated for ten points to ensure thorough coverage across the calibration range. Following data acquisition, the accuracy of the pressure sensor was evaluated by plotting the applied pressures (psi) against the measured values (mA) and verifying its linear response. The calibration curve was generated by fitting the data points to a linear model.

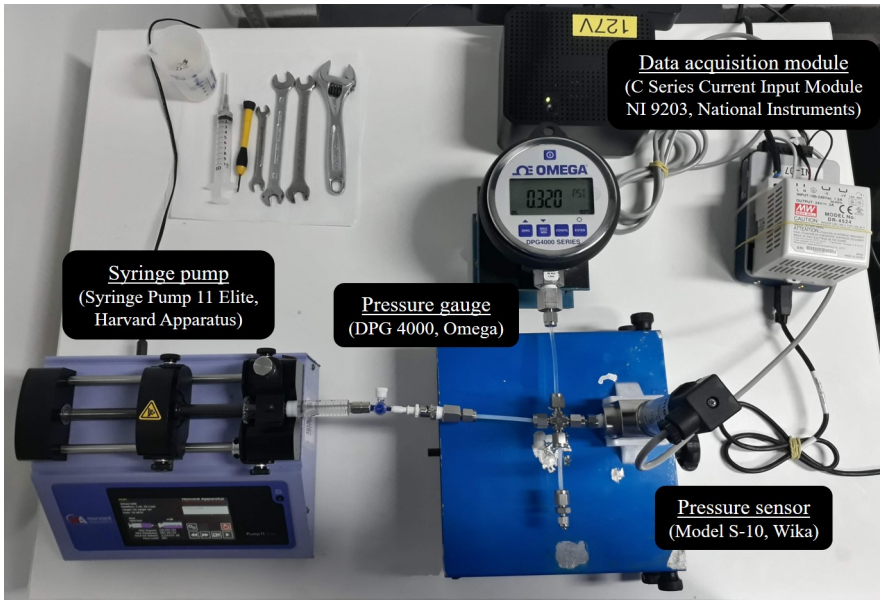

Figure 3.13: Setup for the calibration procedure.

3. Porous media micromodel

The model porous medium has inlet and outlet ports for the injection and production of fluids, respectively. The micromodel was connected to both the injection system and the pressure sensors by 3-way valves and 1/32" ID tubing. A complete description of the micromodel is provided in Section 3.2.

4. Flow visualization system

Leica DMi8 Inverted Microscope (Leica Microsystems), Nikon SMZ 745T Stereo Microscope (Nikon Instruments), and Leica TCS SP8 Confocal Microscope (Leica Microsystems) were employed to visualize the flow tests. Each microscope served to evaluate distinct aspects of emulsion flooding. Throughout the tests, the micromodel was positioned on a motorized stage, and images were captured using a high-speed camera connected to the micro-

scope. Micrographs were recorded at various stages of the test to scrutinize the characteristics of emulsion flooding and the mechanisms for capturing drops.

3.4.1 Linear Flow

The linear flow tests assessed the reduction in aqueous phase mobility resulting from the presence of emulsion drops within the porous medium. Throughout the tests, the pressure drop across the porous medium was recorded, and images were captured to visualize drop retention.

Injection conditions were determined using the dimensionless capillary number, Ca, defined in terms of the aqueous phase viscosity, μ_w, Darcy velocity, ν, and interfacial tension, σ, between the aqueous and oleic phases.

$$Ca = \frac{\mu_w \nu}{\sigma} \tag{3-3}$$

The tests were conducted at different flow rates to cover capillary numbers ranging from 2×10^{-5} to 6×10^{-4}. Table 3.5 presents the total injection flow rates, their corresponding capillary numbers, and the injection flow rates set for each pump across all examined cases.

Table 3.5: Flow rates used to conduct the water-phase mobility tests.

Darcy velocity	**Flow rate**			**Capillary number**
[$\mathrm{mms^{-1}}$]	**Total**	**Concentrated emulsion**	**Aqueous phase**	[ ]
	[$\mathrm{mLh^{-1}}$]	[$\mu\mathrm{Lmin^{-1}}$]	[$\mu\mathrm{Lmin^{-1}}$]	
0.070	0.301	0.345	4.682	2.05×10^{-5}
0.204	0.881	1.010	13.688	5.99×10^{-5}
0.382	1.649	1.890	25.627	1.12×10^{-4}
0.750	3.242	3.717	50.393	2.20×10^{-4}
1.052	4.546	5.212	70.665	3.09×10^{-4}
1.476	6.375	7.308	99.093	4.33×10^{-4}
2.069	8.939	10.248	138.956	6.08×10^{-4}

The experimental procedure of the linear flow tests adopted the setup described at the beginning of this section and depicted in Figure 3.11. Additionally, an image of the experimental setup captured during the test is shown in Figure 3.14.

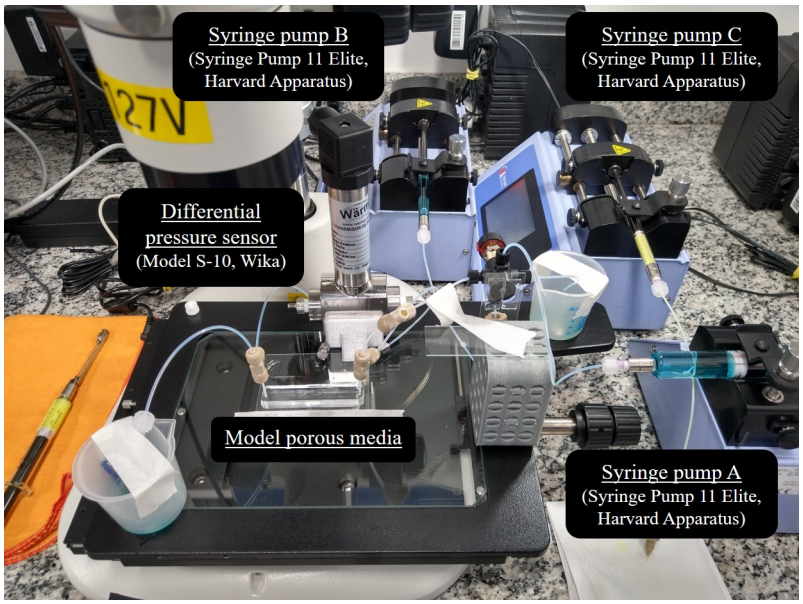

Figure 3.14: Image taken from the experimental setup during the linear flow tests.

The test involved saturating the porous medium completely with the continuous phase before initiating emulsion injection. Initially, the micromodel was positioned under the microscope, and the aqueous phase was injected using a 10-mL glass syringe connected to syringe pump A. Once the pressure lines and the porous medium were fully saturated, the injection was sustained for an additional 4 pore volumes. Throughout this step, the right-angle valve was adjusted to direct the flow of the aqueous phase to the micromodel.

Concurrently, syringe pumps B and C from the Emulsion Injection Module, operating at the flow rates specified for each fluid phase (see Table 3.5), directed the flow from the syringe pumps to the PEEK-tee, where the phases converged to dilute the concentrated emulsion in the aqueous phase. Downstream of the PEEK-tee, the 3-way valve directed the flow of the diluted emulsion to a beaker until the end of the aqueous phase injection.

Upon completing this step, the 3-way valve and subsequent valves were adjusted to direct the flow of the diluted emulsion to the micromodel. Once a steady-state regime was achieved, the injection of emulsion ceased, and the 3-way valve was rerouted back to the beaker. Simultaneously, the right-angle valve directed the flow of the aqueous phase from the syringe pump A back to the micromodel for an additional 15 pore volumes. This setup effectively separated the flow of the aqueous phase and the emulsion, thereby preventing any alteration of the composition of each fluid phase.

3.4.2
Radial Flow

The radial flow tests included both the water-phase mobility tests and the oil displacement test. The latter evaluated the additional oil recovered after emulsion injection. The pressure drop was acquired during all steps of the test. Images were taken to analyze the distribution of each phase within the porous medium and quantify the saturation of oil recovered before and after emulsion injection.

The mobility flow tests were conducted according to the procedure outlined in Section 3.4.1. An additional step was incorporated to account for the two-phase nature of the flow. Differently from the mobility flow tests, the micromodel was initially saturated with the oleic phase before the aqueous phase injection. The aqueous phase (without oil drops) was injected until no changes in saturation or pressure variations were observed, reaching a steady-state condition. Subsequently, emulsion injection was initiated as described in the mobility tests and was sustained for 1 pore volume. Upon completing this step, the injection of aqueous phase was resumed for approximately 30 pore volumes.

In radial flows, velocity decreases radially from the central injection point due to the principle of mass conservation. To account for different injection conditions, the capillary number was defined at the inlet of the porous medium. The flow conditions of the experiments are summarized in Table 3.6.

Table 3.6: Flow rates used to conduct the water-phase mobility tests and the oil displacement test.

Darcy velocity	**Flow rate**			**Capillary number**
[mms^{-1}]	**Total**	**Concentrated emulsion**	**Aqueous phase**	[ ]
	[mLh^{-1}]	[$\mu Lmin^{-1}$]	[$\mu Lmin^{-1}$]	
2.036	3.685	4.298	57.209	5.98×10^{-4}
11.147	20.171	23.524	313.147	3.27×10^{-3}
1.054	1.907	2.262	29.570	1.15×10^{-4}

3.5
Image Acquisition and Processing

3.5.1 Image Acquisition using CLSM

The Leica TCS SP8 microscope was utilized for quantifying the intensities and investigating the spatial arrangement of fluorescent dyes within each phase. The microscope scan head is outfitted with four lasers, two photomultiplier tubes (PMTs) dedicated to both reflected and fluorescent light, one PMT for transmitted light, and a hybrid (HyD) detector. The lasers provide excitation at four distinct wavelengths: 405, 488, 552, and 638 nm.

Fluorophores were selected to distinguish each phase, with careful consideration to minimizing wavelength overlapping issues. However, in multi-channel acquisition, cross-talk can often occur when samples are labeled with multiple fluorescent dyes, resulting in interference and blending of emissions across the spectral range. To address this challenge, a comprehensive understanding of the emission profiles of the selected fluorophores was necessary. This was particularly important given the unconventional nature of Oil-Glo as a fluorophore. Oil-Glo is primarily employed as a fluorescent dye for detecting leaks of oil-based working fluids. Its composition comprises a blend of perylene dye, naphthalimide dye, and a hydrocarbon-based fluid. Perylene dyes exhibit a vibrant yellow fluorescence when exposed to incident radiation within the UV-A band (315-400 nm). Similarly, naphthalimide dyes emit a striking green fluorescence under incident radiation within the blue/violet visible band (400-480 nm) [82].

Figure 3.15 illustrates the emission spectra acquired for the three fluorophores under different excitation wavelengths.

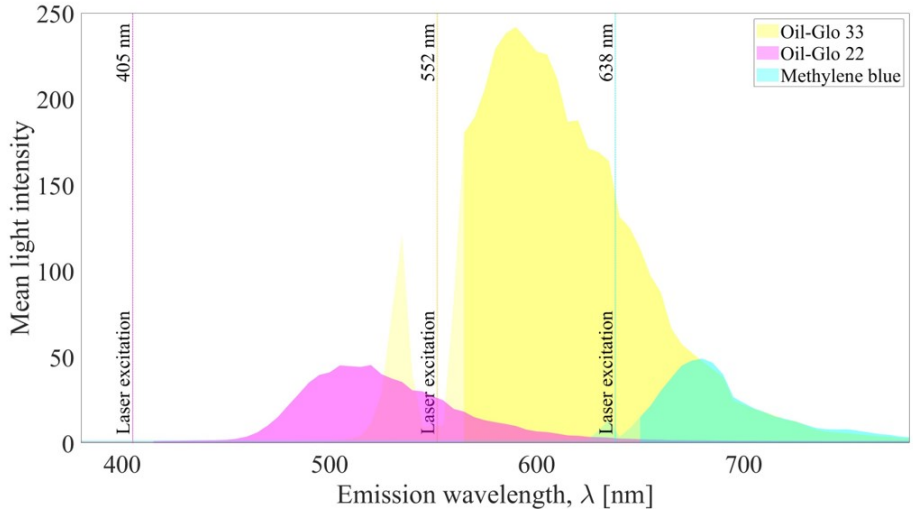

Figure 3.15: Excitation and emission spectra of the fluorophores employed in each fluid phase: Oil-Glo 33, Oil-Glo 22, and methylene blue.

By identifying the distinct emission peaks, it became possible to distinguish between the samples despite their overlapping spectra. The emission spectra were determined through a lambda scan using the Leica Application Suite X (LAS X). Each sample underwent scanning at a defined excitation wavelength, with resulting emissions recorded between 380 nm and 790 nm, utilizing a 5 nm bandwidth.

To further mitigate cross-talk, a narrow detection range was carefully selected for each dye. This selection, as shown in Figure 3.16 and specified in Table 3.7, ensured that emissions from each fluorophore could be accurately separated and analyzed without interference.

Table 3.7: Excitation wavelengths and corresponding detection ranges used for each phase.

Fluid phase	**Excitation wavelength**	**Detection range**
Aqueous	638 nm	695 nm - 710 nm
Oleic	552 nm	595 nm - 610 nm
Dispersed oleic	405 nm	500 nm - 515 nm

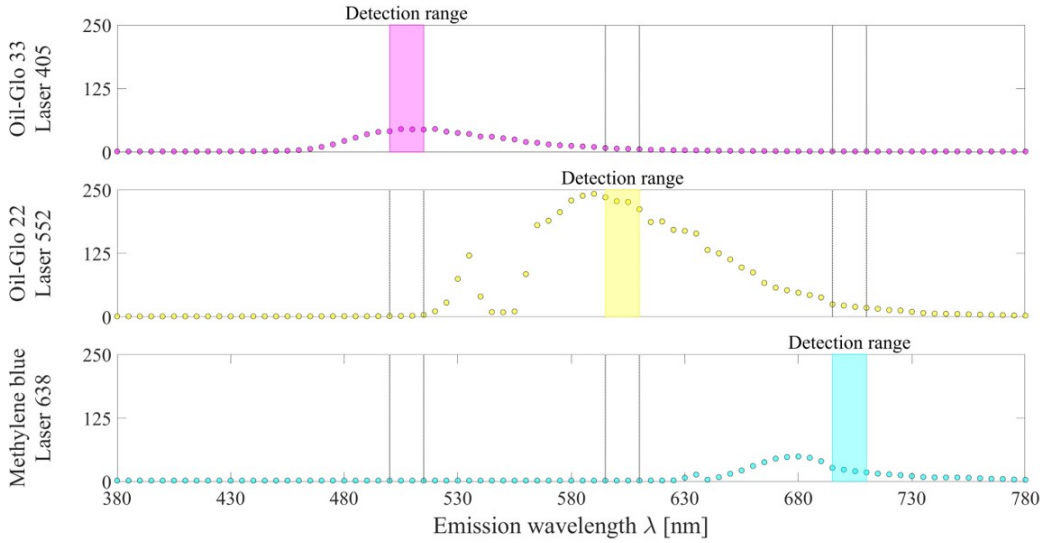

Figure 3.16: Strategy for capturing the fluorescence channels using a fully sequential approach. The dispersed phase is depicted in magenta, the oleic phase in yellow, and the aqueous phase in cyan.

A sequential scanning approach was also employed, where each channel was imaged individually, with only one laser and its corresponding detector activated at a time. Figure 3.17 exemplifies the image acquisition scheme. Each channel was captured separately (Figures 3.17a, 3.17b, and 3.17c) and further combined to depict the complete image (Figure 3.17d). In single-phase flow experiments, imaging was conducted using the oleic phase.

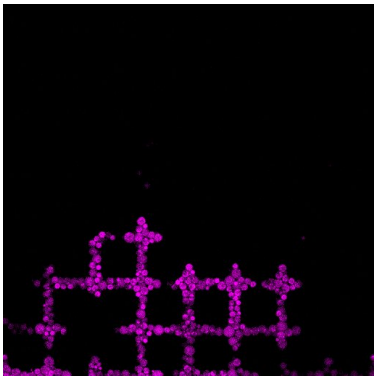

(a) OG33 channel: emulsion oil drops.

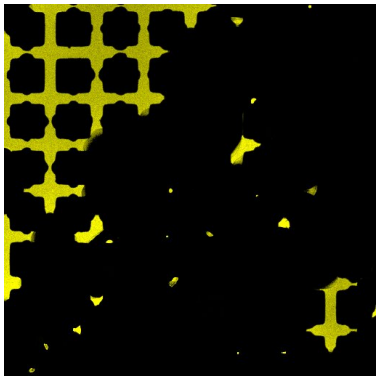

(b) OG22 channel: residual oleic phase.

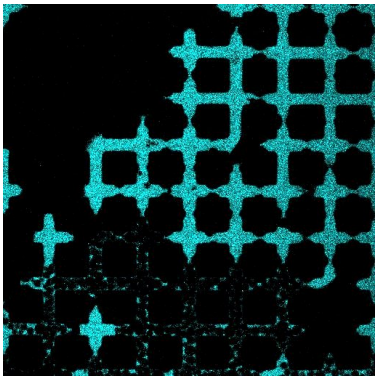

(c) MB^+ channel: injected aqueous phase.

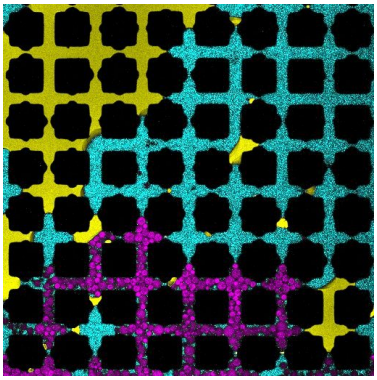

(d) Overlaid image combining all channels.

Figure 3.17: Confocal detection channels. Solid posts are shown in black. Scale bars = 500 μm.

The image of the complete microfluidic device was acquired using the *tilescan* feature of LAS X, as it extends beyond the field of view of the objective lens. This function acquires multiple partial images (xy-planes) of the device and merges them into a single composite image. To merge the images seamlessly, an overlap of pixels is necessary. The intensity of the overlapping pixels was weighted based on their distance from the center of the corresponding image, ensuring smooth transitions between the images. Following the acquisition, a complete image was generated using specialized stitching algorithms.

3.5.2 Image Processing

During the flow tests, images depicting the distribution of each fluid phase before and after emulsion injection were quantified in terms of their saturation. An example of these images is depicted in Figure 3.18.

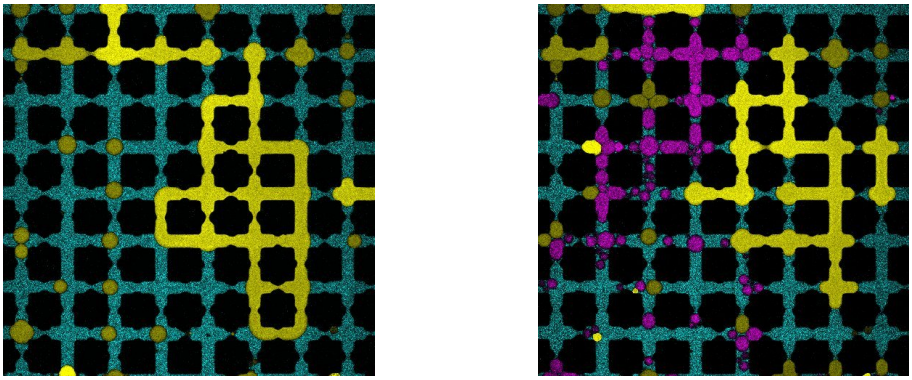

(a) Before emulsion injection (b) After emulsion injection

Figure 3.18: A tile from the same coordinates showing the distribution of fluid phases during waterflooding before and after emulsion injection.

Image processing was performed separately for each channel to facilitate accurate detection and quantification of fluid phases. Single- and two-phase flow tests required different channels during acquisition, resulting in varying numbers of images for subsequent processing. Table 3.8 provides an example of the image processing requirements at different stages of a flow test: after saturating the device with the oil phase (single-phase flow), after the first aqueous phase injection (before emulsion injection), and after the second aqueous phase injection (after emulsion injection).

Table 3.8: Fluid phases and the corresponding number of channels and images in each flow test.

Flow test	**Fluid phase**	**Channels**	**Images**
Single-phase flow	Oleic	1	784
Two-phase flow			
Before emulsion injection	Oleic and aqueous	2	1578
After emulsion injection	Oleic, dispersed oleic, and aqueous	3	2352

To handle the substantial number of images efficiently, a macro was developed in Fiji® to automate both pre- and post-processing stages. Additionally, a dedicated routine was established using MATLAB® to analyze the extensive dataset and calculate the final saturation values for each fluid phase. The complete process is illustrated in Figure 3.19.

Initially, images were exported from LAS X® as individual tiles and organized into folders; frames from each channel corresponding to the same tile were grouped. The macro then systematically accessed each folder, executing

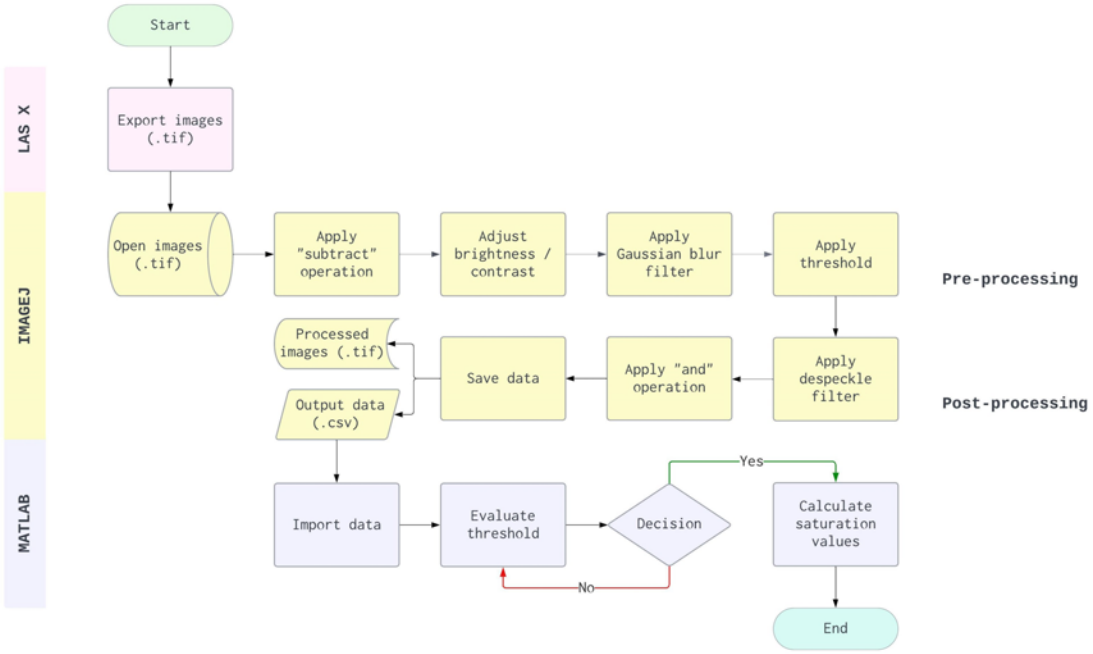

Figure 3.19: Comprehensive flowchart describing the image processing workflow. The red box refers to the activity executed in LAS X® software. The yellow and blue boxes correspond to the steps conducted in Fiji® and MATLAB®, respectively.

pre- and post-processing steps (yellow boxes in Figure 3.19) while iterating through the range of tiles from 1 to 784.

The first processing step involved conducting subtraction operations between images to isolate each fluid phase. Next, adjustments to brightness and contrast were made to optimize image features, ensuring neither over nor underexposure occurred. The subsequent step involved applying the Gaussian blur filter to the images, reducing high-frequency noise and enhancing the overall smoothness.

Following these steps, image segmentation was carried out to separate foreground information from background pixels. Binary images were generated based on preset threshold limits, classifying pixels above the threshold as foreground pixels (0) and those below as background pixels (1). Figure 3.20 illustrates the pre-processing steps using an image from the oleic phase channel as an example.

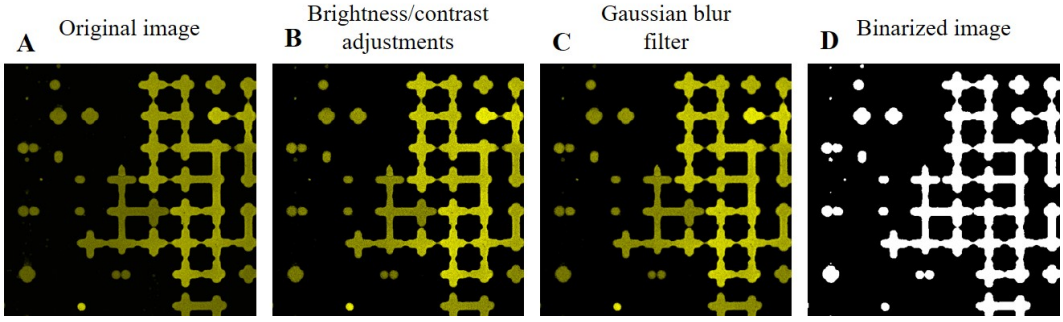

(a) Pre-processing steps: (A) the original image; (B) image after brightness and contrast adjustments; (C) image after application of the Gaussian blur filter; (D) image after thresholding.

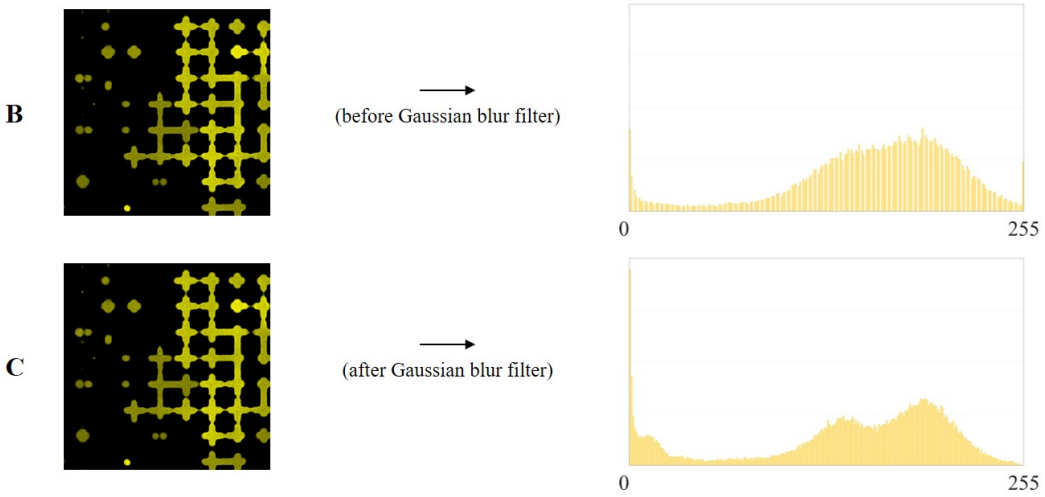

(b) The histogram showing the distribution of pixel intensity values of images B and C. The application of the Gaussian blur filter resulted in a smoother histogram.

Figure 3.20: The pre-processing steps.

The post-processing step consisted of removing foreground objects from the binarized images and computing the mean intensity value of the remaining pixels. To accomplish this, the logical `AND` operation was performed between the original and the binarized images. This step was crucial in testing the efficiency of different threshold methods and will be described in the next section.

At the end of the post-processing stage, the processed data was organized and saved into a `.csv` file, while the resulting images were stored in their original folders. The output data was used to evaluate the threshold methods and calculate the saturation values of each phase. This stage was conducted in MATLAB® and is illustrated by the blue boxes in Figure 3.19.

3.5.2.1 Methodology for processing large number of images

Exploring the performance of different threshold methods is crucial for effective image processing. Figure 3.21 demonstrates the application of three distinct threshold methods to an image of the micromodel's inlet region.

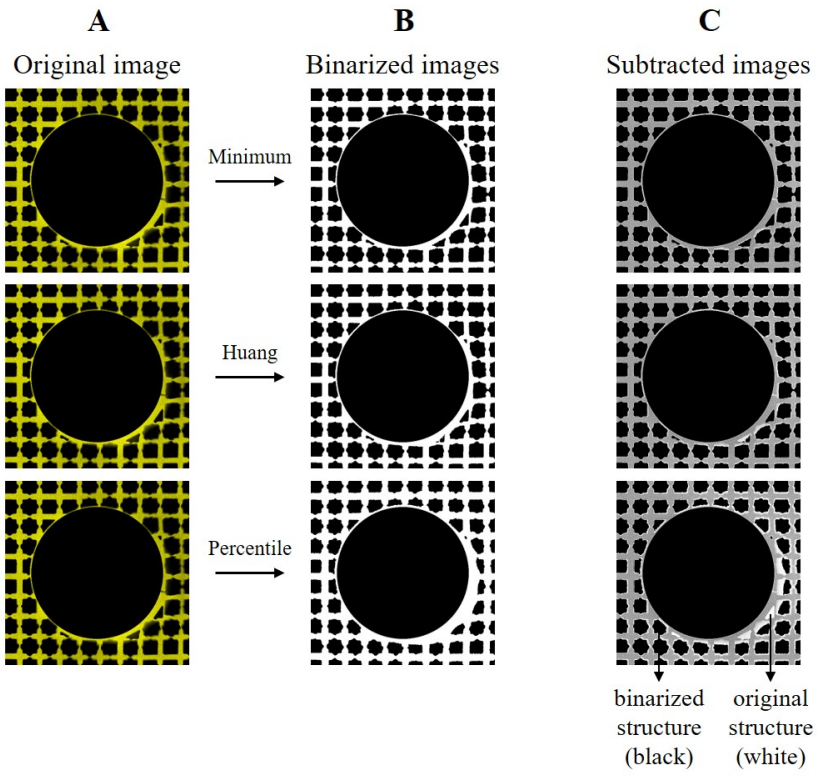

Figure 3.21: Results showing the performance of three distinct threshold methods.

Visual examination of the segmented images provided insights into the segmentation quality achieved by each method. The original image (A) shows the inlet hole and pore structures depicted in black, with the void space in yellow. The binarized images (B) exhibit the original image after segmentation using each threshold algorithm. The subtracted images (C) reveal the binarized images after subtracting the pixels from the original image. Here, the pore structures are delineated in black, the void space appears gray, and the original structures not selected by the threshold are presented in white. The presence of white objects in the subtracted images (C) suggests inaccuracies in the thresholding step. Complementing the visual analysis, porosity values summarized in Table 3.9 were computed to facilitate comparison across each case.

To address this issue, a methodology was developed to evaluate the effectiveness of four global threshold methods available in Fiji®: Huang [83], Li

Table 3.9: Porosity calculation using each threshold method.

Method	**Pore bodies** [μm^2]	**Pore void** [μm^2]	**Porosity** [%]
Minimum	2.41×10^6	1.90×10^6	44.1
Huang	2.28×10^6	2.04×10^6	47.2
Percentile	1.83×10^6	2.49×10^6	57.7

[84, 85], Otsu [86], and Renyi Entropy [87], each employing distinct criteria to determine the threshold values.

This methodology involved removing foreground objects from binarized images and calculating the mean intensity values of the remaining pixels. This procedure is schematically illustrated in Figure 3.22.

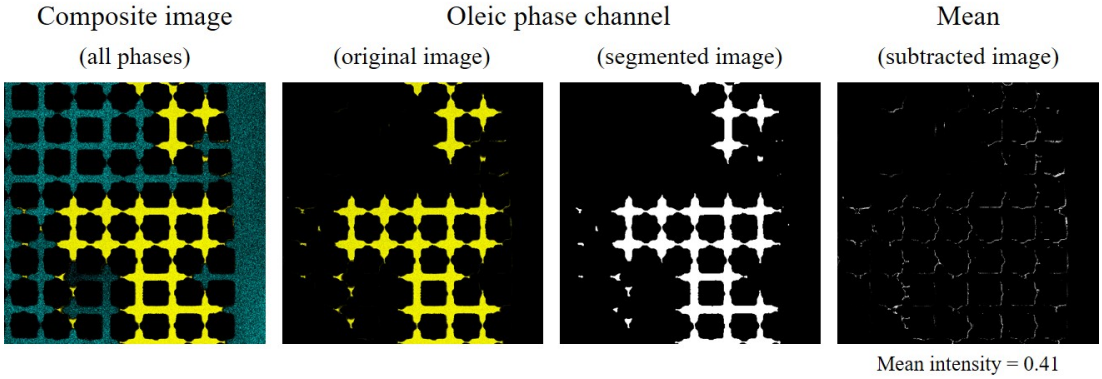

Figure 3.22: A visual overview of the methodology developed to evaluate the effectiveness of distinct threshold methods.

The mean intensity values were computed and plotted for each threshold method, normalized relative to the maximum intensity of an 8-bit image (255). Figure 3.23 displays data (in yellow) predominantly ranging from 0 to 0.01, as most values fall within 1% of the maximum intensity. The plotted data reveals varying degrees of variability across the methods, emphasizing the critical importance of statistical analysis.

The intensity values were also presented using box plots (Figure 3.23), which facilitate data analysis and interpretation by visually summarizing the spread and skewness of large datasets. Box plots provide a clear representation of central tendency through the median (M) and variability through the interquartile range (IQR). They were particularly useful in comparing the distributions of each thresholding method tested in this work. Figure 3.24 presents the summarized data.

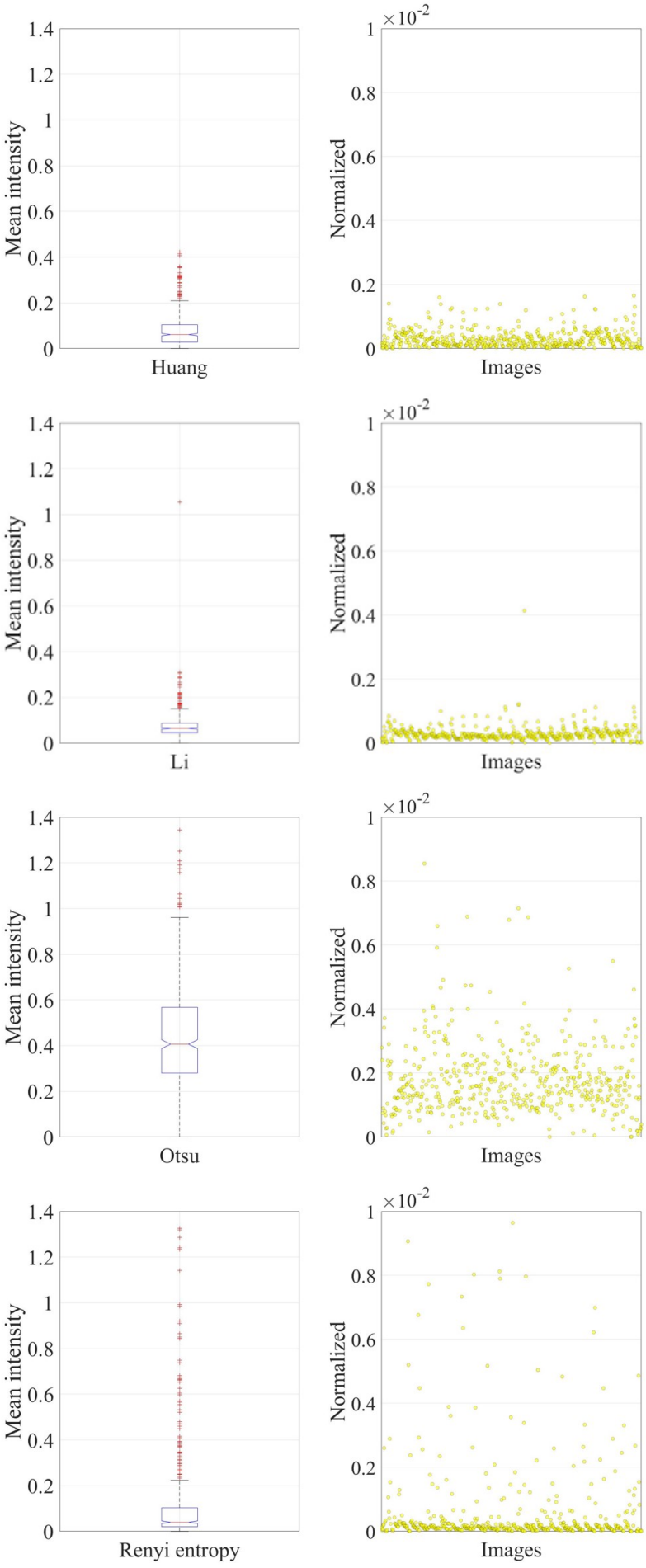

Figure 3.23: Mean intensity values using different threshold methods.

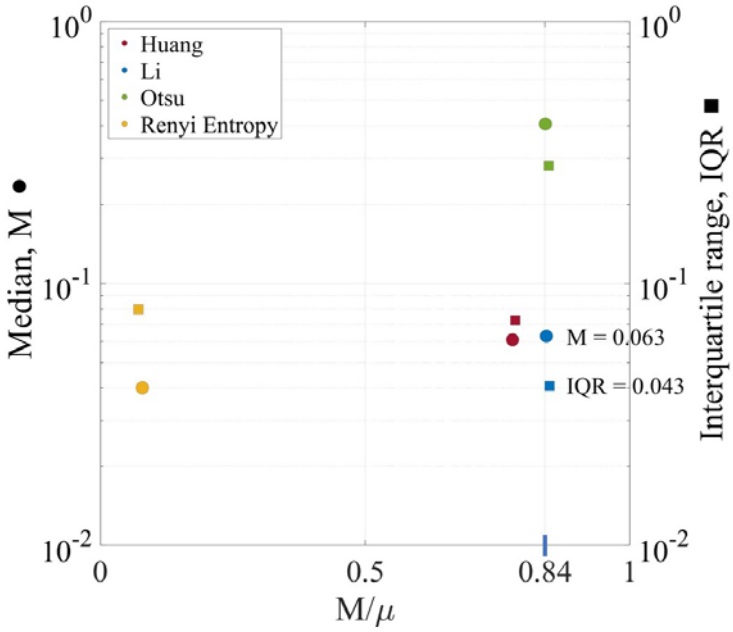

Figure 3.24: A graphical summary illustrating the distribution of mean intensity values. Each color corresponds to a specific thresholding method as indicated in the legend. Circled markers denote the median, while squared markers represent the IQR.

The median proved to be the most critical parameter, followed by the interquartile range (IQR). The ratio between the median and the mean (M/μ) provides an understanding of the symmetry of the distribution. A median closer to the mean ($M \approx \mu$) suggests a symmetric distribution with minimal skewness due to outliers. Additionally, the median reflects the average intensity value of the dataset. The method yielding the lowest median is preferred, as it suggests a higher effectiveness of the thresholding process. The IQR represents the spread between the first and third quartiles, with a smaller IQR indicating decreased variability within the central 50% of the data.

In this case study, the Li method (marked in blue in Figure 3.24) demonstrated the most accurate segmentation. The median approached the mean ($M/\mu = 0.84$), indicating a likely symmetric distribution. Specifically, the median value for the Li method ($M = 0.063$) closely matched that of the Huang method ($M = 0.061$). However, upon analyzing the IQR, it was evident that the data from the Li method exhibited less variability ($IQR = 0.043$).

This systematic approach provided a reliable methodology for evaluating different threshold algorithms by analyzing the mean intensity values of remaining pixels in subtracted images. It proved particularly useful for processing a large number of images using an automated macro.

4
Emulsion Injection in Linear Flow

This chapter presents the findings from the linear flow of stable O/W emulsions in model porous media. It begins with a detailed characterization of the device, describing its structural properties and surface characteristics. Next, the results of the water-phase mobility tests are discussed, providing insights into the dynamic behavior of trapping and subsequent mobilization of emulsion drops within the pore structure across a range of capillary numbers.

4.1
Pore Network Characterization

The linear geometry comprises a rectangular porous medium with a footprint of 60 × 12 mm^2, as illustrated in Figure 4.1 (A). A distribution chamber (B) was provided at each end of the porous medium to ensure uniform fluid dispersion across the inlet and outlet of the device, maintaining uniform pressure. Inlet and outlet ports (C) facilitate the connection of the flow lines to the micromodel.

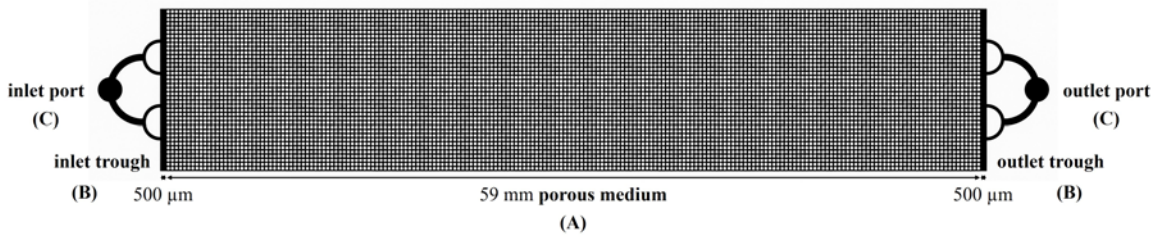

Figure 4.1: Linear porous media device.

The measured values for three micromodels are presented in Table 4.1, showing slight deviations from the original design associated with the micro-fabrication process.

The pore network was constructed by arranging the unit cells in the x and y directions, as shown in Figure 4.2. A total of 20 × 4 unit cells were assembled, creating a network of approximately 6,500 posts. Each unit cell consists of randomly placed channels of varying sizes within a square lattice, as detailed in Section 3.2.1.

Table 4.1: Geometric dimensions of the linear micromodel.

#	Length [mm]	Width [mm]	I/O trough [μm]		Porosity [%]
1	57.80	11.53	447.31	467.74	55.3
2	58.48	11.66	438.22	365.57	52.7
3	58.48	11.69	492.72	483.64	55.7

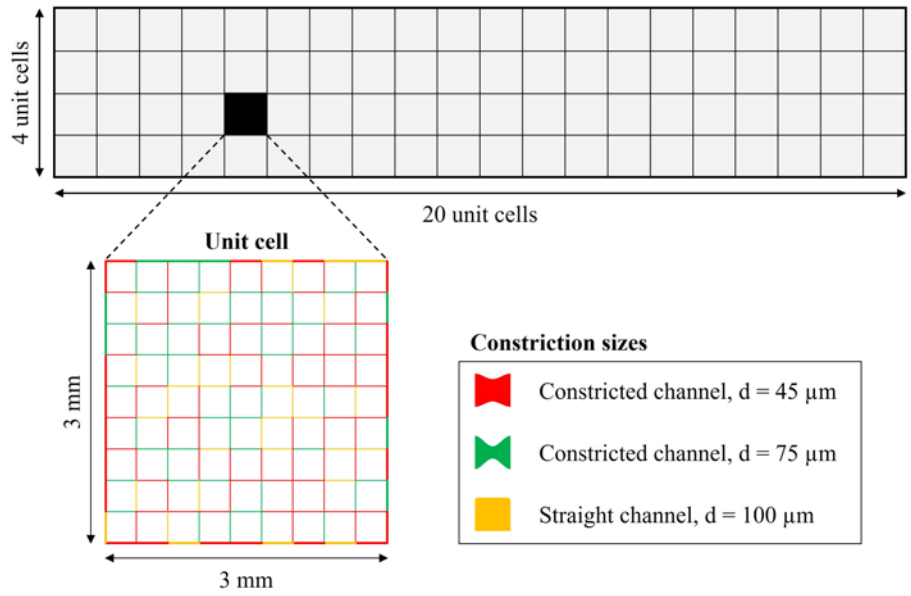

Figure 4.2: A schematic illustration of the pore network arrangement, comprising 20 × 4 unit cells, each containing randomly placed straight and constricted channels.

In such configurations, the posts align with the pressure gradient, facilitating fluid flow from the inlet to the outlet of the micromodel. The random distribution of constrictions introduces additional variability to the flow.

4.1.1 Channel Size Distribution and Average Height

Figure 4.3 presents the frequency distribution of the measured constriction sizes, which falls into three groups as expected from the original design: 45-μm constrictions, 75-μm constriction, and 100-μm straight channels. The black curve represents the multimodal distribution derived from the measured data, with modal sizes of 54 μm, 82 μm, and 104 μm for each group, respectively. The deviations from the original design arise from inaccuracies during the microfabrication process.

The average height of the channels is 99.65 μm. Local heights were computed from 500 tiles and analyzed across 95 stacks (refer to Section 3.2.2.1 for the detailed procedure). Figure 4.4 illustrates the image acquisition map.

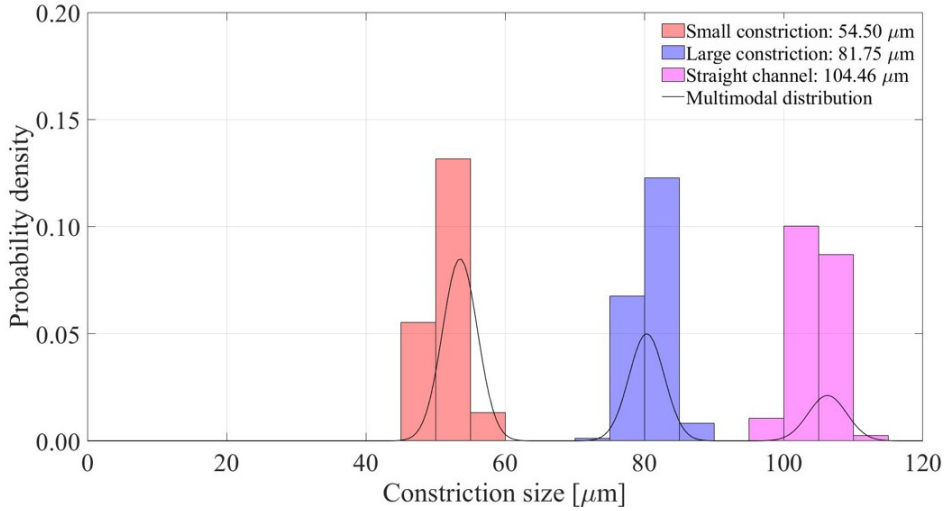

Figure 4.3: Constriction size distribution showing modal sizes of 54 μm, 82 μm, and 104 μm.

Images were acquired using a 10× (0.40 NA, HC PL APO CS) dry lens, with a scanning speed of 5×10^{-3} ms/pixel and a resolution of 512 × 512 pixels. Each tile measured 1.24 × 1.24 mm^2, corresponding to a 4-by-4-pore structure tile.

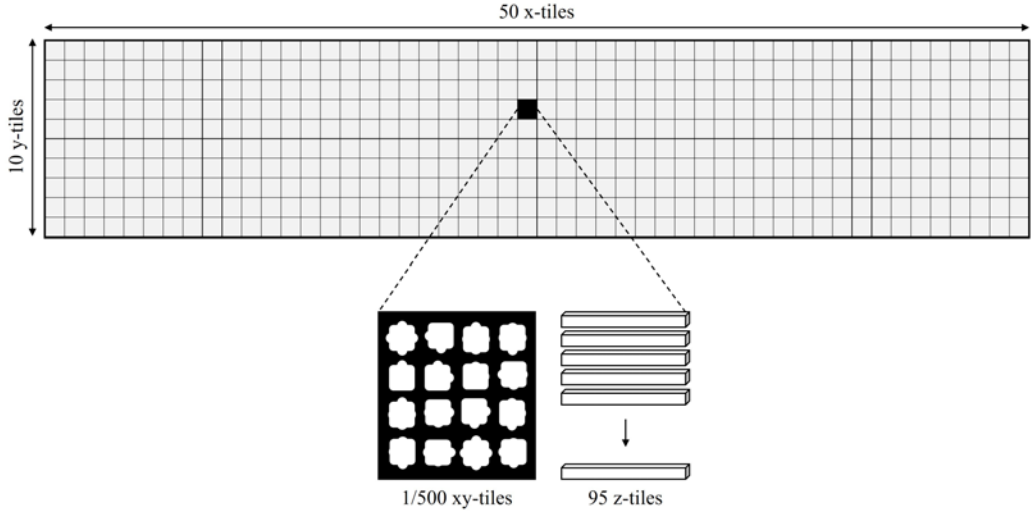

Figure 4.4: A total of 500 tiles, each containing 95 stacks, were analyzed to compute the local heights of the channels.

4.1.2 Porosity and Pore Volume

Porosity (refer to Section 3.2.2.3) was evaluated across three devices sourced from the same master mold and submitted to identical microfabrication procedures. The resulting values are presented in Table 4.1, revealing a porosity

of 0.546 ± 0.016. The pore volume was calculated by multiplying the porous area by the average height, resulting in 37.42 ± 1.15 μL.

4.1.3 Absolute permeability

The absolute permeability was determined using Darcy's law, calculated from the slope of the pressure difference versus flow rate curve, as shown in Figure 4.5. Tests A and B were conducted at flow rates ranging from 0.1 to 1.0 cch^{-}1 and 1.0 to 20.0 cch^{-1}, respectively. Both results yielded approximately 100 D and are consistent with the value reported by Escalante [14].

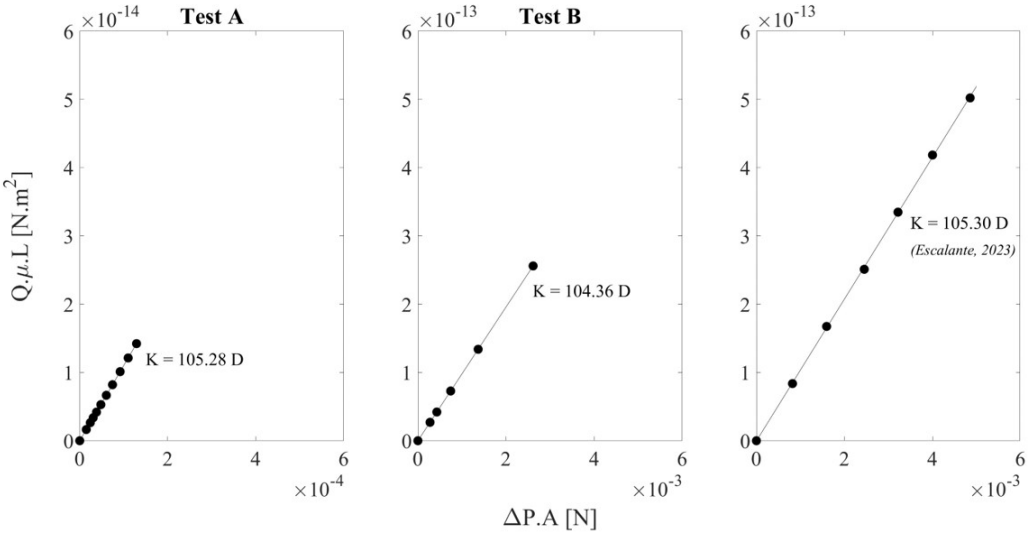

Figure 4.5: Absolute permeability of the porous medium determined using Darcy's law. The first plot (Test A) was conducted at low flow rates, ranging from 0.1 to 1.0 cch^{-1}. The second plot (Test B) was conducted at higher flow rates, ranging from 1.0 to 20.0 cch^{-1}. The third plot presents the result reported by Escalante [14].

The setup used to determine the absolute permeability is shown in Figure 4.6. The pressure drop was measured directly from the porous medium, with the pressure ports positioned at the boundaries of the pore network to exclude additional pressure drop from the fluid flow lines and the inlet and outlet channels.

Although the absolute permeability was higher than those typically found in reservoir rocks, the transparent geometry enabled the visualization of pore-scale events and their impact on macroscopic flow behavior.

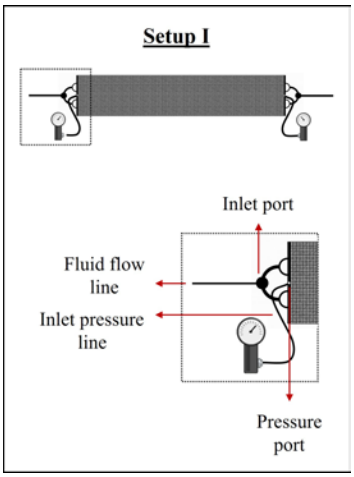

Figure 4.6: Absolute permeability experimental setup. The pressure drop is determined directly from the porous medium. Both pressure and fluid flow lines are connected to the micromodel independently. The pressure ports are positioned at the boundaries of the pore network, excluding additional pressure drop from the inlet and outlet channels and tubing.

4.1.4 Surface wettability

Contact angle measurements were conducted to evaluate the wettability of PDMS and glass surfaces before and after plasma treatment. To ensure thorough dewetting of the dispersed phase from the channel walls, it was essential that all surfaces exhibited similar hydrophilic properties. Measurements were carried out under dry conditions at 21 °C.

PDMS is inherently hydrophobic, as indicated by the contact angle greater than 90° shown in Figure 4.7. After plasma treatment, the contact angle decreased from 100.17° ± 0.25 to 49.55° ± 0.89, temporarily rendering the surface hydrophilic [79].

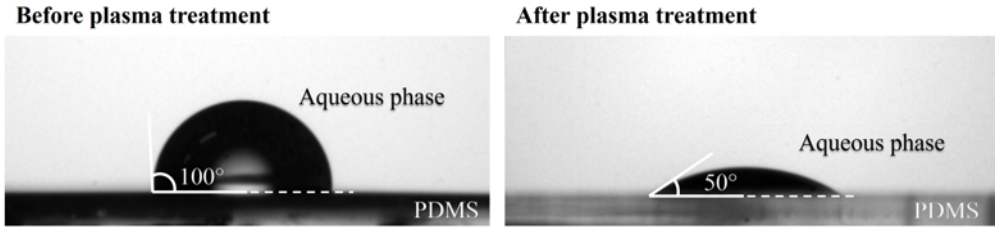

Figure 4.7: Contact angle measurement of a drop of the aqueous phase on the surface of PDMS.

Figure 4.8 illustrates the contact angle between the aqueous phase and the glass slide. Plasma treatment improved the spreading of the aqueous phase on the glass surface, reducing the contact angle from 57.91° ± 1.50 to less than 20°.

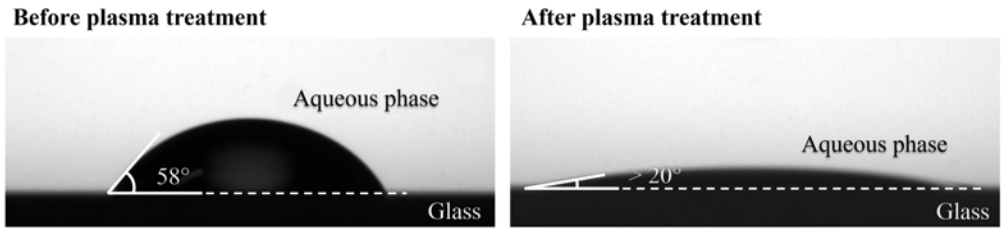

Figure 4.8: Contact angle measurement of a drop of the aqueous phase on the surface of a glass slide.

Micromodels were used immediately after plasma treatment to ensure the surfaces remained hydrophilic during the flow tests.

4.2 Water-Phase Mobility Tests

Fluid flow through porous media is typically modeled using Darcy's law. However, this mean-field description neglects important small-scale events. In emulsion flow, the transport of the dispersed phase significantly changes the continuum flow by altering the dynamics at the pore level. Drops can block the pores and force the surrounding fluid to flow around them, increasing the fluid velocity and changing the velocity components along and transverse to the imposed flow direction [15].

In emulsion flow, drops smaller than the pore throats ($D/d < 1$), move smoothly through the medium without deformation, causing minimal resistance to flow. In contrast, drops larger than the pore throats ($D/w \geqslant 1$) require additional pressure to overcome the capillary resistance and squeeze through the constrictions. If the pressure difference is not strong enough, drops are retained at the entrance of the pore throats. Figure 4.9 illustrates these behaviors as drops of different sizes flow through the channels.

The critical pressure difference needed to push a drop through a constriction depends on the drop diameter, constriction size, and interfacial tension, as described by the Young-Laplace equation:

$$\Delta P = \sigma \left(\frac{1}{R_c} - \frac{1}{R_d} \right) \tag{4-1}$$

Here, σ is the interfacial tension between the phases, R_c is the radius of the constriction, and R_d is the radius of the drop.

Figure 4.10 shows a large drop (marked in red) squeezing through a constriction. The critical pressure is reached as the front part of the drop begins to deform (A). Continuous pressure from the surrounding fluid increases the

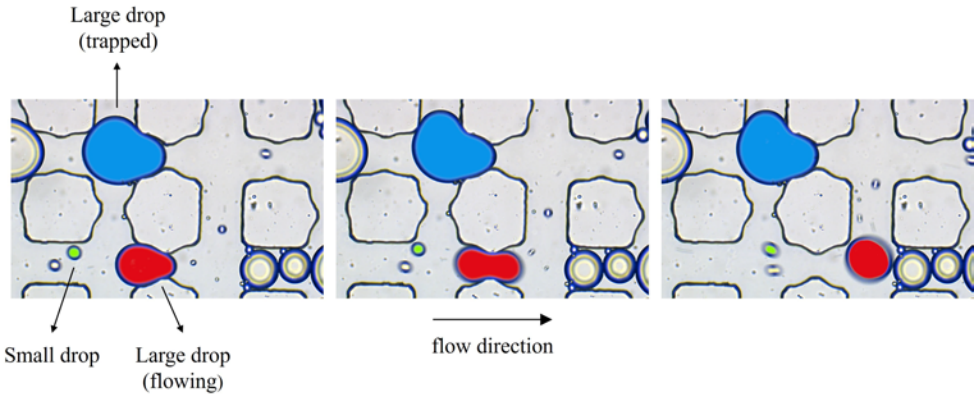

Figure 4.9: Time-sequence of images during emulsion injection showing different drop flow patterns: the small drop (marked in green) flows smoothly through the medium; the large drop (marked in red) deforms as it flows through a constriction; and a larger drop (marked in blue) remains trapped in a pore throat. Images obtained in bright-field mode.

surface area of the drop, stretching it from a spherical to a cylindrical shape. As the front part of the drop moves out of the constriction (B), capillary pressure decreases, reaching its minimum when both ends of the drop are equal in size across the constriction. Beyond this point, the capillary force reverses direction (C), pulling the drop out of the channel and decreasing fluid pressure.

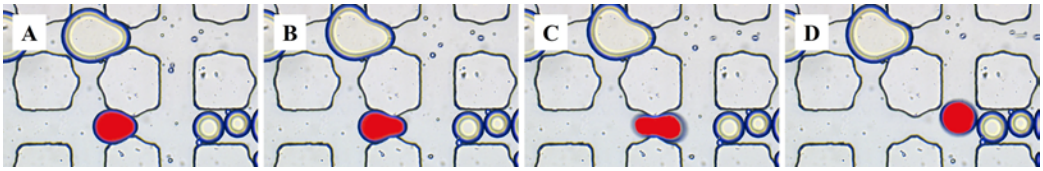

Figure 4.10: Time-sequence of a large drop (marked in red) passing through a constriction: (A) the front of the drop deforms under critical pressure; (B) the tip of the drop begins to move out of the constriction, decreasing the capillary pressure; (C) the capillary force is reversed, pulling the drop out of the channel; (D) the drop fully exits the pore throat. Images obtained in bright-field mode.

Once the drop fully exits the pore throat (D), the rear part may rebound, forming a slightly concave shape due to fluid inertia [64, 88]. The concave deformation is more pronounced at higher velocities, as shown in Figure 4.11 from a similar drop-squeezing event.

In this work, capillary forces are significant, with capillary numbers ranging from 10^{-5} to 10^{-3}. Within this range, interfacial tension drives the deformation of drops. This phenomenon explains why a drop can easily deform to occupy the cross-section of a channel while still retaining a spherical shape after deformation.

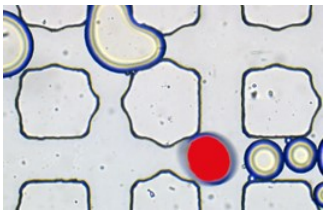

Figure 4.11: Image of a droplet rebounding as it exits a pore throat.

Figure 4.12 depicts a 3D reconstruction near a constriction (marked by the black dashed box), showing multiple drops of varying sizes retained in a pore throat. The drops are distributed across different planes, indicating that the constriction is not fully blocked and allows the surrounding fluid to flow around the drops and through the constriction.

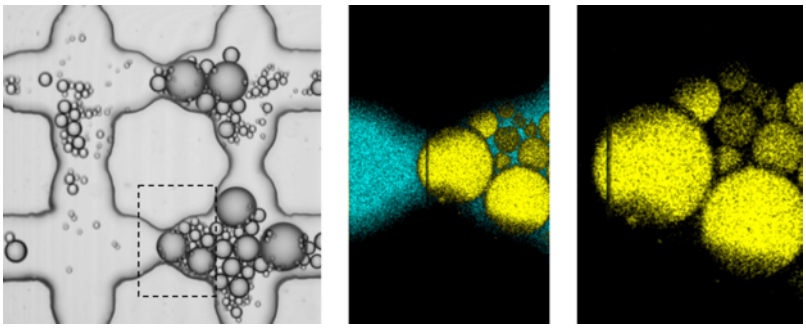

Figure 4.12: 3D reconstruction near a pore throat constriction. Trapped drops are distributed across different planes, revealing that the constriction is not fully blocked and allowing the flow of surrounding fluid around the corners and between the drops. Images obtained using confocal microscopy.

The velocity difference between the continuous phase and the drops contributes to the drag force exerted by the fluid on the drops. The friction force, which opposes the drag force, arises from the contact between the drops and the channel walls and is strongly dependent on drop deformation [89].

Figure 4.13 presents three sequences of images illustrating how drops move through pore constrictions due to local pressure changes. In the first sequence (Figure 4.13a), a large drop (marked in red) reaches the entrance of a constriction, raising the local pressure before quickly squeezing through the narrow passage. A smaller drop (marked in green), flowing closely behind, diverges at the junction, choosing a path with less resistance. Concurrently, the blue-marked drop experiences an increase in pressure and squeezes through an adjacent throat, colliding with another drop at the outlet.

In the following sequence (Figure 4.13b), the large drop exits the pore throat and flows toward the next constriction, where fluid velocity increases due to a narrower gap. This change in velocity creates a pressure difference that pulls the drop through the constriction. This effect is driven by the

incompressibility of the fluid, which pushes the drop through the narrow passage, acting like a piston. However, in rectangular channels, the flow behaves more likely a leaky-piston, where the fluid may either push the drop forward or bypass it through the corners. Here, the pressure forces are dissipated by the motion of the fluid rather than the drop itself, influencing flow distribution and altering the flow topology [89, 90].

In the final sequence (Figure 4.13c), the large drop reaches another pore throat and becomes trapped, causing pressure to build up. Once the pressure surpasses capillary resistance, the drop is squeezed through the pore throat, redirecting the flow to the main stream. This is evident as the smaller drop (marked in green) rejoins the primary path.

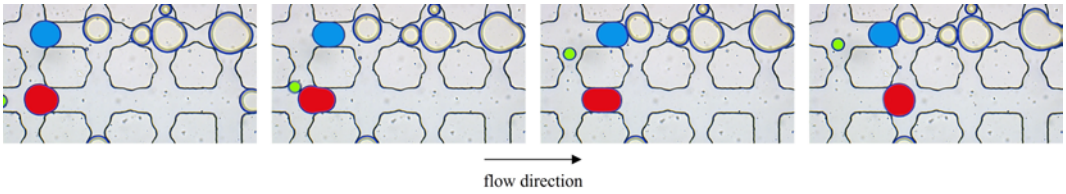

(a) Sequence A: A large drop (marked in red) raises local pressure as it squeezes through a constriction, causing a smaller drop (marked in green) to divert to a path of less resistance. Meanwhile, another drop (marked in blue) squeezes through an adjacent throat and collides with a drop at the outlet.

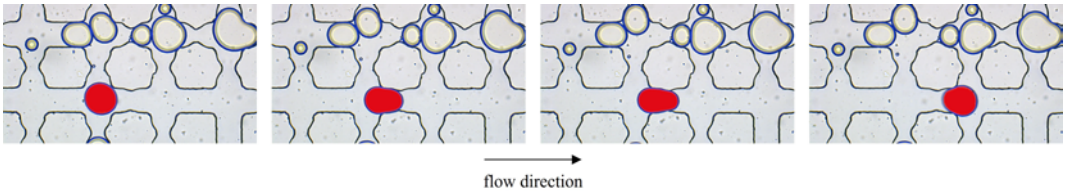

(b) Sequence B: The large drop flows toward the next constriction, where increased fluid velocity and resulting pressure difference drags the drop through the narrow gap.

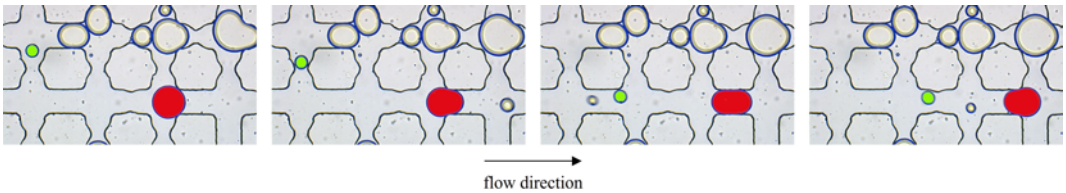

(c) Sequence C: The large drop reaches another pore throat and becomes trapped, leading to a pressure buildup; once the pressure exceeds the capillary resistance, the drop is forced through the throat, redirecting the flow and allowing the smaller drop (marked in green) to rejoin the primary path.

Figure 4.13: The time-sequences illustrate a drop experiencing different mechanisms as it flows through a porous medium. A drop may raise local pressure and divert other drops (Sequence A), be dragged through constrictions due to velocity changes (Sequence B), or become trapped and then forced through a pore throat after a pressure buildup (Sequence C).

In this study, drops flow through straight and constricted channels with

aspect ratios, $AR \equiv h/w$, ranging from 1 to approximately 2 for the smallest constriction. Straight channels with an aspect ratio close to 1 contribute to localized pressure changes, trapping large drops until pressure reaches a critical point and overcomes capillary resistance. The process in Figure 4.13a took about 0.3 seconds to occur. In contrast, the same drop took twice the time (0.6 seconds) to pass through another throat of identical size, as shown in Figure 4.13c. This variation in time reflects local changes in pressure experienced by the drop as it moves along the channel.

When the aspect ratio is greater than 1, drops trapped at pore constrictions experience rapid pressure buildup due to the flow of the continuous phase being forced through small gaps. Figure 4.13b illustrates this phenomenon, showing increased velocity as the drop squeezes through the constriction in a shorter time compared to the other cases (0.1 seconds) [91].

Thus far, we have analyzed the individual mechanisms of drops flowing in confined channels at a low capillary number (2×10^{-5}). As each drop moves through the surrounding fluid, it creates a flow disturbance that can be described as a hydrodynamic dipole, characterized by a pair of equal and opposite flow perturbations [17]. These perturbations, although decaying with distance, still affect other drops. Consequently, even drops far apart experience perturbations in their velocity due to the collective effect of all the dipoles in the system. These long-range dipolar interactions result in collective dynamics among the drops, influencing their trajectories and velocities.

Figure 4.14 illustrates drops changing their trajectories as they navigate through a small region of the pore network. Small drops transverse the channels smoothly, following the pressure gradient and avoiding tortuous paths. In contrast, larger drops alter their paths when encountering obstructions, such as trapped drops or narrower constrictions. The red arrows indicate different paths taken by the drops within a 5-second window. Unlike smaller drops, larger drops percolate through the medium by maneuvering around obstacles, resulting in more tortuous paths. This dynamic process modifies the local flow field and allows previously trapped drops to re-enter the flow stream, intermittently changing the flow paths.

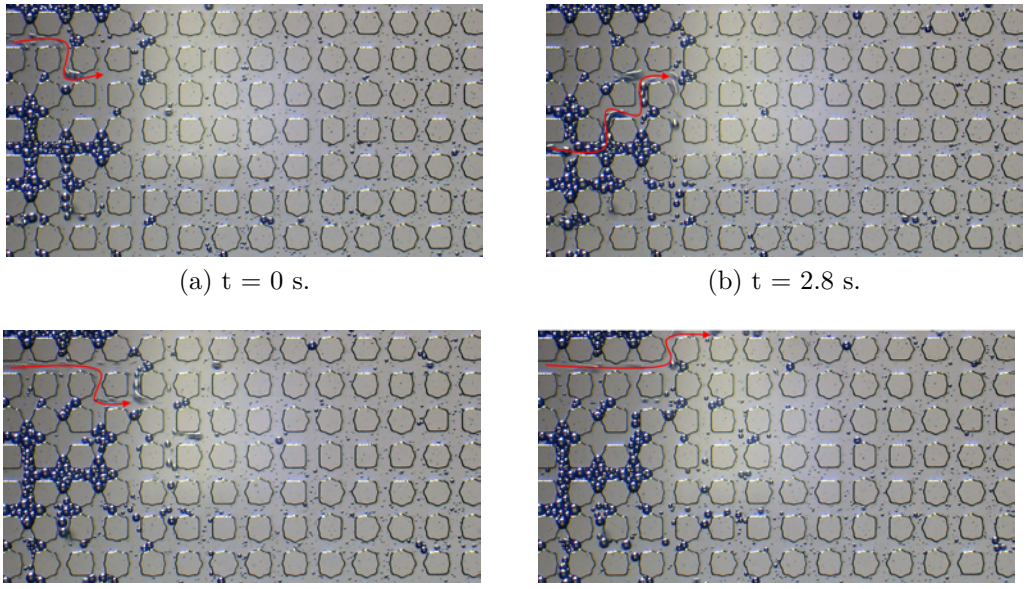

(a) t = 0 s. (b) t = 2.8 s.

(c) t = 4.1 s. (d) t = 5.2 s.

Figure 4.14: Flow paths evolving over a short time-frame. Large drops alter their trajectories when encountering obstacles in the flow. Red arrows indicate varying paths taken by the drops. Images obtained in bright-field mode.

Figure 4.15 illustrates the initial stages of emulsion injection. Upon entering the pore network, drops may either become trapped in narrow constrictions or move independently along straight paths, depending on their size relative to the constrictions. These straight paths represent the shortest route between the inlet and the outlet of the micromodel.

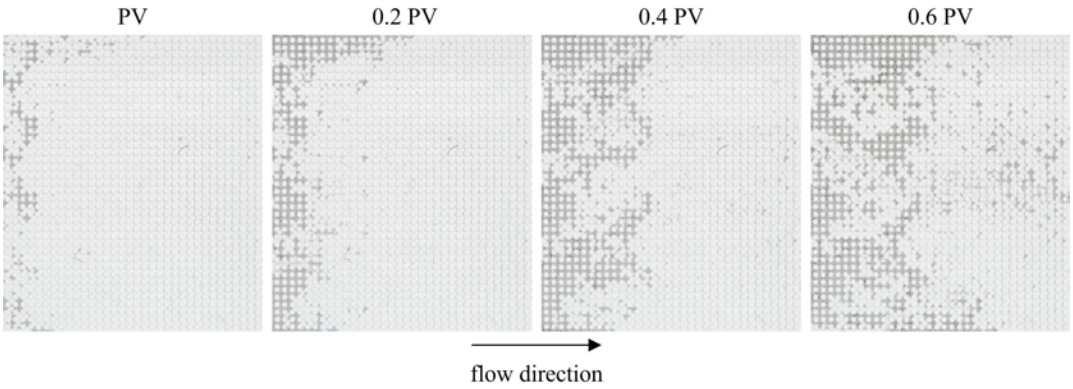

Figure 4.15: Progression of emulsion injection within the network at low capillary number, $Ca = 2{\times}10^{-5}$. Each image was captured after the injection of an additional 0.2 pore volumes.

As more drops populate the medium, they locally reduce the network conductance, leading to long-range dipolar interactions between drops. These interactions induce perturbations in the flow field, causing velocity changes

that affect neighboring drops. This initiates a feedback loop where perturbations propagate through the medium, progressively destabilizing the flow dynamics. Initially stable paths become unstable due to the cumulative effects of perturbations, forcing drops to alter their trajectories and seek new paths.

With drops moving closer together, the likelihood of jams forming increases. As the flow progresses and the drop density rises in the network, the traffic flow becomes intermittent, with jams continuously forming and disrupting [18]. These dynamics create new flow paths, evident in the alternating flow patterns within the medium, as shown in Figure 4.16. The red boxes highlight local changes in flow paths over time.

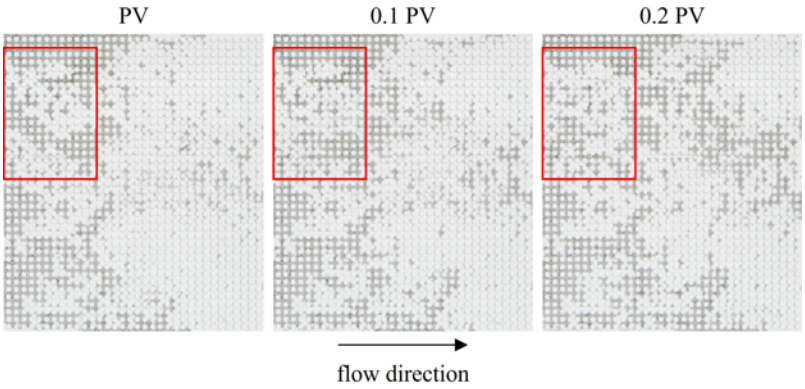

Figure 4.16: Variations in flow patterns resulting from intermittent traffic flow of drops after reaching a critical density within the network.

It is important to mention that a large drop flowing through a constriction can also be split by capillary-driven force, in what is called snap-off [92, 93, 94]. However, emulsion drops used in the experiments were not large enough to suffer snap-off, which was not observed in the experiments reported here.

4.2.1 Small-Drop Emulsion

We first examined the effect of the small-drop emulsion on flow behavior. Figure 4.17 shows the evolution of the injection pressure during the sequential flow of water (4 pore volumes), emulsion (15 pore volumes), and water (15 pore volumes) at the lowest flow rate explored, $Ca = 2{\times}10^{-5}$. During the first water slug, the injection pressure is constant and approximately 0.02 psig. During emulsion injection, marked as the green region in the plot, the pressure starts to increase after approximately 2 pore volumes of injected emulsion. The injection pressure increases until stabilizing at approximately 0.12 psig. After

the injection of the second water slug, the inlet pressure drops to approximately 0.09 psig.

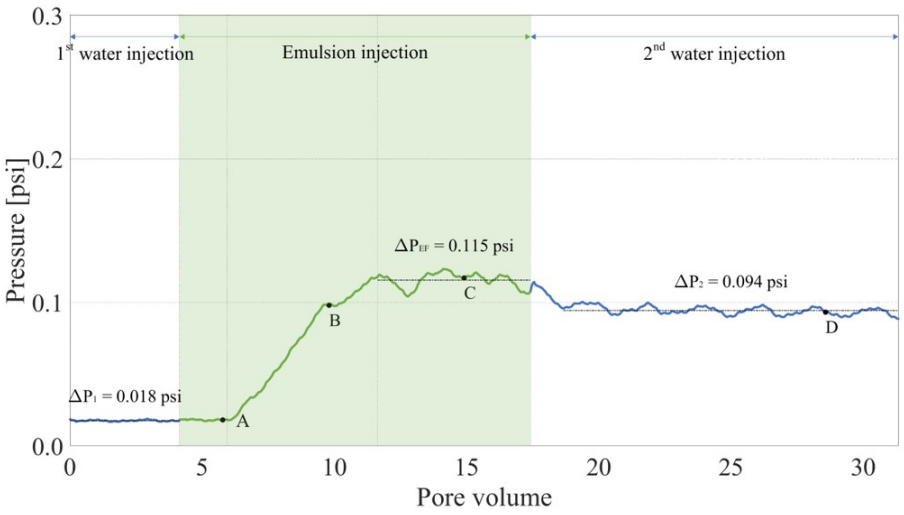

Figure 4.17: Evolution of the pressure difference at $Ca = 2{\times}10^{-5}$.

The drop distribution within the pore space in a region close to the middle of the device at different times (marked in Figure 4.17) is presented in Figure 4.18. The darker areas of the image indicate regions containing oil drops.

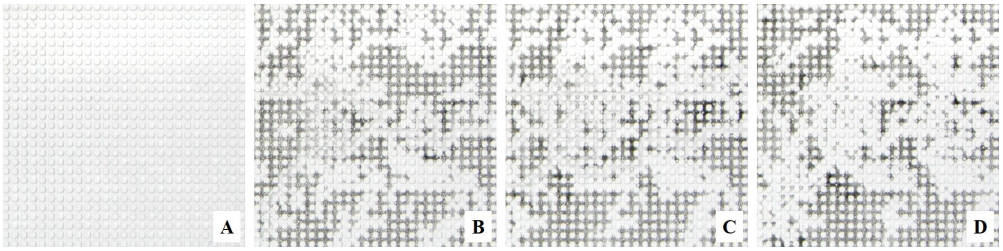

Figure 4.18: Images of the pore space at different times (injected pore volumes) are marked in Figure 4.18. Injected pore volumes (A) 5.8, (B) 10, (C) 15, (D) 28.6. $Ca = 2{\times}10^{-5}$. Images obtained in the bright-field mode.

In the early stage of emulsion injection (A), there are not enough large drops inside the pore space to cause an appreciable reduction in the flow mobility. The observation region did not show any drop. As time evolves, more drops are captured in the pore throats, which leads to higher injection pressures (B and C). At the end of emulsion injection, the number of blocked pore throats is high (C). The second slug of water can remove some of the drops that were blocking pore throats (D), but the number of blocked paths is still high, which explains the relatively high pressure difference at the end of the second water slug.

It is important to note that even after flow stabilization at the end of emulsion injection, the pressure value oscillates, as observed in core flooding experiments [63]. The oscillation is directly related to the dynamics of drop capture and release at different pore throats, which randomly alter the free flow paths. Figure 4.19 illustrates the mobilization of drops during the second water injection. The dashed red arrows in Figure 4.19a indicate the initial flow paths. Over time, the blue-marked drops are mobilized and swept away, creating new flow paths, shown by the solid red arrows in Figure 4.19b. Drops marked in green appear to restrain the flow, causing smaller drops to accumulate near the pore throat entrance. With the establishment of new flow paths, the flow dynamics change, allowing the smaller drops to move past the previously trapped drops.

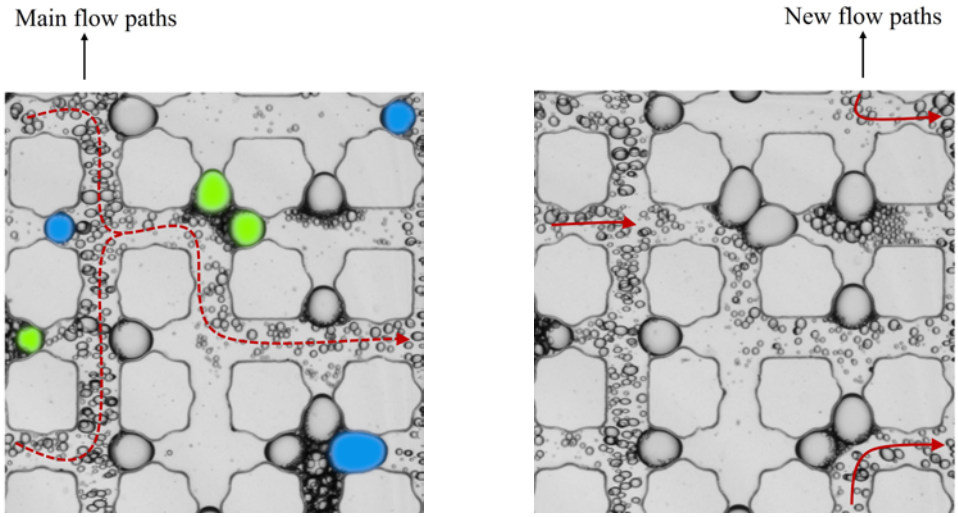

(a) Initial flow paths are indicated by the dashed red arrows. The drops marked in blue are mobilized and swept away, while drops marked in green restrain the flow and cause smaller drops to accumulate.

(b) New flow paths merge where the blue drops were previously trapped, mobilizing smaller droplets near the former green-marked drops. The new flow paths are indicated by the solid red arrows.

Figure 4.19: Time-sequence of images illustrating the intermittent nature of emulsion flow through porous media, showing how different flow paths are created as drops flow through pore throats. Images obtained in bright-field mode.

The evolution of the injection pressure at the highest flow rate explored, $Ca = 6{\times}10^{-4}$, is shown in Figure 4.20. The general behavior is similar but with higher pressure values, as expected. During the first water injection, the pressure is constant and equal to approximately 0.41 psig. During emulsion injection, the pressure rises until it reaches a steady-state value of approximately 0.64 psig. The pressure falls to approximately 0.60 psig after the injection of

the second slug of water.

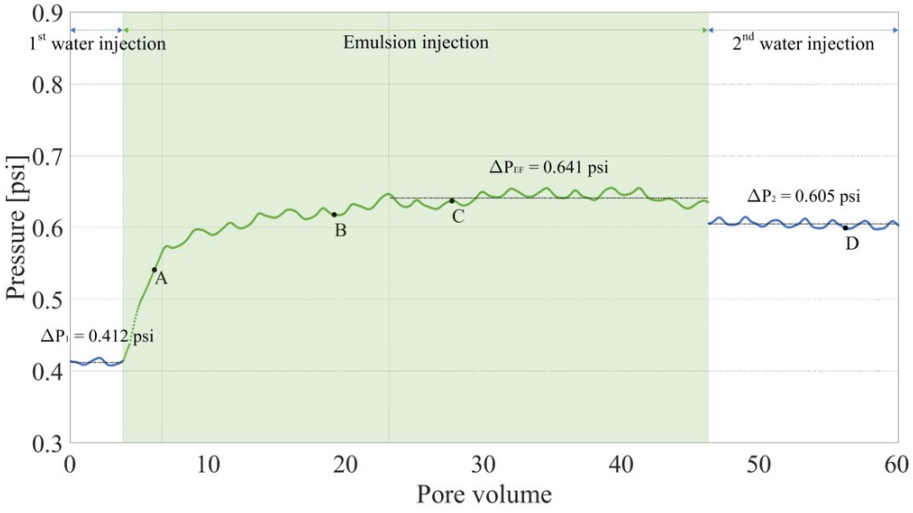

Figure 4.20: Evolution of the pressure difference at $Ca = 6{\times}10^{-4}$.

The relative increase in injection pressure associated with the emulsion slug is less pronounced at high capillary numbers. The higher pressure difference in the flow is sufficient to overcome the capillary pressure, allowing a larger number of drops to pass through the pore throats. Consequently, the number of trapped drops is significantly lower compared to what is observed at low capillary numbers. This difference is evident in the images of the pore space near the middle of the device, captured at various stages of the injection process, as indicated in Figure 4.21 and displayed in Figure 4.20.

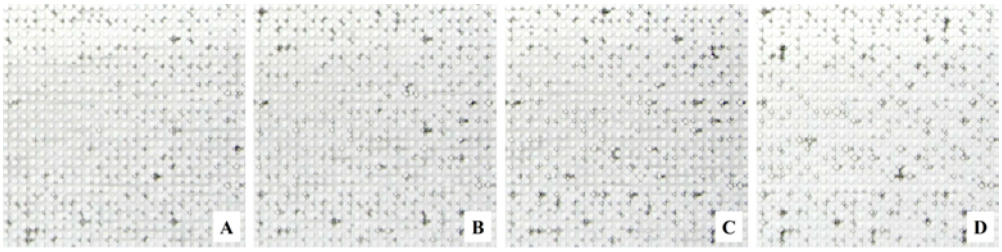

Figure 4.21: Images of the pore space at different times (injected pore volumes) are marked in Figure 4.20. Injected pore volumes (A) 6.2, (B) 19.2, (C) 27.9, (D) 58.5. $Ca = 6{\times}10^{-4}$. Images obtained in the bright-field mode.

4.2.2 Large-Drop Emulsion

The inlet pressure evolution observed with the large-drop emulsion at the lowest and highest flow rates explored are shown in Figures 4.22 and 4.23, respectively. The emulsion injection window is highlighted in yellow in the plot. The behavior is similar to that discussed before and observed for the

small drop emulsion. The inlet pressure rises until it reaches a steady state during the emulsion injection and then falls during the second water slug injection. Because of the larger drops, pore blocking is stronger, and a higher pressure gradient is needed to drive the drops through a pore throat, leading to a larger number of trapped drops. As a direct consequence, the observed injection pressures are higher. As an example, the steady-state pressure at the end of the emulsion slug at a low capillary number, $Ca = 2\times10^{-5}$, was approximately 0.12 psig for the small-drop emulsion and approximately 0.17 psig for the large-drop system.

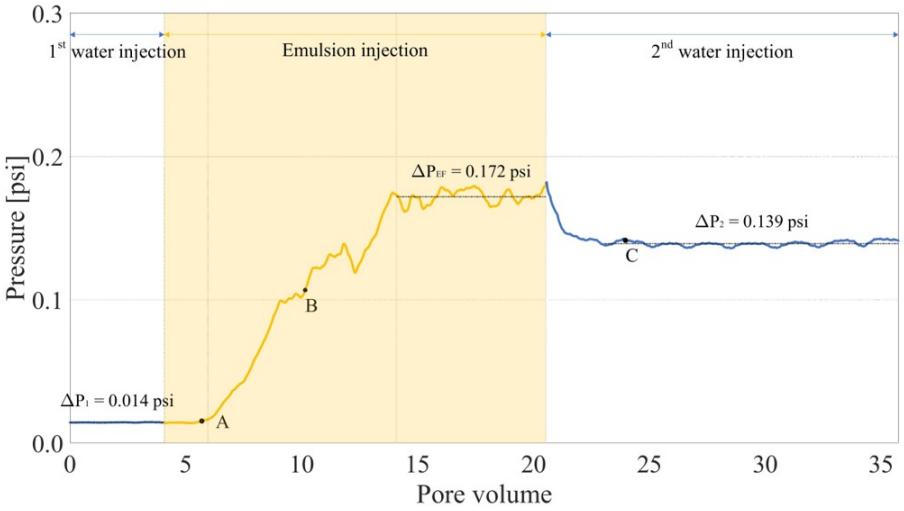

Figure 4.22: Evolution of the pressure difference at $Ca = 2\times10^{-5}$.

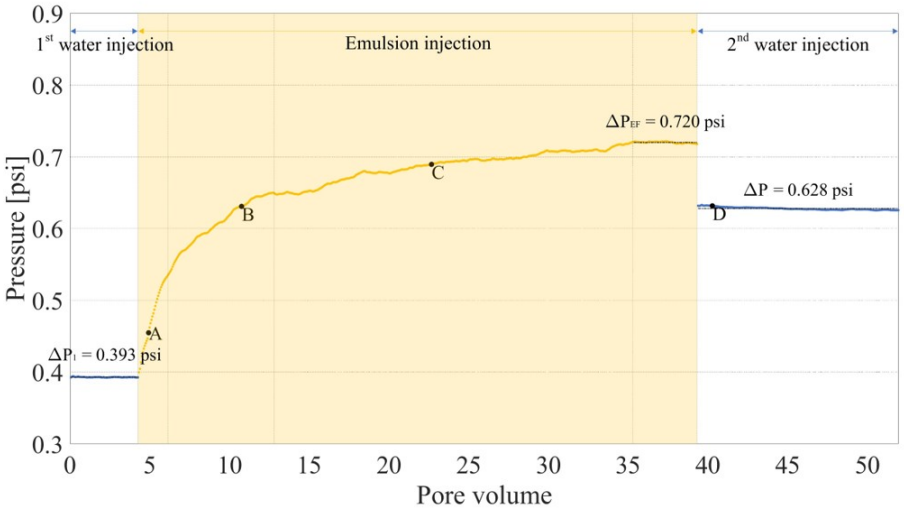

Figure 4.23: Evolution of the pressure difference at $Ca = 6\times10^{-4}$.

To evaluate the reproducibility of the experiments, we repeated the injection procedure with the large-drop emulsion at the low capillary number

flow, which is the case that leads to the strongest pore-blocking effect. The results are presented in Figure 4.24. The evolution of the pressure difference and the steady-state values at the end of the second water slug closely match those shown in Figure 4.23. The relative difference is approximately 3% at the end of the injection procedure.

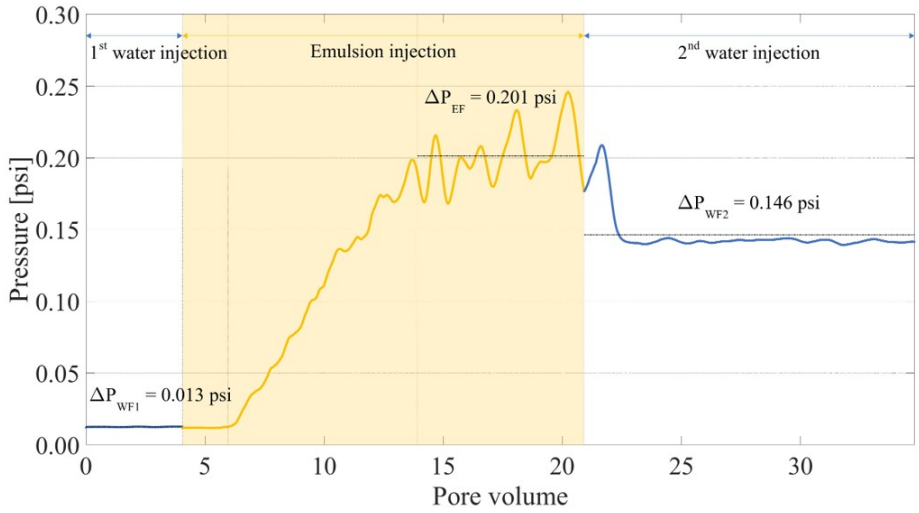

Figure 4.24: Duplicate experiment showing the evolution of the pressure difference during the flow of the large-drop emulsion at $Ca = 5 \times 10^{-5}$.

4.2.3 Resistance Factor and Residual Resistance Factor

The mobility of the aqueous phase at the end of each step of the injection procedure, i.e., first water slug, λ_{wf1}, emulsion injection, λ_{ef}, and second water slug, λ_{wf2}, can be evaluated using Darcy's law and pressure difference measurements:

$$\lambda_{wf1} = \frac{QL}{\Delta P_{wf1}}, \qquad \lambda_{ef} = \frac{QL}{\Delta P_{ef}}, \qquad \lambda_{wf2} = \frac{QL}{\Delta P_{wf2}} \tag{4-2}$$

Since the injection was performed at a constant flow rate, the mobility reduction associated with drop capture in pore throats can be quantified using the resistance factor (RF). The RF is defined as the ratio of the steady-state pressure difference at the end of emulsion injection to that at the end of the first water injection. It is the reciprocal of the mobility reduction factor, f, as defined by Cobos et al., and represents the ratio of the aqueous phase mobility at the end of emulsion injection to that of the first water injection [10].

$$RF = \frac{\Delta P_{ef}}{\Delta P_{wf1}} = \frac{\lambda_{wf1}}{\lambda_{ef}} \tag{4-3}$$

As RF $\rightarrow$ 1, the mobility reduction associated with pore blocking by emulsion drops becomes weaker. On the other extreme, a high value of the RF indicates a strong mobility reduction. Figure 4.25 presents the value of the RF as a function of the capillary number for both small and large drop emulsions. In both cases, the RF falls with the capillary number; mobility reduction is weaker as the capillary number rises. Drops are captured in a pore throat if the pressure difference is not strong enough to overcome the capillary pressure needed to reduce the radius of curvature of a drop as it flows through a constriction. Therefore, at low capillary numbers, the capillary pressure is relatively high compared to the flow pressure drop, and more emulsion drops are captured in the pore throats of the porous medium. As the capillary number rises, the number of drops captured is reduced, and the mobility reduction is not as strong. The value of the RF becomes constant for $Ca > 3\times10^{-4}$ for both emulsions tested.

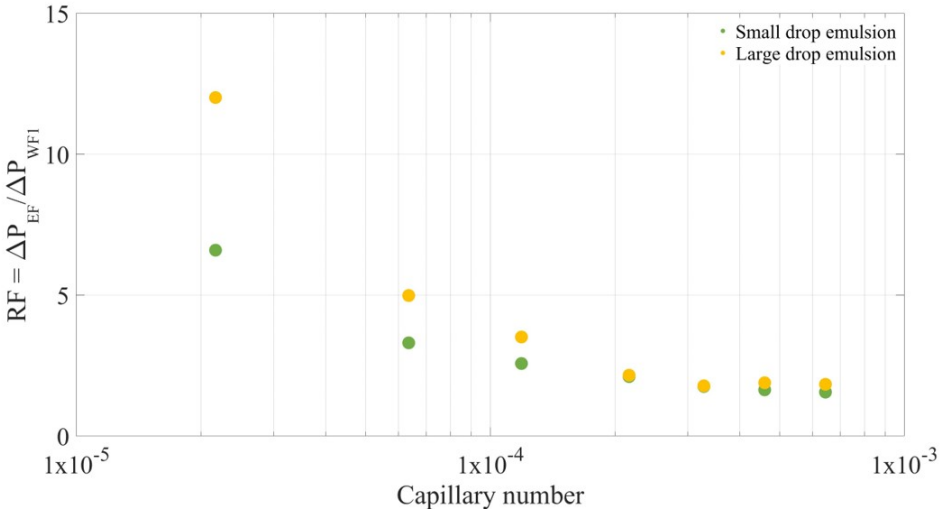

Figure 4.25: The resistance factor as a function of the capillary number for small and large drop emulsions.

For the small-drop emulsion and at the lowest capillary number explored, $Ca = 2\times10^{-5}$, RF $\approx$ 6; the mobility of the aqueous phase containing dispersed drops is 1/6 of the water mobility. At the highest capillary number, $Ca = 6\times10^{-4}$, the resistance factor drops to RF $\approx$ 1.6. The resistance factor is higher for the large-drop emulsion. Larger drops need to deform more as they flow through pore throats, requiring a higher pressure difference to overcome the capillary pressure. At $Ca = 2\times10^{-5}$, RF $\approx$ 12 for the large-drop emulsion. The

results show that the intensity of the aqueous phase mobility reduction can be controlled by both the capillary number and drop-size distribution.

As discussed before, some of the emulsion drops that were retained in the pore throats were displaced during the second water injection, which led to a pressure difference decrease. The steady-state pressure difference at the end of the second water flooding is higher than that observed in the first water injection, indicating a permanent reduction of the water effective permeability. This permanent mobility reduction is quantified by the residual resistance factor (RRF) and represents the ratio of the water mobility after the first and second water slugs.

$$RRF = \frac{\Delta P_{wf2}}{\Delta P_{wf1}} = \frac{\lambda_{wf1}}{\lambda_{wf2}} \tag{4-4}$$

Figure 4.26 presents the residual resistance factor, RRF, as a function of the capillary number for both small and large drop emulsions. At the lower capillary number, the permanent damage is strong with RRF $\approx$ 10 and RRF $\approx$ 5.5 for the large and small drop systems, respectively. As expected, the residual resistance factor is higher for the large drop emulsion since it is harder to displace large drops when compared to small ones. As the capillary number increases, the pressure difference of the flow becomes stronger relative to the capillary pressure, and more drops are displaced during the second water injection, leading to much lower values of RRF. At $Ca = 6{\times}10^{-4}$, RRF $\approx$ 1.5 for the large and small drop systems.

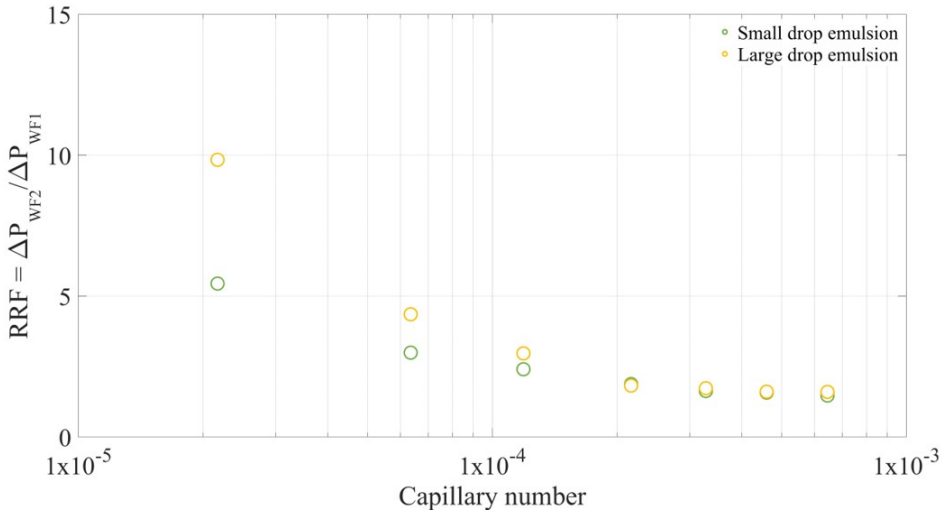

Figure 4.26: The residual resistance factor as a function of the capillary number for small and large drop emulsions.

The pressure difference at the end of the second water slug injection

and, consequently, the permanent mobility reduction are directly associated with the extent of pore blocking by the emulsion drops. Images of different regions of the porous medium at the end of the second water injection were used to quantify the fraction of the pore space occupied by trapped emulsion drops, denoted here as S_D. At the highest capillary number explored, e.g., $Ca = 6{\times}10^{-4}$, $S_D \approx 0.18$ for both small-drop and large-drop systems. It is important to note that the RRF value at high capillary numbers is the same for both systems, e.g., RRF ≈ 1.5. At the lowest capillary number explored, $Ca = 2{\times}10^{-5}$, $S_D \approx 0.64$ for the small-drop emulsion and $S_D \approx 0.68$ for the large-drop emulsion.

5
Emulsion Injection in Radial Flow

This chapter presents the results from the flow behavior of stable O/W emulsion in radial micromodels. It begins with a comprehensive characterization of the devices, including geometric dimensions, pore-size distribution, absolute permeability, and surface wettability. The chapter then analyzes the results from the water-phase mobility tests and discusses the oil displacement achieved through O/W emulsion injection.

5.1
Pore Network Characterization

The radial configuration consisted of a circular porous medium with a 50-mm diameter, as illustrated in Figure 5.1. Surrounding the pore network was a 1-mm wide exit channel designed for uniform fluid drainage. A 2-mm diameter inlet port was placed at the center of the device (A), with eight outlet ports (D) evenly spaced around the circular exit. To accommodate the inlet port, the pore structures at the center were removed, as highlighted in Figure 5.1. Table 5.1 presents the measured dimensions, showing minor deviations from the initial design.

Table 5.1: Geometric dimensions of the radial micromodel.

#	**Inlet port [mm]**	**Outlet port [mm]**	**Exit channel [mm]**	**Porosity [%]**
1	1.83	48.58	1.82	44.6
2	1.82	48.57	1.82	44.8
3	1.92	49.89	1.92	46.8

The pore network comprised 17 × 17 unit cells, arranged laterally in the x and y directions, containing approximately 23,400 square posts. Detailed information on the pore network design is provided in Section 3.2.1. Some posts, particularly those at the boundary, were trimmed to fit the circular geometry, as illustrated in Figure 5.2.

When flowing through porous media, fluid primarily follows low-tortuosity paths, in which the posts align with the pressure gradient. Unlike linear flows, where the pressure gradient directs flow in a single direction, ra-

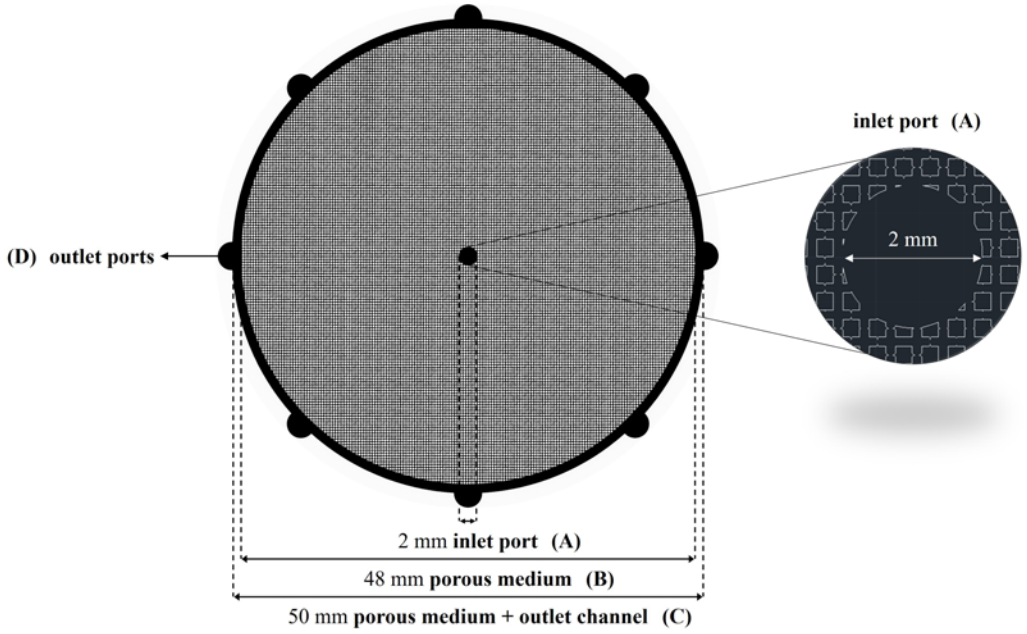

Figure 5.1: The radial micromodel features a circular porous medium with an inlet port at the center and eight evenly spaced outlet ports around the exit channel. The central pore structures were removed to facilitate the inlet port.

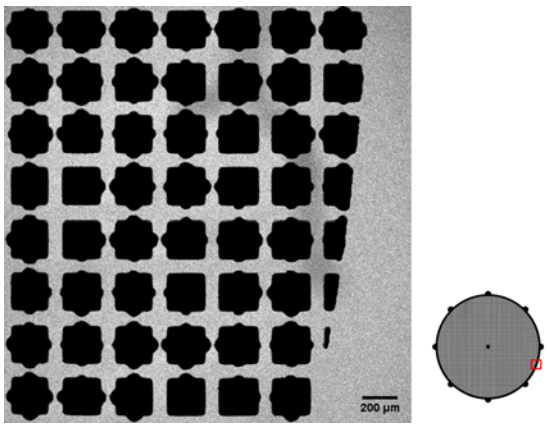

Figure 5.2: The posts (depicted in black) at the boundary of the porous medium were trimmed to fit the circular geometry. The location of the image on the device is highlighted in red. Image obtained using confocal microscopy.

dial flows exhibit a pressure gradient extending outward in all directions from the injection point. In such configurations, tortuosity increases as flow deviates from the orientation of the posts, requiring the fluid to navigate around them to reach the outlet.

Constrictions within the channels further influence flow dynamics. Although the posts are symmetrically arranged, constrictions reduce the spacing between them. The presence of constrictions changes the arrangement of posts from a perfectly regular pattern to a pseudo-regular one, with spacing varying

from 100 μm in unrestricted channels down to 45 μm in constricted channels. This variability affects flow behavior, causing it to transition from homogeneous in highly random lattices to pattern-based in more regular ones [95].

Additionally, in radial flow, the cross-sectional pore area expands with increasing radius, causing the flow velocity to decrease as the fluid moves away from the injection point. Equation 5-1 quantifies this relationship:

$$v_r = -\frac{k}{\mu}\frac{p_e - p_w}{ln(r_e/r_w)}\frac{1}{r} \tag{5-1}$$

Here, v_r represents the radial Darcy flow velocity, k is the permeability of the porous medium, μ is the dynamic viscosity of the fluid, p_e and p_w are the pressures at the boundary and injection point, respectively, r_e and r_w are the radii at those locations, and r is the radial distance from the injection point.

Figure 5.3 illustrates how the Darcy velocity varies at two distinct injection rates, with the colorbar representing the velocity magnitude. The velocity is high near the injection point and decreases rapidly with distance from it. The pressure gradient is also not uniform along the radial direction, being significantly higher closer to the center inlet.

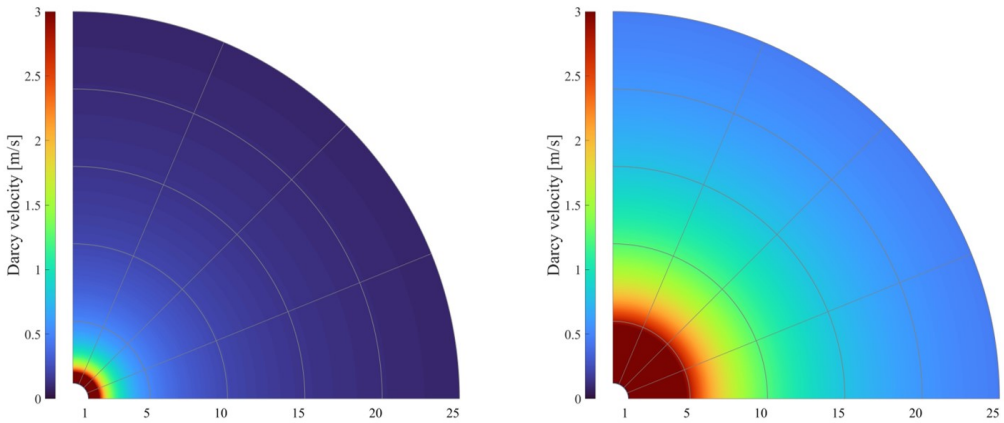

(a) $Q = 3.68$ cch^{-1}. (b) $Q = 20.17$ cch^{-1}.

Figure 5.3: Velocity maps at two distinct injection rates showing how velocity varies with radius.

5.1.1 Channel Size Distribution and Average Height

The size distribution of the measured constrictions is depicted in Figure 5.4, revealing the original categories: small constrictions, large constrictions, and straight channels. Unlike the distribution observed in the rectangular geometry (refer to Section 4.1.1), the radial micromodel exhibited a broader size range

within each peak, indicating greater variability in sizes. The black curve illustrates the multimodal distribution, with modal sizes of 31 μm, 57 μm, and 88 μm for each category, respectively. The deviations from the original design are associated with the limited resolution of the photomask during printing and subsequent inaccuracies in the microfabrication process.

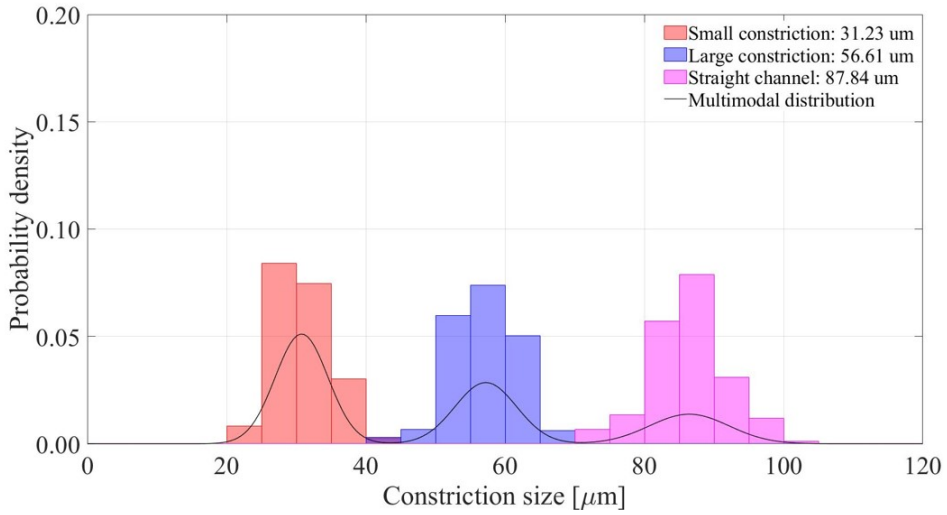

Figure 5.4: Constriction size distribution exhibiting modal sizes of 31 μm, 57 μm, and 88 μm.

The channels exhibited an average height of 81.16 $\pm$ 15.99 μm. Local heights were measured from 676 tiles and analyzed across 28 stacks (refer to Section 3.2.2.1). During image acquisition, the focal plane was adjusted by 11.34 μm between each image, using an optimized pinhole of 500 mAU.

Figure 5.5 shows the image acquisition map, where representative tiles from the porous medium are highlighted in gray. Tiles marked in black were excluded from the height calculation. Images were captured using a 5$\times$ (0.15 NA, HC PL FLUOTAR) dry objective, with a scan speed of 6×10^{-3} ms/pixel and a resolution of 512 $\times$ 512 pixels. Each tile measured 1.55 $\times$ 1.55 mm^2, corresponding to a 5-by-5-pore structure. Local heights were assigned to their respective tiles and assembled to create the porous medium.

A 3D visual representation of the medium was then generated using MATLAB®. The 3D model shown in Figure 5.6 reveals local variations in channel heights, ranging from approximately 66 μm to 103 μm. These height variations can influence the confinement of the drops, causing larger drops to deform not only due to channel constrictions but also when moving through areas with reduced heights.

To enhance resolution, additional points were interpolated between the measured data, resulting in a smoother surface representation. The interpolated data consisted of 19,321 tiles, each measuring 330 $\times$ 330 μm^2.

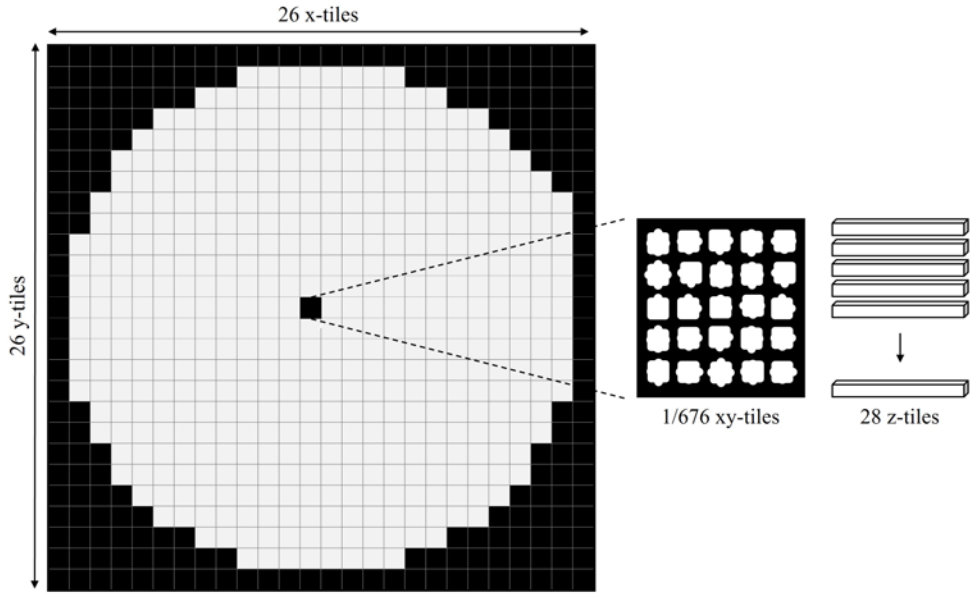

Figure 5.5: A total of 676 tiles, each containing 28 stacks, were analyzed to compute the local heights of the channels. The representative tiles of the porous medium are highlighted in gray.

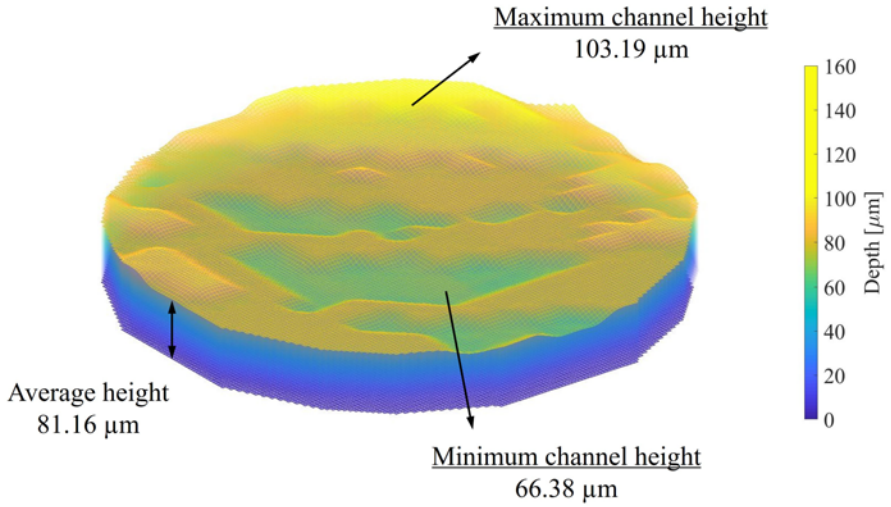

Figure 5.6: 3D topographic model of the radial device generated using MATLAB®.

5.1.2 Porosity and Pore Volume

The porosity (refer to Section 3.2.2.3) was assessed across three devices submitted to identical microfabrication procedures. The resulting values, presented in Table 5.1, indicate a porosity of 0.454 ± 0.012. The pore volume was calculated by multiplying the porous area by the average height, resulting in 65.31 ± 4.46 μL.

The porosity of both the linear and radial geometries is expected to

match, as it is determined solely by geometric factors. The observed differences are primarily due to variations in the constriction sizes, resulting from the photomask printing process, which was outsourced to two different locations.

5.1.3 Absolute permeability

The absolute permeability was determined using Darcy's law, calculated from the slope of the curve, as shown in Figure 5.7. The tests were conducted at flow rates ranging from 2.0 to 16.0 cch^{-1} and yielded a value of approximately 13 D.

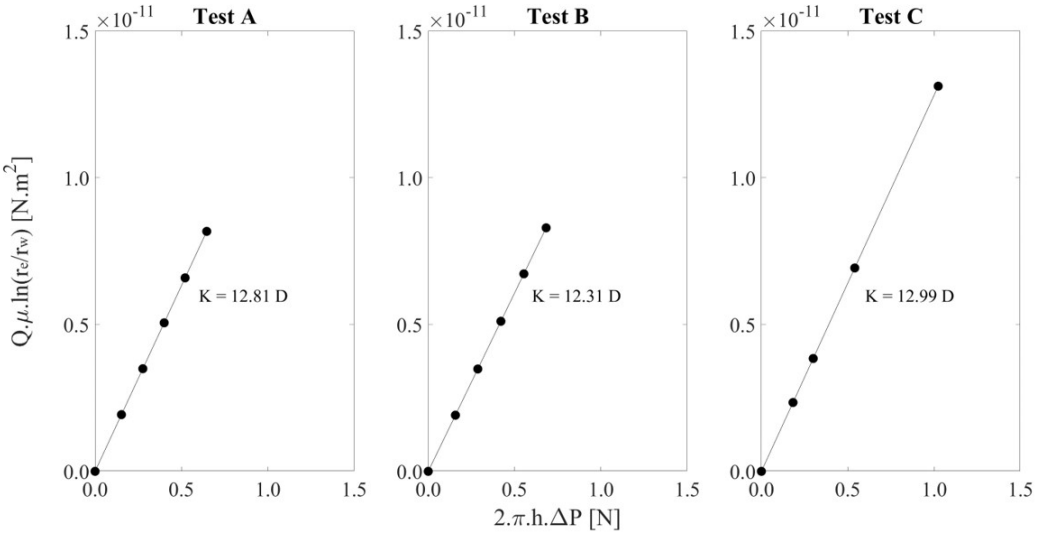

Figure 5.7: Absolute permeability of the porous medium determined using Darcy's law. The tests were conducted at flow rates ranging from 2.0 to 16.0 cch^{-1}, yielding a value of approximately 13 D.

5.1.4 Surface wettability

Contact angle measurements were conducted to simulate the conditions of the oil displacement test. These measurements were performed inside a transparent cell filled with the oleic phase (DKL7 + OG22), as shown in Figure 5.8.

PDMS is inherently hydrophobic. When submitted to plasma treatment, the surface is coated with polar groups and becomes temporarily hydrophilic [79]. In this study, the contact angle between the aqueous phase and the PDMS decreased from 100° to 50° after plasma treatment (refer to Section 4.3). When submerged in the oleic phase, the hydrophobic behavior of untreated PDMS increased, with the contact angle rising from 100° to 140.91° ± 1.93. However, after plasma treatment, the contact angle decreased to 83.52° ± 0.51, a lesser extent compared to the dry environment condition (50°).

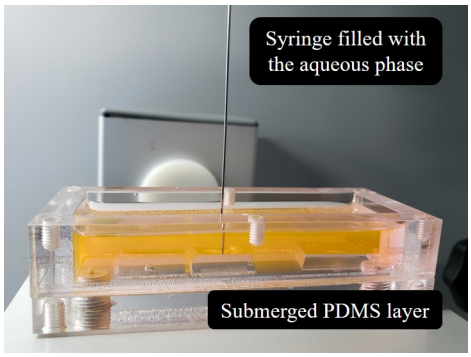

Figure 5.8: Schematic representation of the experimental setup mimicking the oil displacement test.

Plasma treatment also enhanced the spreading of the aqueous phase on the treated glass slide under submerged conditions. In contrast to the rapid spreading observed under atmospheric conditions (refer to Figure 4.8 in Section 4.3), the aqueous phase gradually displaced the oleic phase from the surface of the glass. This displacement process took approximately 135 seconds, after which the contact angle decreased from 62.92° to 24.71°, as illustrated in Figure 5.9.

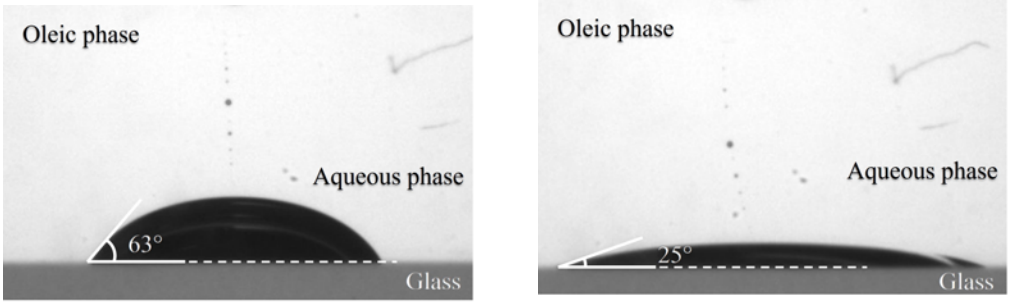

(a) $\theta = 62.92°$ at t = 0 s. (b) $\theta = 24.71°$ at t = 135 s.

Figure 5.9: Contact angle evolution over time. The aqueous phase gradually displaced the oil from the glass surface, leading to a decrease in the contact angle.

5.2 Image acquisition and data analysis

During mobility tests, images were captured using a 5× (0.15 NA, HC PL FLUOTAR) dry objective lens at a scanning speed of 2×10^{-3} ms/pixel. The images had a resolution of 1024 × 1024 pixels, allowing for high-resolution video recording. To create the full image of the pore network, a total of 2025 frames (45 × 45 images) were stitched together.

In the oil displacement experiment, the same 5×/0.15 dry objective lens was used, but with a different scanning speed of 5×10^{-3} ms/pixel. These

images had a resolution of 512 × 512 pixels. To compile the complete image of the porous medium, 784 frames (28 × 28 images) were combined.

Saturation was assessed using four distinct thresholding methods outlined in Section 3.5.2.1. The saturation of each phase was selected based on the method that minimized the number of remaining pixels after subtracting the original image from the thresholded one.

5.3 Flow Tests

Studying the behavior of emulsions in radial flows provides insights into the interaction between viscous and capillary forces and their effect on pore-blocking phenomena. The capillary number, which quantifies the ratio of viscous to capillary forces, is essential for understanding these interactions. In the radial flow experiments, the capillary number was defined at the inlet, situated at the center of the micromodel.

5.3.1 Water-Phase Mobility Tests

In the water-phase mobility test, we investigated the effect of the capillary number on water-emulsion flow at $Ca = 6\times10^{-4}$ and $Ca = 3\times10^{-3}$. Both tests were conducted using the small-drop emulsion system, detailed in Section 3.3.1.

5.3.1.1 Low-capillary number test

We investigated the effect of a small-drop emulsion system on radial flow at $Ca = 6\times10^{-4}$. Figure 5.10 shows the evolution of pressure drop during the sequence of water-emulsion-water injection. The device was initially saturated with the aqueous phase. After the injection of 4 pore volumes of the continuous phase (free of oil drops), 15 pore volumes of emulsion were injected, followed by an additional 15 pore volumes of the aqueous phase.

During the first water slug, the injection pressure remained constant at approximately 0.17 psig. Emulsion injection (marked as the yellow region in the plot) lasted 15 pore volumes, causing the pressure to increase slowly. With continuous injection of emulsion, a steady-state pressure was achieved after 8 pore volumes, stabilizing at 0.50 psig. Emulsion injection continued for an additional 7 pore volumes, after which the aqueous phase injection resumed for another 15 pore volumes, reducing the pressure to 0.44 psig. The higher pressure difference observed during the second water injection indicates

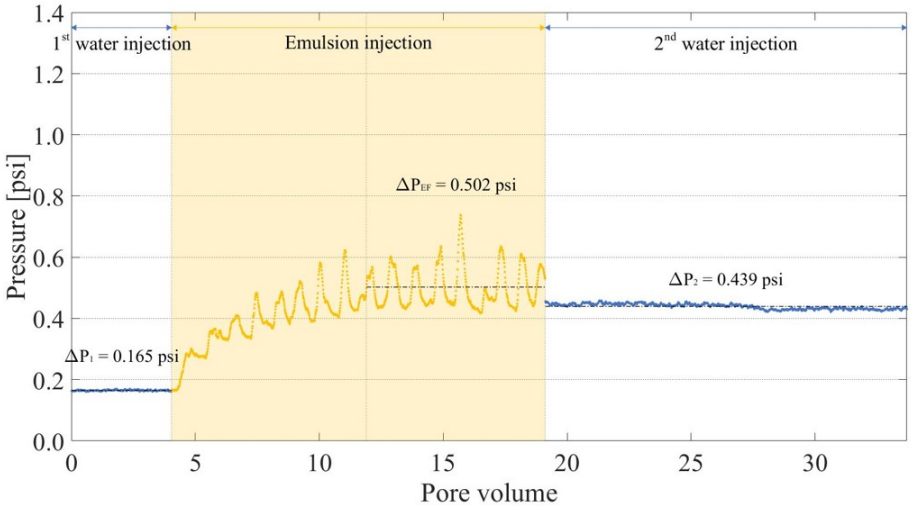

Figure 5.10: Evolution of the pressure difference at $Ca = 6{\times}10^{-4}$.

a permanent reduction in water mobility, suggesting that the drops remained trapped in the pore throats, partially blocking the flow.

Figure 5.11 shows the distribution of drops after emulsion injection. While some drops managed to flow past the constrictions toward the outlet, a significant number became trapped in the medium, even far from the inlet. This suggests that the viscous pressure was sufficient to drive the drops close to the boundary.

Figure 5.11: Final saturation at the end of the second water injection. The aqueous phase is represented in blue and the oleic phase is depicted in yellow.

In radial flow, fluid is expected to flow preferentially through low-tortuosity paths. These paths are characterized by posts aligned with the pressure gradient, as shown in Figure 5.12a. As drops accumulate within these

paths, they locally reduce the network conductance, causing upstream drops to flow around the posts through zig-zagging paths (Figure 5.12b).

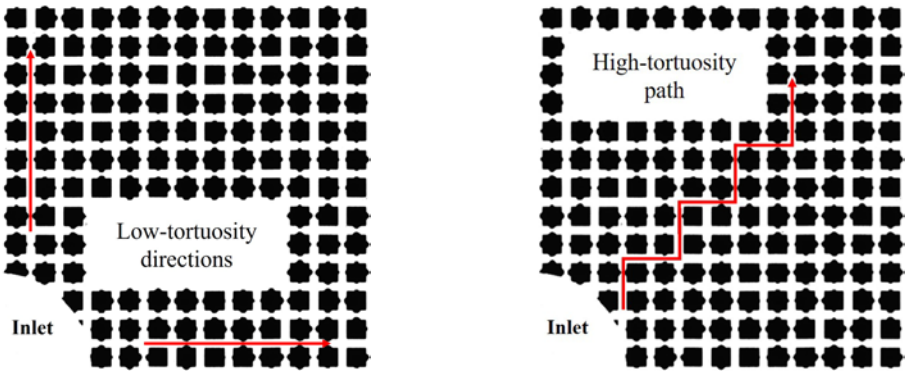

(a) Flow paths with low tortuosity.

(b) Flow paths with high tortuosity.

Figure 5.12: In radial flows, tortuosity increases as flow deviates from the alignment of the posts. The red arrow indicates fluid flow through both low and high tortuosity paths.

Figure 5.13 presents a sequence of images showing drops flowing from the bottom left to the upper right direction in each frame. The drops must maneuver past the posts to traverse the medium. The intermittent change in flow paths results in pressure oscillations [10, 63], as observed during emulsion injection in Figure 5.10.

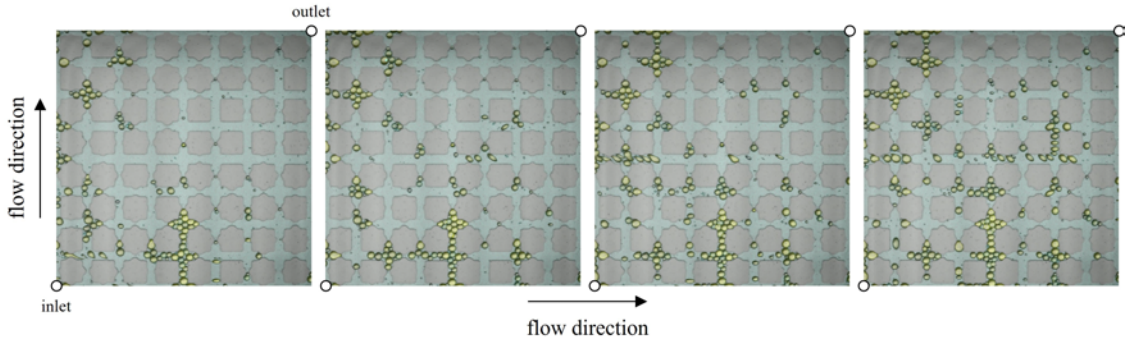

Figure 5.13: The dispersed phase navigates through zig-zagging paths around the posts to reach the outlet of the porous medium. Images obtained using confocal microscopy.

In regular lattice geometries, with symmetrically spaced posts, geometric patterns arise during steady-state flow, creating well-established regions of low and high tortuosity [95]. In this work, the introduction of constrictions disrupted the symmetric distribution of posts, resulting in less pronounced distinctions between these regions. Instead, recurring patterns emerged from the random distribution of constrictions within the grid, being replicated through-

out the medium, as illustrated in Figure 5.14. The drops are represented in white, while the black region encompasses the posts and the aqueous phase. Interestingly, the blocked regions are oriented in the x and y directions, suggesting that the drops initially followed the low-tortuosity paths before becoming trapped.

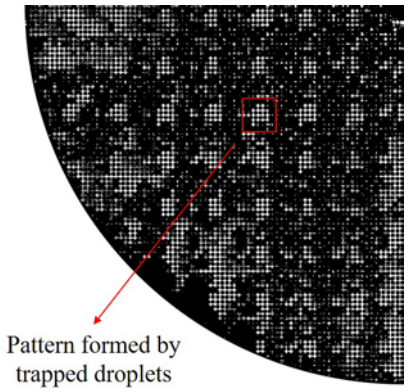

Figure 5.14: Recurring flow patterns resulting from trapped drops.

The flow dynamics were further influenced by the polydisperse emulsion, characterized by drops of varying sizes. Figure 5.15 illustrates the distribution of the drop-to-pore size ratio relative to the channel sizes, providing insights into the local hydrodynamic resistance induced by the drops as they flow through the constrictions. The results indicate that 90% of the drops are smaller than the channel sizes ($D/d < 1$), while the larger drops are approximately the same size or slightly larger than the constrictions ($D/d \approx 1$).

The relationship between pore geometry and drop-size distribution affects the mobility of the drops. The distribution shows that most drops in the system are smaller or comparable to the constriction sizes. This contributed to the mobility of drops and led to continuous changes in their concentration within the medium until a steady state was reached.

At the end of the test, the saturation of the dispersed phase decreased from 47% to 40%, indicating the mobilization of drops following the second water injection. This result is consistent with the pressure difference, which dropped by 12% after the second water slug, decreasing from 0.50 psig to 0.44 psig (Figure 5.10).

5.3.1.2 High-capillary number test

Following the low capillary number test, we investigated the flow behavior of the small-drop system at a higher capillary number, $Ca = 3{\times}10^{-3}$. Figure 5.16 shows the evolution of the pressure drop during the test.

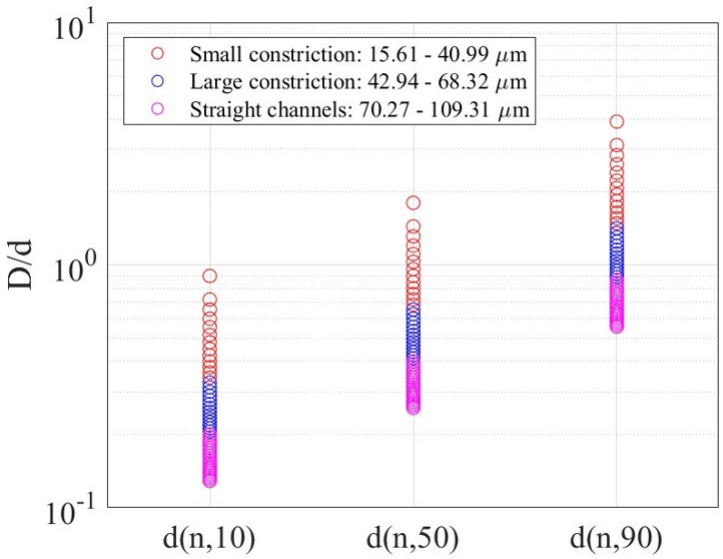

Figure 5.15: Distribution of the ratio between drop and pore throat sizes relative to channel sizes. Small constrictions range from 15 μm to 41 μm, large constrictions range from 43 to 68 μm, and straight channels range from 70 μm to 109 μm.

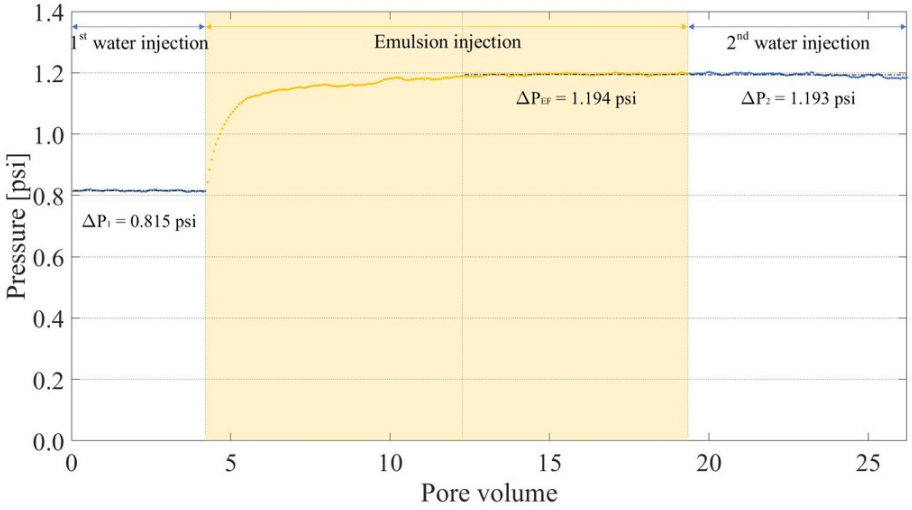

Figure 5.16: Evolution of the pressure difference at $Ca = 3{\times}10^{-3}$.

The behavior was in line with the results from the linear flow tests at high capillary numbers discussed in Chapter 4. During the initial water injection, the pressure remained constant at approximately 0.81 psig. Upon emulsion injection, the pressure increased until stabilizing at a steady-state value of 1.19 psig. This pressure difference was maintained even after the injection of an additional 7 pore volumes of the continuous phase.

Figure 5.17 depicts a region of the porous medium after emulsion injection (Figure 5.17a) and subsequent water flooding (Figure 5.17b). During water flooding, smaller drops were mobilized and moved through the medium, while

larger drops remained trapped in the constrictions due to insufficient viscous pressure to drive them through. Although these small-scale events were visible at the pore scale (Figure 5.17), they were not reflected in the macroscopic pressure behavior, which remained steady at 1.19 psig. This indicates that in high-capillary number flows, viscous forces vastly outweigh capillary effects and govern flow dynamics.

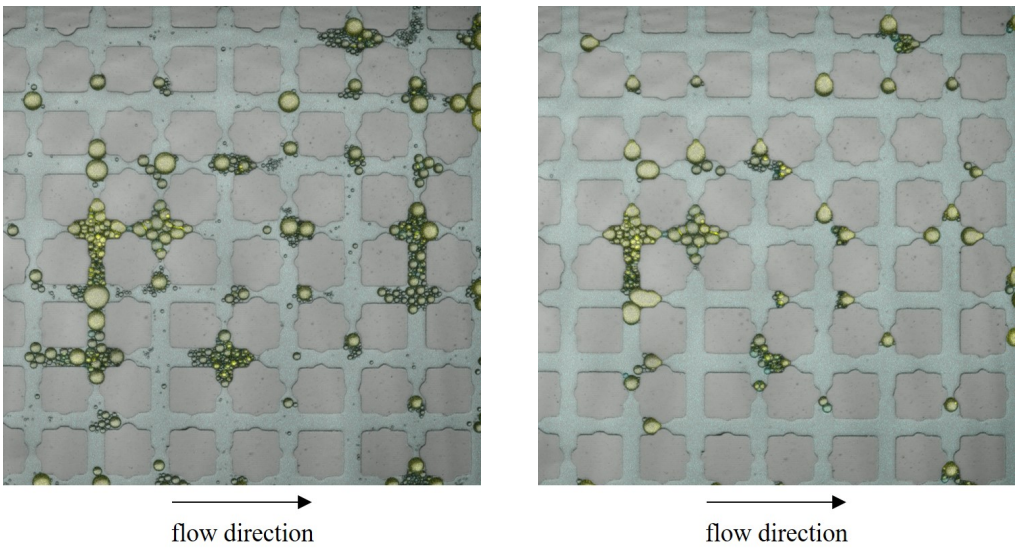

(a) Saturation after emulsion injection.

(b) Saturation after second water injection.

Figure 5.17: Saturation after emulsion injection and second water flooding. The water was able to mobilize only the smaller drops. Images obtained using confocal microscopy.

5.3.2 Oil Displacement Test

Emulsion flooding was conducted to investigate the dynamics of oil displacement by O/W emulsion in radial flow. Initially, the continuous phase, free of oil droplets, was injected into the oil-saturated medium at a flow rate of Q = 1.907 cch^{-1}, corresponding to a capillary number of $Ca = 1{\times}10^{-4}$. The interfacial tension between the oleic phase and the displacing fluid was $\sigma = 8.78$ mN/m.

Figure 5.18 shows the pressure difference and the recovery factor as functions of the injected pore volume. As the continuous phase displaced the oil, the pressure dropped from 0.35 psig to 0.22 psig, achieving a recovery of 79% of the original oil in place. After injecting 65 pore volumes of the continuous phase, the introduction of a 1-pore volume slug of dilute emulsion (with a dispersed phase concentration of 5%) caused the pressure to increase

from 0.22 psig to 0.30 psig, without reaching a steady state. Finally, an additional injection of 30 pore volumes of the continuous phase brought the total recovery to 84%.

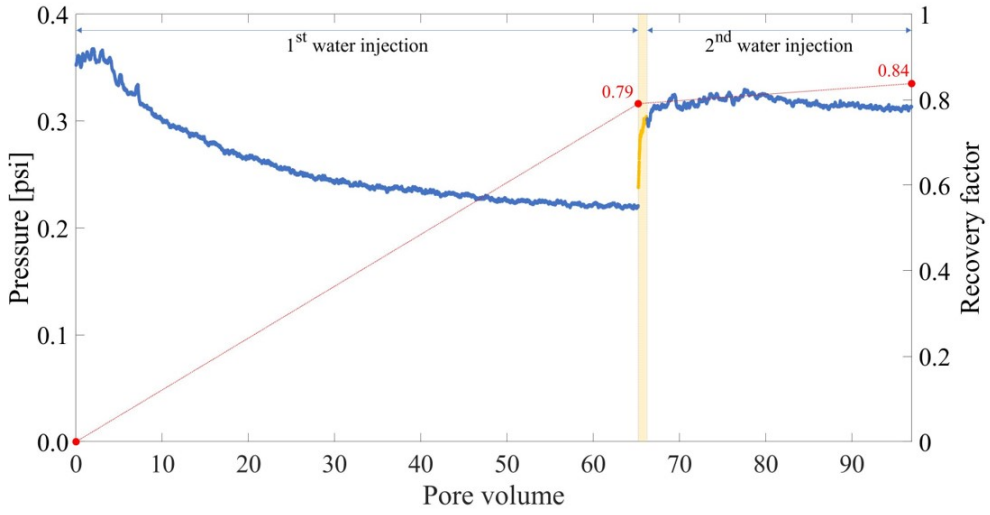

Figure 5.18: Evolution of the pressure difference during the oil displacement test at $Ca = 1{\times}10^{-4}$. The recovery factor is shown on the right axis.

Figure 5.19 illustrates the phase saturations at the end of the test. The aqueous phase is shown in blue, the oleic phase in yellow, and the dispersed phase in magenta. Emulsion drops are primarily trapped near the inlet region, while the residual oil is scattered throughout the medium in the form of oil ganglia. This distribution indicates that the oil was displaced from the inlet area during emulsion injection and subsequent water flooding.

Near the injection point, viscous forces are more pronounced compared to those at the boundary. This happens because in radial flows the velocity depends on the radius. As the fluid moves away from the injection point, capillary forces become increasingly significant. With fewer droplets within the medium, interactions are concentrated in a smaller area, causing localized pressure perturbations. These perturbations destabilize flow dynamics, leading to the opening of new flow paths and facilitating the mobilization of trapped oil. The drops continue to flow until capillary forces restrict their movement at a critical capillary number.

Further results demonstrate how emulsion flooding effectively controlled the mobility of the aqueous phase, leading to additional oil recovery. Figure 5.20 illustrates the oleic phase saturation before and after emulsion injection. After being displaced by the aqueous phase, oil appeared scattered throughout the medium, accumulating near the outlet channel (Figure 5.20a). At this point, the remaining oil within the pore space was immobile, with no changes in the aqueous phase flow paths. During emulsion injection, the flow

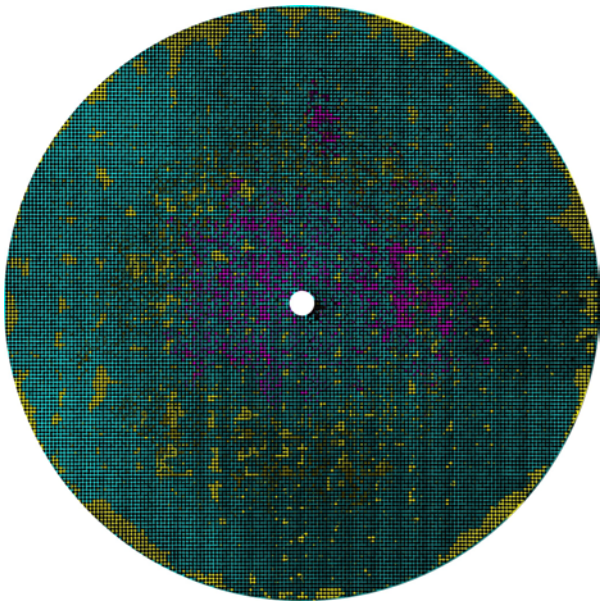

Figure 5.19: Fluid saturation at the end of the test. The aqueous phase is depicted in blue, the oleic phase in yellow, and the dispersed phase in magenta. Emulsion drops appear trapped around the inlet after the second water injection.

equilibrium was disrupted, with drops causing local pressure perturbations, altering the flow dynamics near the injection point. As a result, a distinct clear region around the inlet emerged (Figure 5.20b), indicating the radial displacement of initially trapped oil towards the outlet. The oleic phase saturation decreased from 20% to 16% after emulsion injection.

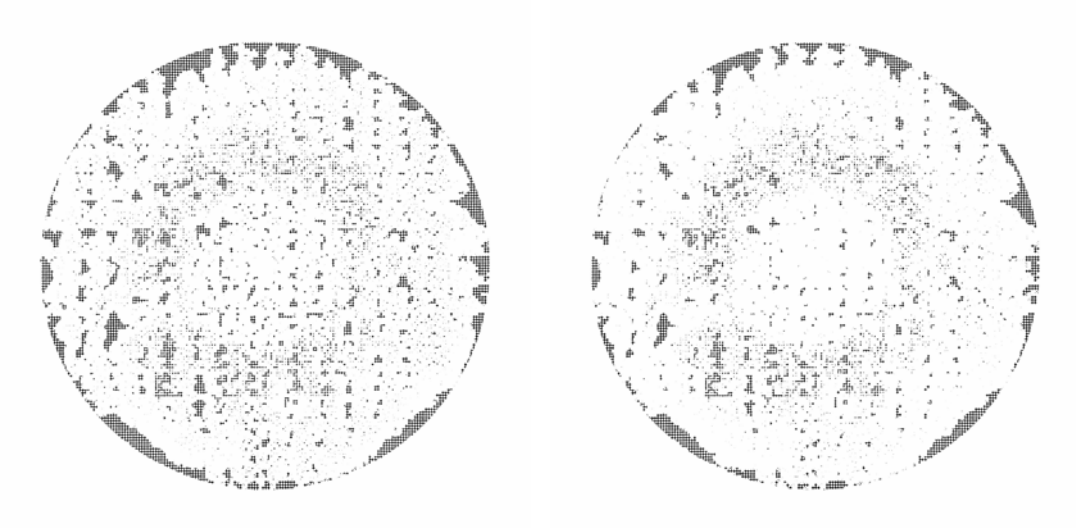

(a) Oleic phase saturation after the first water injection.

(b) Oleic phase saturation after the second water injection.

Figure 5.20: Oleic phase saturation after the first (a) and second (b) water injection. The oleic phase is represented in black. The posts and the other phases are depicted in white. The residual oil saturation within the medium decreased from 21% to 16%.

While displacing the initial oil saturating the porous medium, the aqueous phase exhibited a homogeneous distribution across the pore space (left image in Figure 5.21). As emulsion injection begins, the aqueous phase becomes predominantly mobilized near the inlet (middle image in Figure 5.21). The areas previously occupied by the aqueous phase are now filled with emulsion drops. The right image in Figure 5.21 illustrates the saturation of the aqueous phase superimposed with that of the dispersed phase, depicted in magenta.

The difference in saturation after the first and second water injection is subtle, rising from 79% to 80%. The dispersed phase contributed to 4% of the total saturation. Despite the slight increase in saturation, the additional recovery of 23% of oil confirms the diversion of the aqueous phase to adjacent channels, improving the microscopic sweep efficiency. This is corroborated by the pressure data (Figure 5.18), which shows an increase from 0.22 psig after the first water injection to 0.32 psig during the second water injection, indicating a permanent reduction in the mobility of the aqueous phase.

The presence of oil drops significantly affects the flow dynamics within the porous medium. By displacing the aqueous phase near the inlet, the drops induce local pressure perturbations, facilitating the formation of new flow paths for the aqueous phase.

As the drops enters the pore space, they spread radially from the injection point, advancing in a regular circular front, as illustrated in Figure 5.22. Due to

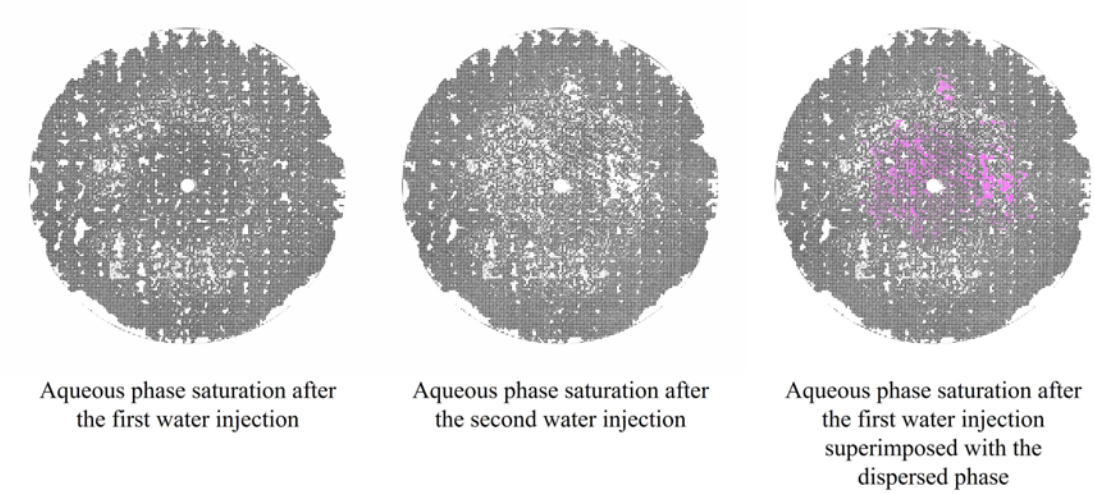

Figure 5.21: Aqueous phase saturation after the first and second water injections. The right image shows the aqueous phase saturation superimposed with that of the dispersed phase, depicted in magenta. In all images, the aqueous phase is represented in black, while the posts and the other phases are shown in white. The aqueous phase saturation within the medium remained relatively constant, increasing slightly from 79% to 80%.

the limited amount of emulsion injected (1 PV), the drops become concentrated near the inlet. Following emulsion injection, the aqueous phase drives the drops deeper into the porous medium until capillary forces prevent further movement.

Figure 5.22: Dispersed phase saturation following the second water injection. The aqueous phase is represented in black, while the posts and the other phases are shown in white. The dispersed phase saturation within the medium was 4%.

Figure 5.23 shows the behavior of the capillary number as a function of the radius. The capillary number is higher near the inlet and decreases as the

fluid moves toward the outlet. During the second water injection, the viscous pressure displaces the drops until the capillary forces hinder their movement at approximately r = 9.5 mm, marked by the red circle in Figure 5.23. This radius corresponds to a critical capillary number, which in this test was $Ca = 2{\times}10^{-5}$.

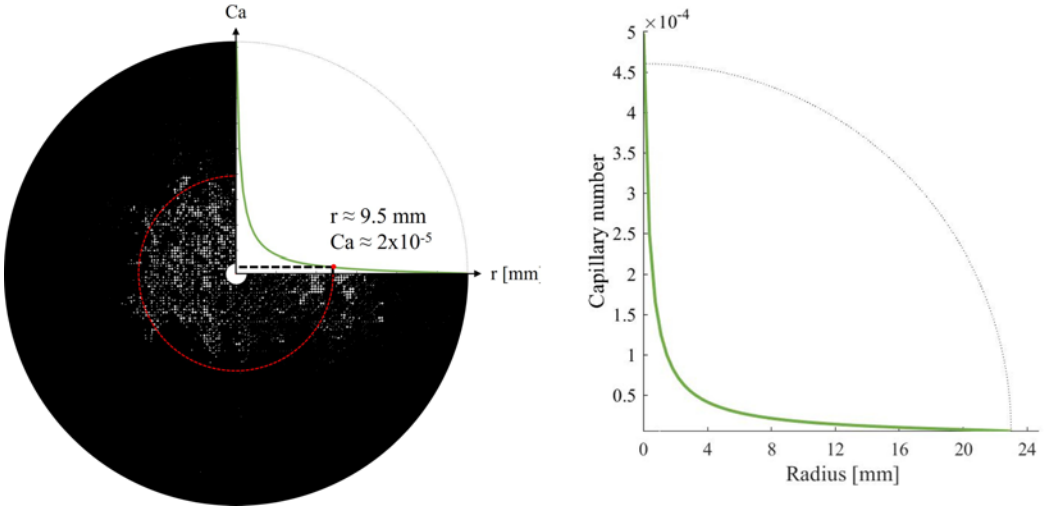

Figure 5.23: The critical radius at which capillary forces become dominant is marked by the red circle. This radius is associated with a critical capillary number of $Ca = 2{\times}10^{-5}$.

Understanding the flow dynamics of emulsion in radial flows is crucial, particularly for identifying the radius at which pore blocking occurs. The radius represents the critical capillary number where capillary forces dominate, thereby controlling the movement of emulsion drops. The trapping of drops occurs below this threshold value, as shown in Figure 5.23.

6
Conclusions

This study employed an experimental microfluidic approach to explore emulsion flow dynamics in porous media, examining various flow conditions and drop-size distributions. The investigation involved injecting polydisperse emulsions into both linear and radial micromodels with varying pore throat sizes to evaluate the effects on the displacing aqueous phase mobility.

In the linear flow experiments, emulsions with different drop-size distributions were injected at varying flow rates to assess how drop size and flow conditions influence mobility reduction. The resistance factor (RF) and residual resistance factor (RRF) were used to quantify mobility reduction as functions of drop-size distribution and capillary number. By combining pore-scale visualization with pressure difference measurements, we were able to correlate pore-scale phenomena with macroscopic flow behavior.

The findings revealed that at high capillary numbers, the pressure difference across pore throats was generally sufficient to overcome the capillary resistance needed to deform drops, resulting in minimal trapping and limited mobility reduction. In contrast, at low capillary numbers, drops were unable to deform sufficiently to pass through constrictions, leading to significant trapping and mobility reduction. Larger drops, requiring higher pressure to pass through constrictions, resulted in greater pore blockage compared to smaller drops.

In systems with smaller drops, the mobility was higher due to the drops being periodically squeezed through pore throats, causing intermittent flow path changes. Conversely, larger drops exhibited increased trapping and reduced flow path variability due to the higher pressure required to overcome constriction resistance.

Droplet concentration also played a critical role in flow dynamics. Higher concentrations of droplets led to enhanced interactions and long-range perturbations within porous media, resulting in alternating periods of movement and trapping. This cycle persisted until no more drops were injected and the flow reached a steady state with minimal further movement of drops.

Radial flow experiments highlighted the influence of the capillary number on droplet trapping. Below a critical capillary number, capillary forces effectively trap droplets in pore constrictions. This critical value is associated with

a specific radial distance from the inlet. Near the injection point, viscous forces dominate, whereas capillary forces become more significant further from the inlet. Droplets continue to flow until capillary forces restrict their movement at the critical capillary number.

The study also demonstrated that effective emulsion flooding does not necessarily require high droplet concentrations. Even at lower concentrations, emulsions can mobilize oil efficiently without significantly reducing the permeability of porous media. Localized pressure perturbations associated with the trapping of droplets affect the overall flow dynamics, redirecting the flow of water and further mobilizing trapped oil.

These findings provide valuable insights for designing enhanced oil recovery (EOR) strategies using emulsion injection. They indicate the optimal emulsion drop-size distribution required for achieving the desired aqueous phase mobility reduction and improved oil recovery. Furthermore, the results underscore the utility of porous medium micromodels and microfluidic techniques as cost-effective and rapid alternatives to core flooding experiments for evaluating different formulations.

6.1 Future Work

Future research could involve conducting oil displacement experiments in radial micromodels at higher capillary numbers, sufficient to produce the mobilized oleic phase. The results from the oil displacement test (Section 5.3.2) show that the oleic phase was mobilized near the inlet and the viscous pressure was not high enough to displace the oil to the outlet, leading to its retention near the boundaries of the micromodel. This resulted in oil being trapped within the micromodel, which did not significantly impact additional recovery after the second water injection.

In addition to increasing the capillary number, increasing the size of the emulsion slug could promote deeper penetration of droplets within porous media, allowing them to reach regions farther from the injection point. It is important to note that a larger slug size would provide more droplets available for trapping in the pore throats, thus requiring a higher pressure drop to overcome the accumulated trapping. Higher pressure drop occurs near the injection point, potentially driving larger drops further away from the central inlet.

Regarding the fabrication of the radial micromodels, future work could focus on designing grids with different post orientations to investigate the influence of pore geometry on the radial flow of emulsions. As demonstrated in

Section 5.3.1.1, post orientation has a significant impact on flow paths in radial geometries. Additionally, pressure measurements at various radii could be performed to determine the critical pressure drop at which capillary resistance dominates the flow.

For O/W emulsions, future work could encompass formulating monodisperse emulsions to evaluate the degree of trapping under different drop-size distributions. In polydisperse systems, smaller drops disturb the local flow within channels, increasing the likelihood of upstream drops altering their flow paths. Monodisperse emulsions could help isolate the hydrodynamic effects of smaller drops within the pore network.

Bibliography

1 GREEN, D. W.; WILLHITE, G. P. Enhanced oil recovery–2nd edition. **Society of Petroleum Engineers**, 2018.

2 LENORMAND, R.; ZARCONE, C. Capillary fingering: percolation and fractal dimension. **Transport in porous media**, Springer, v. 4, p. 599–612, 1989.

3 JOEKAR-NIASAR, V.; HASSANIZADEH, S. Analysis of fundamentals of two-phase flow in porous media using dynamic pore-network models: a review. **Critical reviews in environmental science and technology**, Taylor & Francis, v. 42, n. 18, p. 1895–1976, 2012.

4 FERRARI, A. et al. Challenges in modeling unstable two-phase flow experiments in porous micromodels. **Water Resources Research**, Wiley Online Library, v. 51, n. 3, p. 1381–1400, 2015.

5 MARTÍNEZ-PALOU, R. et al. Transportation of heavy and extra-heavy crude oil by pipeline: A review. **Journal of petroleum science and engineering**, Elsevier, v. 75, n. 3-4, p. 274–282, 2011.

6 LEE, R. F. Agents which promote and stabilize water-in-oil emulsions. **Spill Science & Technology Bulletin**, Elsevier, v. 5, n. 2, p. 117–126, 1999.

7 KOKAL, S. L. Crude oil emulsions. **Petroleum Engineering Handbook**, Society of Petroleum Engineers Richardson, TX., v. 1, p. 533–570, 2006.

8 MCAULIFFE, C. D. Oil-in-water emulsions and their flow properties in porous media. **Journal of petroleum technology**, SPE, v. 25, n. 06, p. 727–733, 1973.

9 YU, L. et al. Plugging ability of oil-in-water emulsions in porous media: experimental and modeling study. **Industrial & Engineering Chemistry Research**, ACS Publications, v. 57, n. 43, p. 14795–14808, 2018.

10 COBOS, S.; CARVALHO, M.; ALVARADO, V. Flow of oil–water emulsions through a constricted capillary. **International Journal of Multiphase Flow**, Elsevier, v. 35, n. 6, p. 507–515, 2009.

11 ROMERO, M. I.; CARVALHO, M. S.; ALVARADO, V. Experiments and network model of flow of oil-water emulsion in porous media. **Physical Review E**, APS, v. 84, n. 4, p. 046305, 2011.

12 GUILLEN, V.; CARVALHO, M.; ALVARADO, V. Pore scale and macroscopic displacement mechanisms in emulsion flooding. **Transport in Porous Media**, Springer, v. 94, n. 1, p. 197–206, 2012.

13 SOO, H.; RADKE, C. J. Flow mechanism of dilute, stable emulsions in porous media. **Industrial & engineering chemistry fundamentals**, ACS Publications, v. 23, n. 3, p. 342–347, 1984.

14 ESCALANTE, J. D. F. **Relative permeability measurement and two-phase flow visualization in micromodels of vugular porous media**. PhD thesis — PUC-Rio, 2023.

15 DATTA, S. S. et al. Spatial fluctuations of fluid velocities in flow through a three-dimensional porous medium. **Physical review letters**, APS, v. 111, n. 6, p. 064501, 2013.

16 HAK, M. Gad-el. The fluid mechanics of microdevices—the freeman scholar lecture. 1999.

17 BELLOUL, M. et al. Competition between local collisions and collective hydrodynamic feedback controls traffic flows in microfluidic networks. **Physical Review Letters**, APS, v. 102, n. 19, p. 194502, 2009.

18 CHAMPAGNE, N. et al. Traffic jams and intermittent flows in microfluidic networks. **Physical review letters**, APS, v. 105, n. 4, p. 044502, 2010.

19 BEATUS, T. et al. Two-dimensional flow of driven particles: a microfluidic pathway to the non-equilibrium frontier. **Chemical Society Reviews**, Royal Society of Chemistry, v. 46, n. 18, p. 5620–5646, 2017.

20 ANBARI, A. et al. Microfluidic model porous media: Fabrication and applications. **Small**, Wiley Online Library, v. 14, n. 18, p. 1703575, 2018.

21 CHANDLER, R. et al. Capillary displacement and percolation in porous media. **Journal of Fluid Mechanics**, Cambridge University Press, v. 119, p. 249–267, 1982.

22 WILKINSON, D.; WILLEMSEN, J. F. Invasion percolation: a new form of percolation theory. **Journal of physics A: Mathematical and general**, IOP Publishing, v. 16, n. 14, p. 3365, 1983.

23 SUN, Z.; SANTAMARINA, J. C. Haines jumps: Pore scale mechanisms. **Physical review E**, APS, v. 100, n. 2, p. 023115, 2019.

24 LENORMAND, R. Statistical physics and immiscible displacements through porous media. **Physics and Chemistry of Porous Media II**, v. 154, p. 98–115, 1987.

25 LENORMAND, R.; TOUBOUL, E.; ZARCONE, C. Numerical models and experiments on immiscible displacements in porous media. **Journal of fluid mechanics**, Cambridge University Press, v. 189, p. 165–187, 1988.

26 ZHAO, B.; MACMINN, C. W.; JUANES, R. Wettability control on multiphase flow in patterned microfluidics. **Proceedings of the National Academy of Sciences**, National Acad Sciences, v. 113, n. 37, p. 10251–10256, 2016.

27 JUNG, M. et al. Wettability controls slow immiscible displacement through local interfacial instabilities. **Physical Review Fluids**, APS, v. 1, n. 7, p. 074202, 2016.

28 AVENDAÑO, J. et al. Effect of surface wettability on immiscible displacement in a microfluidic porous media. **Energies**, MDPI, v. 12, n. 4, p. 664, 2019.

29 JAMIN, M. Xxvii. on the equilibrium and motion of liquids in porous bodies. **The London, Edinburgh, and Dublin Philosophical Magazine and Journal of Science**, Taylor & Francis, v. 19, n. 126, p. 204–207, 1860.

30 CHATZIS, I.; MORROW, N. R.; LIM, H. T. Magnitude and detailed structure of residual oil saturation. **Society of Petroleum Engineers Journal**, SPE, v. 23, n. 02, p. 311–326, 1983.

31 LENORMAND, R.; ZARCONE, C.; SARR, A. Mechanisms of the displacement of one fluid by another in a network of capillary ducts. **Journal of Fluid Mechanics**, Cambridge University Press, v. 135, p. 337–353, 1983.

32 MOHANTY, K. K.; DAVIS, H. T.; SCRIVEN, L. Physics of oil entrapment in water-wet rock. **SPE Reservoir Engineering**, SPE, v. 2, n. 01, p. 113–128, 1987.

33 MELROSE, J. Role of capillary forces in detennining microscopic displacement efficiency for oil recovery by waterflooding. **Journal of Canadian Petroleum Technology**, OnePetro, v. 13, n. 04, 1974.

34 LARSON, R.; DAVIS, H.; SCRIVEN, L. Displacement of residual nonwetting fluid from porous media. **Chemical Engineering Science**, Elsevier, v. 36, n. 1, p. 75–85, 1981.

35 GEISTLINGER, H. et al. The impact of pore structure and surface roughness on capillary trapping for 2-d and 3-d porous media: Comparison with percolation theory. **Water Resources Research**, Wiley Online Library, v. 51, n. 11, p. 9094–9111, 2015.

36 KRUMMEL, A. T. et al. Visualizing multiphase flow and trapped fluid configurations in a model three-dimensional porous medium. **AIChE Journal**, Wiley Online Library, v. 59, n. 3, p. 1022–1029, 2013.

37 DATTA, S. S.; DUPIN, J.-B.; WEITZ, D. A. Fluid breakup during simultaneous two-phase flow through a three-dimensional porous medium. **Physics of Fluids**, AIP Publishing, v. 26, n. 6, 2014.

38 MA, K. et al. Visualization of improved sweep with foam in heterogeneous porous media using microfluidics. **Soft Matter**, Royal Society of Chemistry, v. 8, n. 41, p. 10669–10675, 2012.

39 CONN, C. A. et al. Visualizing oil displacement with foam in a microfluidic device with permeability contrast. **Lab on a Chip**, Royal Society of Chemistry, v. 14, n. 20, p. 3968–3977, 2014.

40 OSEI-BONSU, K.; GRASSIA, P.; SHOKRI, N. Investigation of foam flow in a 3d printed porous medium in the presence of oil. **Journal of colloid and interface science**, Elsevier, v. 490, p. 850–858, 2017.

41 CLARKE, A. et al. Mechanism of anomalously increased oil displacement with aqueous viscoelastic polymer solutions. **Soft matter**, Royal Society of Chemistry, v. 11, n. 18, p. 3536–3541, 2015.

42 LIMA, N. M.; AVENDAÑO, J.; CARVALHO, M. S. Effect of viscoelasticity on oil displacement in a microfluidic porous medium. **Journal of the Brazilian Society of Mechanical Sciences and Engineering**, Springer, v. 44, n. 4, p. 144, 2022.

43 AZIZOV, I.; DUDEK, M.; ØYE, G. Studying droplet retention in porous media by novel microfluidic methods. **Chemical Engineering Science**, Elsevier, v. 248, p. 117152, 2022.

44 AMORIM, C. de et al. Visualization and quantification of mobility reduction in porous media flow associated with pore blocking by emulsion drops. **Industrial & Engineering Chemistry Research**, ACS Publications, v. 62, n. 51, p. 22093–22102, 2023.

45 WALSTRA, P. Principles of emulsion formation. **Chemical engineering science**, Elsevier, v. 48, n. 2, p. 333–349, 1993.

46 MCCLEMENTS, D. J. Critical review of techniques and methodologies for characterization of emulsion stability. **Critical reviews in food science and nutrition**, Taylor & Francis, v. 47, n. 7, p. 611–649, 2007.

47 HALL, S. et al. Droplet break-up by in-line silverson rotor–stator mixer. **Chemical Engineering Science**, Elsevier, v. 66, n. 10, p. 2068–2079, 2011.

48 KOKAL, S. Crude-oil emulsions: A state-of-the-art review. **SPE Production & facilities**, SPE, v. 20, n. 01, p. 5–13, 2005.

49 HE, L. et al. Interfacial sciences in unconventional petroleum production: from fundamentals to applications. **Chemical Society Reviews**, Royal Society of Chemistry, v. 44, n. 15, p. 5446–5494, 2015.

50 GOODARZI, F.; ZENDEHBOUDI, S. A comprehensive review on emulsions and emulsion stability in chemical and energy industries. **The Canadian Journal of Chemical Engineering**, Wiley Online Library, v. 97, n. 1, p. 281–309, 2019.

51 SCHRAMM, L. L. et al. Fundamentals and applications in the petroleum industry. **Adv. Chem**, v. 231, p. 3–24, 1992.

52 SHENG, J. J. **Modern chemical enhanced oil recovery: theory and practice**. [S.l.]: Gulf Professional Publishing, 2010.

53 KHADIM, M. A.; SARBAR, M. A. Role of asphaltene and resin in oil field emulsions. **Journal of Petroleum Science and Engineering**, Elsevier, v. 23, n. 3-4, p. 213–221, 1999.

54 MULLINS, O. C.; SHEU, E. Y. **Structures and dynamics of asphaltenes**. [S.l.]: Springer Science & Business Media, 2013.

55 TAMBE, D. E.; SHARMA, M. M. Factors controlling the stability of colloid-stabilized emulsions: I. an experimental investigation. **Journal of colloid and interface science**, Elsevier, v. 157, n. 1, p. 244–253, 1993.

56 LEVINE, S.; SANFORD, E. Stabilisation of emulsion droplets by fine powders. **The Canadian Journal of Chemical Engineering**, Wiley Online Library, v. 63, n. 2, p. 258–268, 1985.

57 WRIGHT, R. Jamin effect in oil production. **AAPG Bulletin**, American Association of Petroleum Geologists, v. 17, n. 12, p. 1521–1526, 1933.

58 MCAULIFFE, C. D. Crude-oil-water emulsions to improve fluid flow in an oil reservoir. **Journal of Petroleum Technology**, SPE, v. 25, n. 06, p. 721–726, 1973.

59 KHAMBHARATANA, F.; THOMAS, S.; ALI, S. F. Macroemulsion rheology and drop capture mechanism during flow in porous media. In: SPE. **SPE International Oil and Gas Conference and Exhibition in China**. [S.l.], 1998. p. SPE–48910.

60 YU, L. et al. Effects of interfacial tension and droplet size on the plugging performance of oil-in-water emulsions in porous media. **Industrial & Engineering Chemistry Research**, ACS Publications, v. 56, n. 32, p. 9237–9246, 2017.

61 DING, B.; DONG, M.; YU, L. A model of emulsion plugging ability in sandpacks: Yield pressure drop and consistency parameter. **Chemical Engineering Science**, Elsevier, v. 211, p. 115248, 2020.

62 SOO, H.; RADKE, C. A filtration model for the flow of dilute, stable emulsions in porous media—i. theory. **Chemical Engineering Science**, Elsevier, v. 41, n. 2, p. 263–272, 1986.

63 MORADI, M. et al. Dynamic flow response of crude oil-in-water emulsion during flow through porous media. **Fuel**, Elsevier, v. 135, p. 38–45, 2014.

64 WEI, B. et al. Flow behaviors of emulsions in constricted capillaries: A lattice boltzmann simulation study. **Chemical Engineering Science**, Elsevier, v. 227, p. 115925, 2020.

65 GUILLEN, V. R. et al. Capillary-driven mobility control in macro emulsion flow in porous media. **International Journal of multiphase flow**, Elsevier, v. 43, p. 62–65, 2012.

66 NOGUEIRA, G.; CARVALHO, M.; ALVARADO, V. Dynamic network model of mobility control in emulsion flow through porous media. **Transport in porous media**, Springer, v. 98, p. 427–441, 2013.

67 SOO, H.; RADKE, C. Velocity effects in emulsion flow through porous media. **Journal of Colloid and Interface Science**, Elsevier, v. 102, n. 2, p. 462–476, 1984.

68 DING, B.; DONG, M. Optimization of plugging high mobility zones in oil sands by injection of oil-in-water emulsion: Experimental and modeling study. **Fuel**, Elsevier, v. 257, p. 116024, 2019.

69 YU, L. et al. Experimental study on the effect of interfacial tension on the conformance control of oil-in-water emulsions in heterogeneous oil sands reservoirs. **Chemical Engineering Science**, Elsevier, v. 189, p. 165–178, 2018.

70 CHEN, Z. et al. Effects of oil viscosity on the plugging performance of oil-in-water emulsion in porous media. **Industrial & Engineering Chemistry Research**, ACS Publications, v. 57, n. 21, p. 7301–7309, 2018.

71 YU, L. et al. A new model of emulsion flow in porous media for conformance control. **Fuel**, Elsevier, v. 241, p. 53–64, 2019.

72 ALVARADO, D.; JR, S. M. Flow of oil-in-water emulsions through tubes and porous media. **Society of Petroleum Engineers Journal**, SPE, v. 19, n. 06, p. 369–377, 1979.

73 DEVEREUX, O. F. Emulsion flow in porous solids: I. a flow model. **The Chemical Engineering Journal**, Elsevier, v. 7, n. 2, p. 121–128, 1974.

74 SOO, H.; WILLIAMS, M.; RADKE, C. A filtration model for the flow of dilute, stable emulsions in porous media—ii. parameter evaluation and estimation. **Chemical Engineering Science**, Elsevier, v. 41, n. 2, p. 273–281, 1986.

75 AZIZOV, I.; DUDEK, M.; ØYE, G. Emulsions in porous media from the perspective of produced water re-injection–a review. **Journal of Petroleum Science and Engineering**, Elsevier, v. 206, p. 109057, 2021.

76 XIA, Y.; WHITESIDES, G. M. Soft lithography. **Angewandte Chemie International Edition**, Wiley Online Library, v. 37, n. 5, p. 550–575, 1998.

77 MCDONALD, J. C.; WHITESIDES, G. M. Poly (dimethylsiloxane) as a material for fabricating microfluidic devices. **Accounts of chemical research**, ACS Publications, v. 35, n. 7, p. 491–499, 2002.

78 LISTON, E. M. Plasma treatment for improved bonding: A review. **The journal of adhesion**, Taylor & Francis, v. 30, n. 1-4, p. 199–218, 1989.

79 BACHAROUCHE, J. et al. Singularities in hydrophobic recovery of plasma treated polydimethylsiloxane surfaces under non-contaminant atmosphere. **Sensors and Actuators A: Physical**, Elsevier, v. 197, p. 25–29, 2013.

80 JUNQUEIRA, H. C. et al. Modulation of methylene blue photochemical properties based on adsorption at aqueous micelle interfaces. **Physical Chemistry Chemical Physics**, Royal Society of Chemistry, v. 4, n. 11, p. 2320–2328, 2002.

81 DAVIES, E. R. **Machine vision: theory, algorithms, practicalities**. [S.l.]: Elsevier, 2004.

82 COOPER, B. W.; DUERR, J. T. **Full spectrum fluorescent dye composition for the optimization of leak detection processes**. [S.l.]: Google Patents, 2000. US Patent 6,165,384.

83 HUANG, L.-K.; WANG, M.-J. J. Image thresholding by minimizing the measures of fuzziness. **Pattern recognition**, Elsevier, v. 28, n. 1, p. 41–51, 1995.

84 LI, C. H.; LEE, C. Minimum cross entropy thresholding. **Pattern recognition**, Elsevier, v. 26, n. 4, p. 617–625, 1993.

85 LI, C.; TAM, P. K.-S. An iterative algorithm for minimum cross entropy thresholding. **Pattern recognition letters**, Elsevier, v. 19, n. 8, p. 771–776, 1998.

86 OTSU, N. et al. A threshold selection method from gray-level histograms. **Automatica**, v. 11, n. 285-296, p. 23–27, 1975.

87 KAPUR, J. N.; SAHOO, P. K.; WONG, A. K. A new method for gray-level picture thresholding using the entropy of the histogram. **Computer vision, graphics, and image processing**, Elsevier, v. 29, n. 3, p. 273–285, 1985.

88 ZHANG, Z. et al. The effects of 3d channel geometry on ctc passing pressure–towards deformability-based cancer cell separation. **Lab on a Chip**, Royal Society of Chemistry, v. 14, n. 14, p. 2576–2584, 2014.

89 MA, S. et al. On the flow topology inside droplets moving in rectangular microchannels. **Lab on a Chip**, Royal Society of Chemistry, v. 14, n. 18, p. 3611–3620, 2014.

90 WONG, H.; RADKE, C.; MORRIS, S. The motion of long bubbles in polygonal capillaries. part 1. thin films. **Journal of Fluid Mechanics**, Cambridge University Press, v. 292, p. 71–94, 1995.

91 O'CONNELL, M. G. et al. Cooperative size sorting of deformable particles in porous media. **Soft Matter**, Royal Society of Chemistry, v. 15, n. 17, p. 3620–3626, 2019.

92 TSAI, T.; MIKSIS, M. J. Dynamics of a drop in a constricted capillary tube. **Journal of fluid mechanics**, Cambridge University Press, v. 274, p. 197–217, 1994.

93 PEÑA, T.; CARVALHO, M.; ALVARADO, V. Snap-off of a liquid drop immersed in another liquid flowing through a constricted capillary. **AIChE journal**, Wiley Online Library, v. 55, n. 8, p. 1993–1999, 2009.

94 WANG, Z. et al. Probing the generation mechanism of emulsion based on shearing actions between multiphase fluids in porous media. **Colloids and Surfaces A: Physicochemical and Engineering Aspects**, Elsevier, v. 653, p. 129997, 2022.

95 SPEIRS, E. **Emulsion transport in two-dimensional porous media: influence of geometric and surface heterogeneities**. Tese (Doutorado) — Université de Rennes, 2023.